

Analyses of the Circulation in Intermediate and  
Shallow Water Masses of the North Atlantic with  
Lagrangian and Profiling Methods

(Untersuchungen zur Zirkulation in mittleren und  
oberen Wassermassen des Nordatlantiks mit  
Lagrange'schen und profilierenden Methoden)

Dissertation  
zur Erlangung des Doktorgrades  
der Mathematisch-Naturwissenschaftlichen Fakultät  
der Christian-Albrechts-Universität  
zu Kiel

vorgelegt von

Matthias Lankhorst

Kiel

2006

Referent: U. Send

Korreferent: M. Visbeck

Tag der mündlichen Prüfung: 30.1.2007

Zum Druck genehmigt: Kiel, 30.1.2007

gez. J. Grotemeyer – Dekan

# Contents

<b>Abstract</b>	<b>3</b>
<b>Zusammenfassung</b>	<b>5</b>
<b>1 Introduction</b>	<b>7</b>
1.1 Circulation and Hydrography of the North Atlantic . . . . .	7
1.2 Instrumentation . . . . .	11
1.2.1 Acoustic Floats . . . . .	12
1.2.2 Profiling Floats . . . . .	13
1.3 About this Dissertation . . . . .	13
<b>2 Transport Time Series of Northeastern Atlantic Current Systems Derived from Long-Distance Geostrophy</b>	<b>15</b>
2.1 Introduction . . . . .	15
2.2 Data and Basic Methodology . . . . .	16
2.3 Observed Currents and Transports . . . . .	18
2.4 Details of the Methodology . . . . .	21
2.4.1 Validation . . . . .	21
2.4.2 Error Estimates . . . . .	21
2.5 Concluding Remarks . . . . .	26
<b>3 RAFOS Float Observations at Intermediate Depths in the Northeastern Atlantic Ocean</b>	<b>27</b>
3.1 Introduction . . . . .	27
3.2 Selected Trajectories . . . . .	29
3.3 The Mesoscale Velocity Field . . . . .	36
3.3.1 Eddy Kinetic Energy, Integral Time Scale, and Derived Quantities . . . . .	36
3.3.2 Coherent Eddies . . . . .	40
3.4 Methodology . . . . .	43

3.4.1	Data Availability and Processing . . . . .	43
3.4.2	Calculation of the Integral Properties . . . . .	44
3.5	Concluding Remarks . . . . .	45
<b>4</b>	<b>A Self-Contained Identification Scheme for Eddies in Drifter and Float Trajectories</b>	<b>47</b>
4.1	Introduction . . . . .	47
4.2	Methodology . . . . .	48
4.2.1	About Autoregressive Processes . . . . .	48
4.2.2	Eddy Detection Criteria . . . . .	53
4.2.3	Validation . . . . .	55
4.3	Concluding Remarks . . . . .	59
<b>5</b>	<b>Zonal Intermediate Currents in the Equatorial Atlantic Ocean</b>	<b>61</b>
5.1	Introduction . . . . .	61
5.2	Results from Float Observations . . . . .	62
5.3	Concluding Remarks . . . . .	66
5.3.1	Equatorial Current Bands at Other Depths . . . . .	66
5.3.2	Notes on Dynamical Aspects . . . . .	67
<b>6</b>	<b>On the Circulation in the Northwestern Tropical Atlantic</b>	<b>69</b>
6.1	Mean Currents . . . . .	69
6.2	Mesoscale Variability . . . . .	75
6.3	Concluding Remarks . . . . .	78
6.4	Database for Chapters 5 and 6 . . . . .	79
<b>7</b>	<b>Summary and Conclusion</b>	<b>83</b>
<b>A</b>	<b>Glossary</b>	<b>87</b>
<b>B</b>	<b>Acknowledgements</b>	<b>91</b>
<b>C</b>	<b>Bibliography</b>	<b>93</b>

# Abstract

The Atlantic Meridional Overturning Circulation (MOC) transports warm water northwards in near-surface depth layers and cold water southwards at greater depths. This dissertation investigates aspects of the circulation within the context of the MOC in the northeastern and tropical Atlantic, based on observations of the past 20 years. The instrumentation mainly relies on submerged drifters called *floats*, which measure current velocities and—depending on instrument type—hydrographic profiles.

In the northeastern Atlantic, the entire water column is analyzed. Volume transports by currents in the upper 1000 m and their temporal variabilities are derived via long-distance geostrophy. These currents are a part of the upper, warm branch of the MOC. The total transport by the North Atlantic Current in the study area is approximately 25 Sv with interannual variability up to 3 Sv on interannual time scales for individual current branches. At intermediate depths, various spreading paths within the deep, cold branch of the MOC are documented by selected float trajectories, and the properties of the mesoscale eddy field are quantified. Lagrangian eddy kinetic energy and time scales show a strong contrast between the subpolar and the subtropical basins. Especially in the subpolar basin, several regions of increased eddy activity emerge. An algorithm for automatic identification of coherent eddies reports particularly many and energetic cyclones in the subpolar northeastern Atlantic, which obviously play an important role in the mixing processes there.

In the tropical Atlantic, depth layers in the intermediate and in the upper part of the deep waters are analyzed. The separation between northward- and southward-flowing branches of the MOC is between these layers. Both feature zonal bands of strong, alternating zonal currents near the equator. These bands are circa 200 km wide on average, and are in parts subject to a strong seasonal cycle. Boundary currents flow along the western boundary of the basin, northwards in the intermediate and southwards in the deep waters, which interact with the zonal current bands of the interior basin. Energy and time scales are described for the tropical region, too. Here, eddy activity generally increases towards the boundary.

The Lagrangian eddy kinetic energies and time scales at intermediate depths both in the tropical and the northeastern Atlantic are found to be 1–150  $\text{cm}^2 \text{s}^{-2}$  and 2–10 days. Highest mean current velocities at these depths are approximately 15  $\text{cm s}^{-1}$ .

New methodologies presented in this thesis are the observation of volume transport in the northeastern Atlantic by long-distance geostrophy and the algorithm to detect eddies in individual trajectories. Both are suited for future studies with similar instruments. The description of mean currents and the mesoscale eddy field is proper for validating numerical models of large-scale ocean circulation, which brings them back into the context of the MOC.



# Zusammenfassung

Die meridionale Umwälzbewegung (MOC, Meridional Overturning Circulation) des Atlantiks transportiert warmes Wasser in den oberflächennahen Schichten nordwärts sowie kaltes Wasser in größeren Tiefen südwärts. Diese Dissertation untersucht vor dem Hintergrund der MOC Teilaspekte der Zirkulation im nordöstlichen sowie im tropischen Atlantik, basierend auf Beobachtungen der letzten 20 Jahre. Als Meßgeräte kommen dabei hauptsächlich Unterwasserdrifter namens *Floats* zum Einsatz, die Strömungsgeschwindigkeit und – je nach Typ – vertikale hydrographische Profile messen.

Im Nordostatlantik wird die gesamte Wassersäule untersucht. Dabei werden Volumentransporte von Strömen in den oberen 1000 m sowie deren zeitliche Variabilität mittels Geostrophie über große Entfernungen bestimmt. Diese Ströme gehören zum oberen, warmen Zweig der MOC. Der Gesamttransport des Nordatlantischen Stromes im Beobachtungsgebiet beträgt circa 25 Sv mit einer Variabilität von bis zu 3 Sv auf interannualen Zeitskalen für einzelne Stromzweige. In mittleren Tiefen darunter werden anhand ausgewählter Float-Trajektorien verschiedene Ausbreitungspfade im tiefen, kalten Teil der MOC dokumentiert und die Eigenschaften des mesoskaligen Wirbelfeldes quantifiziert. Lagrange'sche Wirbelenergie und Zeitskalen zeigen einen starken Kontrast zwischen subpolarem und subtropischem Becken. Insbesondere im subpolaren Becken treten mehrere Regionen erhöhter Wirbelaktivität hervor. Ein Algorithmus zur automatischen Identifizierung kohärenter Wirbel findet im subpolaren Nordostatlantik auffallend viele und energetische Zyklonen, denen offensichtlich eine tragende Rolle bei dortigen Vermischungsprozessen zukommt.

Im tropischen Atlantik werden Tiefen im Zwischenwasser und im oberen Tiefenwasser beprobt. Die Grenze zwischen nord- und südwestlichem Zweig der MOC liegt zwischen diesen beiden Tiefen. In beiden kommen in Äquatornähe kräftige zonale Strömungsbänder von alternierender zonaler Strömungsrichtung vor. Diese Bänder sind im Mittel circa 200 km breit und unterliegen teilweise einem starken Jahresgang. Längs des westlichen Beckenrandes fließen Randströme, nordwärtig im Zwischenwasser und südwestlich im Tiefenwasser, die mit den zonalen Strömungsbändern im Beckeninneren im Austausch stehen. Auch für die tropische Region werden die Energie- und Zeitskalen des Wirbelfeldes beschrieben. Die Wirbelaktivität nimmt hier generell zum Beckenrand hin zu.

Die Lagrange'schen Wirbelenergie- und Zeitskalen liegen in mittlerer Tiefe sowohl im tropischen als auch im Nordostatlantik im Bereich von 1–150  $\text{cm}^2 \text{s}^{-2}$  und 2–10 Tagen. Die höchsten mittleren Strömungsgeschwindigkeiten in diesen Tiefen sind ungefähr  $15 \text{ cm s}^{-1}$ .

Methodische Neuerungen, die in dieser Arbeit vorgestellt werden, sind die Bestimmung der Volumentransporte im Nordostatlantik mittels Geostrophie über große Distanzen sowie der Algorithmus zur Wirbelerkennung in einzelnen Trajektorien. Beide eignen sich für zukünftige Studien mit ähnlichen Meßgeräten. Die Darstellungen der mittleren

Strömungen und des Wirbelfeldes bieten sich für die Validierung von numerischen Modellen der großräumigen Ozeanzirkulation an, womit sie wieder im Kontext der MOC stehen.



# Chapter 1

## Introduction

This dissertation is treating the circulation of the North Atlantic, considering the area from the equatorial current systems in the south to the ridge between Greenland, Iceland, and Scotland in the north. Results are based on recent observations by the physical oceanography groups at the *Leibniz-Institut für Meereswissenschaften (IFM-GEOMAR)* in the northeastern parts of the Atlantic as well as in the western tropical Atlantic.

### 1.1 Circulation and Hydrography of the North Atlantic

The most obvious large-scale features of near-surface circulation of the North Atlantic are the cyclonic subpolar gyre and the anticyclonic subtropical gyre. The former comprises a counterclockwise loop around the Labrador Sea, Irminger Sea, and Iceland Basin, while the latter essentially fills the remainder of the ocean from there to the equatorial current system in the south. Superimposed on this mainly wind-driven circulation is a component forced by density gradients, which leads to the Meridional Overturning Circulation (MOC) of the Atlantic. The MOC transports warm water northward near the surface and cold water southward at greater depth. The warm limb of the Atlantic MOC north of the equator transports water into and through the Caribbean Sea and the Gulf of Mexico. From there, the following well-known surface currents carry warm waters successively further north along the eastern shores of North America: the Florida Current, the Gulf Stream, and the North Atlantic Current (NAC). The NAC eventually leaves the proximity of the American continent and crosses the ocean towards Europe, following the boundary between the subpolar and the subtropical gyres. Downstream branches of the NAC include the Irminger Current southwest of Iceland, the North Atlantic Drift Current (sometimes still called NAC) southeast of Iceland, and the Azores Current south of the Azores. Of the warm limb of the MOC, this manuscript presents results on the latter three branches of the NAC, and on the circulation at intermediate depths in the tropical Atlantic, which are generally also assigned to the “upper” limb. Thereby, the beginning and the end of the path outlined in the previous sentences are sampled, and whatever lies inbetween is subject to other studies (an incomplete but introductory list of manuscripts treating these currents is: SCHMITZ AND MCCARTNEY, 1993; ROSSBY ET AL., 1985; ROSSBY, 1996).

On the other hand, the cold limb of the Atlantic MOC has its origins in the North Atlantic and the Arctic. Through atmospheric cooling, water gets denser there and sinks, e.

g. in the Nordic Seas. Such cold water spills over the relatively shallow topography connecting Greenland, Iceland, and Europe towards the south (HANSEN AND ØSTERHUS, 2000). Undergoing complex mixing processes and strongly guided by bottom topography, large portions of these overflow waters flow towards the western boundary of the Atlantic basin, i. e. off Labrador. Another reasonably deep water mass is formed directly in the Labrador Sea by wintertime convection. Together, this Labrador Sea Water and the overflow waters compose the main body of *North Atlantic Deep Water (NADW)* after being united at the southern exit of the Labrador Sea. NADW is then considered as the southward-flowing, cool branch of the Atlantic MOC, traditionally viewed as flowing in a *Deep Western Boundary Current (DWBC)* adjacent to the American continental shelf. The real spreading path is more complex, especially when exchange processes with the interior basin are considered. In the subtropical Atlantic, hydrography typically shows NADW at depths between 1200 and 4000 m. In this manuscript, data from the subpolar northeastern Atlantic and from the western tropical Atlantic from depths in the NADW are analyzed. These regions are therefore in the area where NADW gains its identity in the north, whereas in the tropics, it has travelled a considerable distance since its formation.

Figure 1.1 shows a rough overview over the hydrography of the entire Atlantic. Temperature and salinity data taken from the NODC (Levitus) World Ocean Atlas 1994 are displayed for a section spanning the Atlantic from Iceland in the north to the Antarctic Peninsula in the south. From the salinity section, one can identify three tongues of distinct water masses penetrating the ocean meridionally: Antarctic Intermediate and Bottom Waters (AAIW, AABW), both coming from the south, are identified by lower salinities than the surrounding waters. North Atlantic Deep Water (NADW), spreading from the north, is squeezed between them and therefore shows up as a local salinity maximum. This pattern of salinity as a function of depth, i. e. decreasing towards AAIW, then increasing in the NADW, and again decreasing for the AABW, is also apparent in the  $\Theta$ -S diagram indicated in the figure. The saltier waters closer to the surface in the subtropical gyres are not as easily associated with distinct spreading paths in this plot, because of flow perpendicular to the section and local patterns of evaporation and precipitation. However, strong horizontal gradients associated with the NAC are seen in the upper 1000 m near  $50^\circ$  N. Another feature is the inflow of salty Mediterranean Water, obvious in the plot at around  $30^\circ$  N at depths near 1000 m. Boxes in the figure indicate the areas studied in this manuscript, in the hope that the MOC stands out as a connecting background feature in which both study areas are intrinsically involved. The depth ranges under investigation here are intermediate depth levels in the tropical area and the entire water column except for the deepest bottom water in the northeastern Atlantic. Water masses at these depths are therefore the AAIW, the NADW, and the bulk of near-surface waters in the northeastern Atlantic. AABW is only mentioned for completeness here, as its remnants cover most of the Atlantic abyss and thus provide the bottom boundary for the analyses.

Clearly, the actual circulation is more complex than the simplified view of the MOC outlined in the previous paragraphs. Figure 1.2 attempts to summarize the circulation features of the North Atlantic between  $40^\circ$  N and  $70^\circ$  N and will serve as an introductory figure to the study area of the northeastern Atlantic here. This figure has been repeatedly used and modified within the context of the *Sonderforschungsbereich* SFB 460, a research initiative carried out at IFM-GEOMAR and the university of Kiel between 1996 and 2006. Near the surface, the NAC as the border between the two gyres transports warm waters from near Newfoundland northeastward. On its path, several current branches peel off, three of

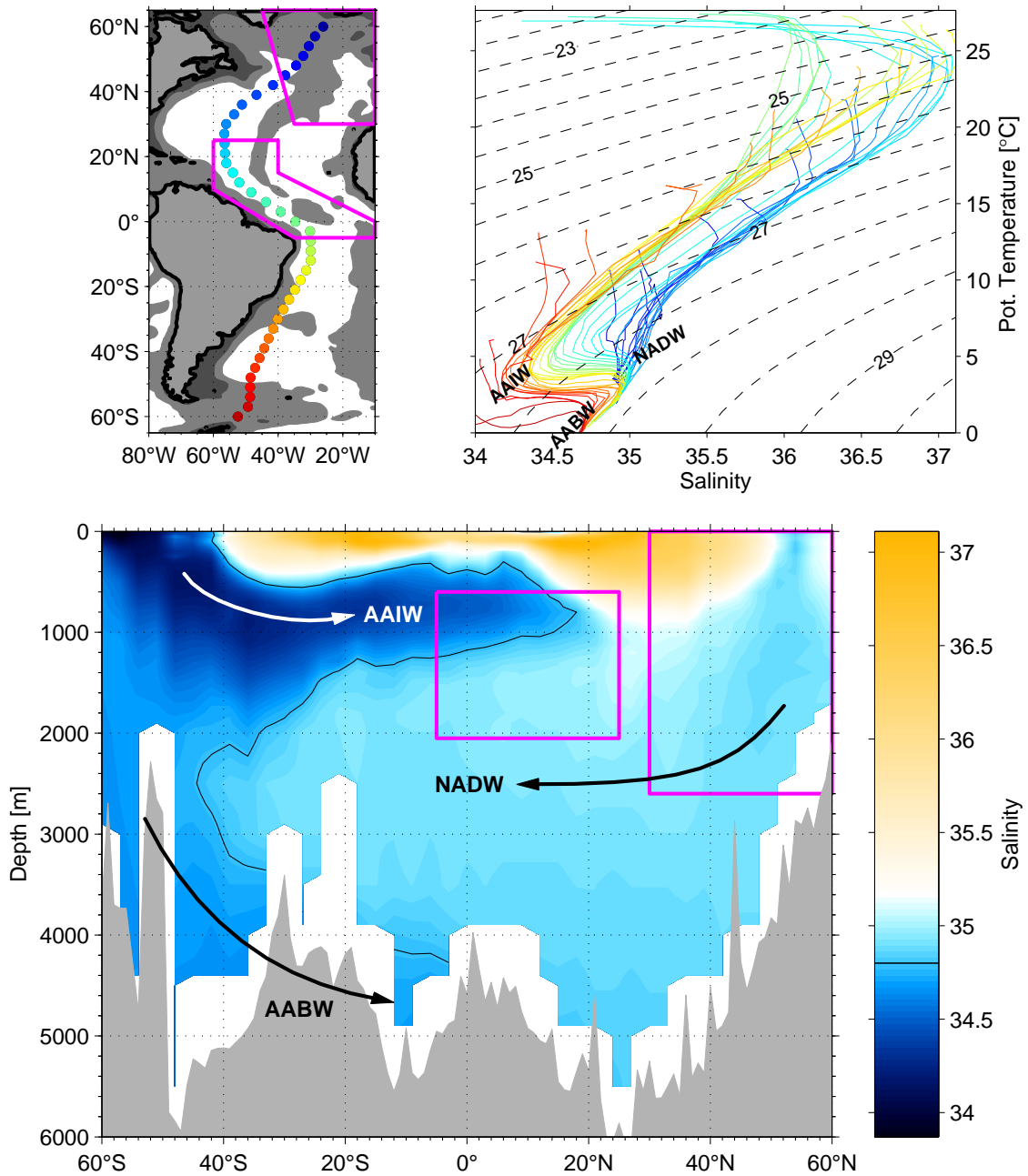


Figure 1.1: Hydrographic overview over the Atlantic, assembled from the NODC (Levitus) World Ocean Atlas 1994. *Top left:* Map of the Atlantic; grey shading at 1000 and 4000 m depth. *Top right:*  $\Theta$ - $\Sigma$  diagram; colors match stations on the map. Dashed lines denote isopycnals. *Bottom:* Salinity section with schematic spreading paths of three water masses: AAIW Antarctic Intermediate Water, NADW North Atlantic Deep Water, AABW Antarctic Bottom Water. The black line denoting the isohaline of 34.8 separates the three water masses. Purple boxes indicate roughly the areas studied in this manuscript: the northeastern Atlantic from top to bottom, and the AAIW as well as the upper NADW in the tropical Atlantic. Grey shading outlines bottom topography along the section.

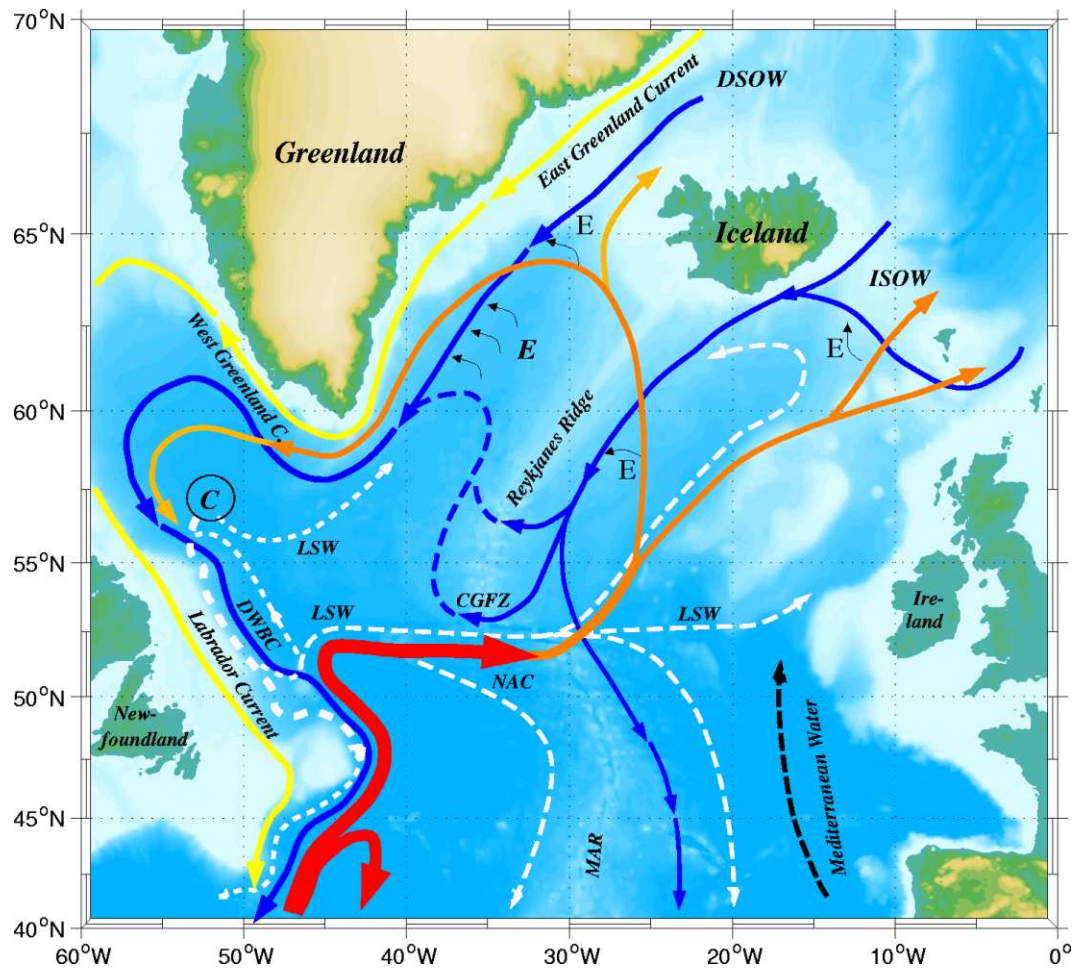


Figure 1.2: Schematic of the circulation in the North Atlantic, widely reproduced and modified from the IFM-GEOMAR SFB460 web site ([www.ifm-geomar.de/index.php?id=sfb460](http://www.ifm-geomar.de/index.php?id=sfb460)). *Red and yellow*: Near-surface currents. *Dashed black and white*: Intermediate currents. *Blue*: Near-bottom currents. Abbreviations are: C Convection, CGFZ Charlie-Gibbs Fracture Zone, E Entrainment, LSW Labrador Sea Water, ISOW Iceland-Scotland Overflow Water, MAR Mid-Atlantic Ridge, NAC North Atlantic Current. The individual current branches are discussed in the context of the Meridional Overturning Circulation, where the NAC (net northward flow) and the deep currents (net southward flow) balance each other.

which are investigated here in chapter 2. Chapter 4 also makes use of data collected within the NAC regime, although the focus of the chapter is on the methodology presented therein. Underneath the depth range covered by the NAC, at intermediate depths between 500 and 2000 m, Labrador Sea Water (LSW) disperses from its formation regions in the Labrador Sea along various pathways. Chapter 3 treats its spreading routes in the eastern basins, i. e. east of the Mid-Atlantic Ridge, where the figure indicates three branches separating east of Charlie-Gibbs Fracture Zone (CGFZ). Also in the eastern basins, Mediterranean outflow brings salty, warm water to similar intermediate depths, although mostly a little shallower than LSW and thus outside the scope of chapter 3. Deeper yet, the overflow waters from Denmark Strait and the Iceland-Scotland Ridge occupy the subpolar Atlantic after having crossed the shallower sills in the north. In the northeastern Atlantic, parts of these water masses are captured by the instruments of chapter 3, and pathways and mixing processes between them and LSW are identified. Eventually, the overflow waters follow the topography around the Iceland, Irminger, and Labrador Sea Basins, before exiting the subpolar region into the subtropics as parts of the NADW.

In the tropical Atlantic, the westward-flowing branches of the subtropical gyres on either hemisphere, the Northern and Southern Equatorial Currents (NEC/SEC), provide the lateral boundaries to the equatorial current system between them. Flow patterns in the tropical Atlantic are generally aligned in zonal bands, the distribution and amount of which makes it difficult to summarize their appearance in brief. At the surface, the eastward-flowing North Equatorial Countercurrent (NECC) and multiple westward branches of the SEC complicate the picture outlined by the simple concept of westward NEC/SEC for latitudes below  $10^\circ$ . In the upper thermocline, the strong eastward Equatorial Undercurrent (EUC) deserves mention, along with the Northern and Southern Equatorial Undercurrents (NEUC/SEUC). Chapter 5 discusses five named zonal current bands at intermediate depth ranges covered by the AAIW in the lower thermocline, plus indications of multiple other bands. The main features of the AAIW depth are also found in the upper NADW in the area. Further complexity is caused by seasonal variability and interaction with the western boundary currents, both of which are addressed in chapters 5 and 6. Flow along the western boundary in the equatorial Atlantic is generally northward in the upper waters including AAIW, whereas it is southwards in the NADW, as would be expected from the concept of the MOC. Details of the flow field, in particular interaction with the zonal flows filling the interior basins, are less well-known, and provide the motivation for the studies presented here.

## 1.2 Instrumentation

Due to their fundamental character for this study, the technology of different underwater drifters called *floats* will be reviewed in the following paragraphs. Floats are either actively (by a pumping system) or passively (by careful weighing) ballasted to drift underwater usually on constant depth or pressure levels, or on isopycnals (SWIFT AND RISER, 1994). As electromagnetic waves (light, radio) are not well transmitted by water, two positioning strategies for floats have evolved: one is by using acoustics, which works underwater, and the other involves floats temporarily rising to the surface for positioning via satellite. Figure 1.3 shows two such instruments. ROSSBY (2007) gives a thorough review of float technology since the middle of the 20th century. For a more general account of other sensors and measurement techniques, the interested reader is referred to standard oceanography textbooks



Figure 1.3: Fotos of two floats. Both are approximately 1.5 m long. *Left:* An acoustic RAFOS float from an experiment in the 1990's. Through its glass housing, the electronics are visible. At the bottom end, one can see the hydrophone and a drop weight, which enables the float to return to the surface once at the end of the mission, typically after 1–2 years. *Right:* A state-of-the-art profiling float as used in the Argo array. Sensors and the antenna are at the top of the instrument. On the bottom end, a plastic shield covers the inflating rubber bladder that is part of the buoyancy control. This instrument is designed to return to the surface from 2000 m every 10 days and deliver temperature and salinity profiles each time, up to 150 times.

(e. g. PICKARD AND EMERY, 1990). Apart from floats, results from the following equipment are used in this study:

- moored sensors for salinity, temperature, and pressure,
- satellite altimetry,
- output from numerical models,
- velocity observations from ADCPs (acoustic doppler current profiler),
- velocity observations from moored mechanical sensors,
- combined data products for mean sea surface height and hydrography.

### 1.2.1 Acoustic Floats

The vertical hydrographic structure over much of the world ocean is such that sound velocity has a minimum at intermediate depth (typically between 800 and 1500 m in the tropical and subtropical regions). By laws of refraction, this layer will tend to “capture” sound signals emitted within it at reasonably horizontal angles, much like an optical fiber cable, and is called the *SOFAR channel* (SOund Fixing And Ranging). Early float designs called SOFAR floats made use of this sound fixing by drifting at that particular depth (e. g. FREELAND ET AL., 1975). They carried large sound sources which were heard by fixed listening stations. From different arrival times of the sound signals at different listening stations, the positions of the floats can be derived over distances exceeding 1000 km with appropriate sound signals. The same technology reversed, with moored sound sources

and receivers on the floats, is called *RAFOS floats* (SOFAR spelled backwards) and was introduced by ROSSBY ET AL. (1986a). This allows for larger amounts of floats at reduced costs, and the RAFOS instruments are the type of acoustic floats that are most often used today. Recent experiments have also been successful with drift depths outside the classical SOFAR channel (e. g. LANKHORST AND ZENK, 2006, instruments at 2600 m, chapter 3 here), suggesting that sound paths at greater inclination or even surface reflections (e. g. trajectory in the Labrador Sea in figure 3.2) still yield useful results. A sophisticated version of RAFOS floats called *MARVOR* has a pumping mechanism to return to the surface multiple times, similar to the profiling floats of the next paragraph, and therefore eliminates the need for pre-scheduled mission lengths while returning data already earlier in the mission.

### 1.2.2 Profiling Floats

Another strategy to locate floats is to have them return to the sea surface temporarily, where they can be located via satellite (the ARGOS satellite system is commonly used, an alternative would be a combination of GPS and IRIDIUM). Obviously, these floats carry a pumping system to ascend and descend. Provided that the time at the surface and the times spent in ascent and descent are small compared to the underwater drift, biases in the deep currents derived from the surface fixes are usually small. Today, an international effort called *Argo* maintains several thousand of these instruments throughout the world ocean. Current designs used in Argo are equipped with sensors for temperature, salinity, and pressure to collect hydrographic profiles whilst ascending or descending, and to actively control their drifting depth underwater. In fact, most of the scientific analyses involving Argo floats have focused on the hydrographic profiles rather than the velocity information from the float displacements (ROSSBY, 2007). In contrast, early float designs (DAVIS ET AL., 1992) had neither active depth control nor capabilities to sample hydrographic profiles. The majority of Argo floats, much like their predecessors, are on a ten-day cycle with approximately half a day at the surface and the remainder underwater. Recent developments use Argo floats as platforms to carry sensors other than the standard hydrographic ones, indeed also including RAFOS acoustics (FISCHER ET AL., 2007), thereby blurring the differences between the two float types.

## 1.3 About this Dissertation

Each chapter of this dissertation represents an individual study that has either been published in the scientific literature already or is in preparation for being published. The connection between the chapters, as already pointed out in the previous paragraphs, is both methodological and physical, as all chapters use float data to investigate the flow field within the broad context of the MOC. The title of the work, “Analyses of the Circulation in Intermediate and Shallow Water Masses of the North Atlantic with Lagrangian and Profiling Methods”, reflects this: the term *Lagrangian* refers to the technique of deriving flow from floats that drift with the currents, whereas *Profiling* hints at the hydrography sampled by profiling floats.

Chapter 2 presents a study of the near-surface currents in the northeastern Atlantic derived from profiles through the assumptions of geostrophy.

Chapter 3, although located in the same area, analyzes flow at intermediate depths by

direct observations from acoustic floats.

Chapter 4 details a methodology used in chapter 3, highlighting the capability of acoustic floats to resolve the mesoscale eddy field.

Chapters 5 and 6 treat the tropical Atlantic at intermediate depths, differentiating between the equatorial and the northwestern part. Both chapters make use of velocity observations from profiling and acoustic floats.

This manuscript finishes with a summary and an appendix, which contains a list of abbreviations, acknowledgements, and the bibliographic references.



## Chapter 2

# Transport Time Series of Northeastern Atlantic Current Systems Derived from Long-Distance Geostrophy

With the existing ocean observation systems, the transports of three major currents in the northeastern Atlantic are monitored at a semiannual resolution in time. The currents are the Irminger, North Atlantic Drift, and Azores Currents, all relevant for European climate. Results are presented on the mean transports of all of them, as well as on the interannual variability of the former two. The method uses geostrophy over basin-scale distances, the density being measured by profiling floats and nearby moorings. Dynamic sea surface height composed of a recent global estimate of the mean plus measurements by satellite altimetry provides a reference level for the geostrophic assumption, which is found to compare well with independent observational and model results. All of the results are essentially directly derived from observations and have potential for semi-automatic monitoring, provided that the observing systems remain in place.

This chapter reproduces LANKHORST, SEND AND BIASTOCH (2007b, ©American Geophysical Union (AGU), by general permission to the author).

### 2.1 Introduction

The Gulf Stream–North Atlantic Current System as the upper limb of the Meridional Overturning Circulation (MOC) and the northward part of the subtropical gyre is the main circulation feature of the North Atlantic in many aspects (for a detailed review, cf. ROSSBY, 1996). One of these aspects is its role for global and in particular European climate due to northward heat transport. Downstream branches of the North Atlantic Current near or east of the Mid-Atlantic Ridge and thus closer to Europe are difficult to observe due to their weaker currents along less well-defined pathways, which contrast sharply with e. g. the strong, single-branch Gulf Stream further upstream. Yet, they must be expected to be important for European climate plainly due to their proximity to this continent, and will be the focus of this chapter. The observational difficulties are addressed by using a geostrophic

end-point technique. This long-distance observational method inherently averages over unresolved eddy features, and even weak currents are detectable, although data coverage is sparse. Similar techniques have been applied by CURRY AND MCCARTNEY (2001) in the northwestern Atlantic and by KANZOW ET AL. (2006) in the tropical Atlantic.

Figure 2.1 shows a map of the North Atlantic with three “sections”, which will be referred to as containing three major near-surface currents: the Irminger Current (IrmC), the North Atlantic Drift Current (NADC), and the Azores Current (AzC). This section is concerned with current velocities and volume transports across the three sections (thus mainly by the above-mentioned currents), which are derived from observations alone at a semiannual resolution. To the best of my knowledge, this is the first purely observational study addressing mean currents, their vertical structures, and interannual variability in this region which compares favorably with independent observations and model results even after the delicate referencing of the geostrophic velocity shear. The work also aims at supporting the idea of an integrated ocean observing effort by demonstrating success of this synthesis of several observation systems, as outlined by the Global Ocean Observing System (GOOS).

## 2.2 Data and Basic Methodology

Velocities are computed via the geostrophic method, which relates vertical shear of horizontal velocity to the horizontal gradients of the density field (cf. standard oceanographic textbooks, e. g.: POND AND PICKARD, 1983). To integrate the shear to absolute velocities, one must know the constant of this integration, also called a “level of known motion”, which has been a crucial limitation of the method for decades.

In this study, the density profiles are derived from measurements by profiling floats of the Argo array and by moored sensors from the OceanSITES infrastructure. Both deliver temperature and salinity profiles versus pressure, from which density profiles and thus vertical shear are derived. Argo floats measure profiles typically every 10 days in the upper 2000 m. Of the moorings, the sites CIS (Central Irminger Sea), PAP (Porcupine Abyssal Plain), and ESTOC (Estación Europea de Series Temporales del Oceano, Islas Canarias) from the ANIMATE (Atlantic Network of Interdisciplinary Moorings and Time-series for Europe) project (now MERSEA, Marine Environment and Security for the European Area) are used. They contain instruments at fixed depths (approx. 10 sensors in the upper 1000 m), data of which is combined to a single profile every 10 days and then treated the same way as a float profile. The CIS and ESTOC moorings are located in the northernmost and southernmost polygons of figure 2.1, resp., while PAP is only used in the validation section, because PAP has not delivered sufficient data for time series analyses. A total of 980 profiles, 133 of which are from the moorings and the rest from floats, are used from within the polygons of figure 2.1.

As the level of known motion, the surface is chosen: the mean dynamic sea surface height is taken from the climatology by MAXIMENKO AND NIILER (2005, derived from surface drifters, satellite altimetry, wind reanalyses, and GRACE satellite gravimetry), and a temporally varying component comes from satellite altimetry alone. Table 2.1 lists all data products and their sources used in this section. For data from Argo and altimetry, delayed-mode data with presumably higher levels of error correction were used if they were available, otherwise the (near-) real-time data were used. The most recent data applied is from Sept. 2006 for both. OceanSITES mooring data from the ANIMATE sites were

Table 2.1: Overview over data sets used in chapter 2. T: Temperature, S: Salinity, P: Pressure, V: Velocity, SSH: Sea Surface Height. The last four rows show data included for validation purposes only, while data sets from the first four rows compose the results of this study.

Data Type	Instrumentation	Project, Product, Name	Data Source	References
T, S, P	Profiling Floats	Argo	Argo Data Centers	<a href="http://www.argo.ucsd.edu">www.argo.ucsd.edu</a> <a href="http://argo.jcommops.org">argo.jcommops.org</a>
T, S, P	Moorings	OceanSITES (ANIMATE, MerSEA)	IFM-GEOMAR	<a href="http://www.oceansites.org">www.oceansites.org</a> <a href="http://www.noc.soton.ac.uk/animate/">www.noc.soton.ac.uk/animate/</a>
Mean SSH	Composite Product	MDOT	N. Maximenko	<a href="http://iprc.soest.hawaii.edu/~nikolai/DOT/">iprc.soest.hawaii.edu/~nikolai/DOT/</a>
SSH Anomaly	Satellite Altimetry	SSALTO/DUACS “Merged”	AVISO	<a href="http://las.aviso.oceanobs.com/las/servlets/dataset">las.aviso.oceanobs.com/las/servlets/dataset</a>
V	ADCP (voluntary obs. ship)	Nuka Arctica	Ø. Knutsen	KNUTSEN ET AL. (2005)
V	RAFOS Floats	SFB 460, Eurofloat	IFM-GEOMAR	LANKHORST AND ZENK (2006)
T, S, P, V	Numerical Model	ORCA 05	A. Bias-toch, IFM-GEOMAR	
T, S	Composite Product	World Ocean Atlas	NODC, CDC	<a href="http://www.cdc.noaa.gov">www.cdc.noaa.gov</a>

available until 2004 or 2005 depending upon location. The mean sea surface refers to the period 1992–2002, which is not quite the observational period here, but there is overlap.

To obtain time series of the three transports, a temporal resolution of six months (centered around mid-winter and mid-summer) was chosen as a compromise between data sparsity and want for high resolution. For each time interval, density profiles from within the polygonal areas indicated in figure 2.1 are averaged to a mean profile of geopotential anomaly. The locations of the polygons were chosen based on availability of profile data, and geostrophic shear being low within them as expected from a hydrographic climatology (World Ocean Atlas, cf. table 2.1 and section 2.4.2). Surface values of geopotential anomaly are derived simultaneously by averaging over those gridpoints from the (gridded) sea surface height products that lie within the corresponding polygons. Together, these yield the absolute velocity profiles of figure 2.2. Velocity profiles were then integrated over the upper 1000 dbar to create time series of volume transport shown in figure 2.3.

The accuracy of the method is limited by the sparseness of the profile data, whereas satellite coverage is presently not critical due to the large areas and long time intervals over which to average. Errors are introduced to the velocity estimates by sensor error,

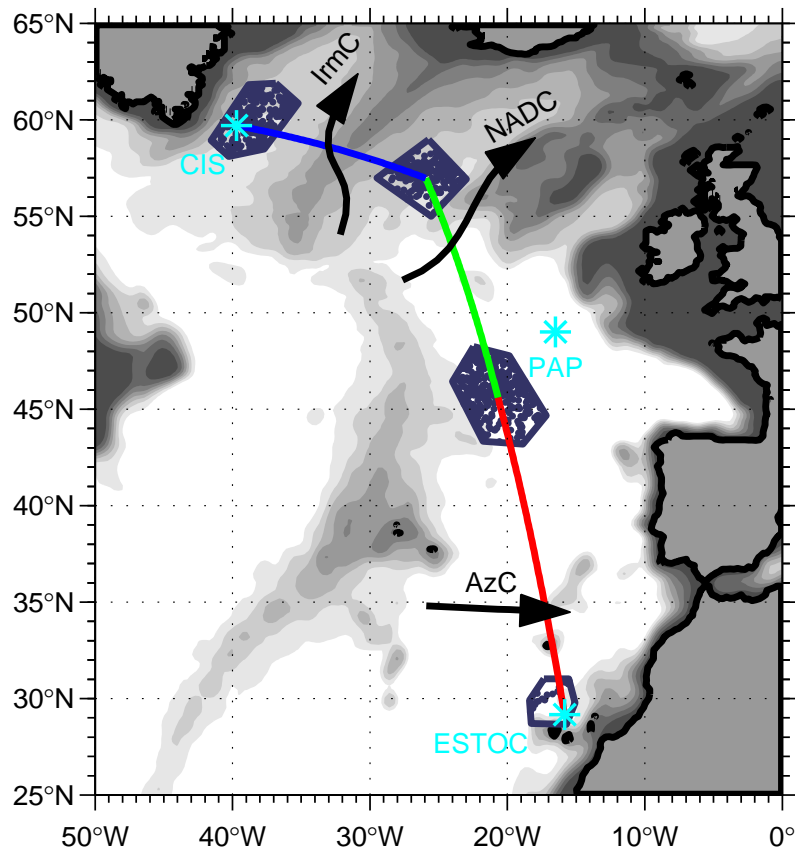


Figure 2.1: Map of the North Atlantic indicating three sections, across which the following major currents flow: Irminger Current (IrmC), North Atlantic Drift Current (NADC), Azores Current (AzC). Data is from density profiles within clusters near section endpoints (dark dots in polygonal areas). Cyan symbols denote the location of three mooring sites (CIS, PAP, ESTOC). PAP has not delivered sufficient data for time series analyses and is therefore not used in the main part of the study. Grey shading indicates bathymetry every 500 m down to 3500 m. Adapted from LANKHORST ET AL. (2007b, © AGU).

inconsistent location of the data, and natural variability due to mesoscale eddies, all of which are discussed in section 2.4.2. All of these errors are reduced statistically with increasing amount of data, which may be obvious but repeats the need for sustained observations.

### 2.3 Observed Currents and Transports

The three sections of figure 2.1 are designed to contain the IrmC, the NADC, and the AzC. Although there are other circulation features, multiple branches of these currents, and different naming conventions, we shall restrict our nomenclature to these for simplicity. In particular, NADC will refer to the branch east of the Mid-Atlantic Ridge to differentiate it from the NAC.

The IrmC section has been the target of the recent study by KNUTSEN ET AL. (2005), who find rich detail in the near-surface circulation. In this more large-scale approach, a

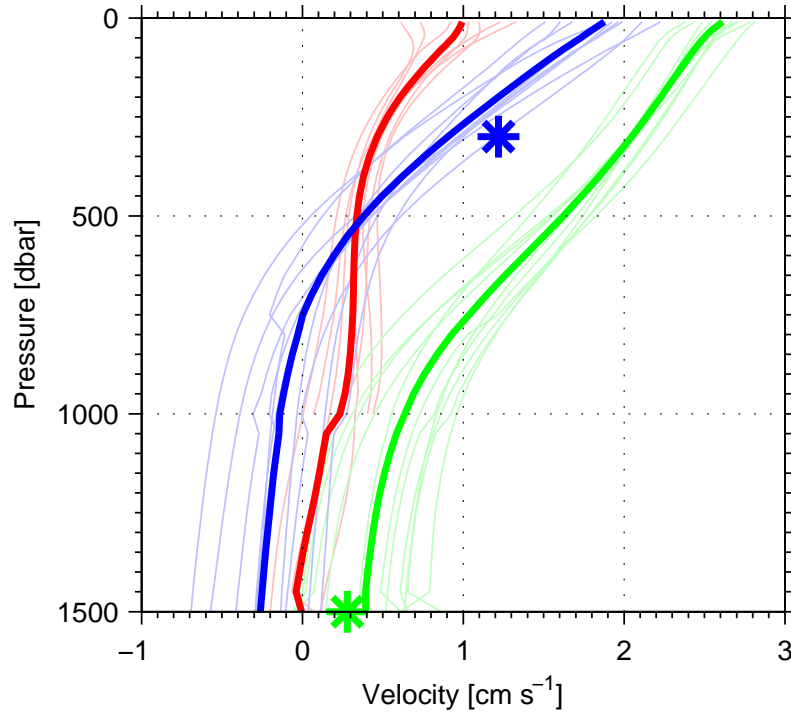


Figure 2.2: Averaged (thick) and semiannual (thin) vertical velocity profiles across the sections shown in figure 2.1. Two asterisk symbols indicate independent direct velocity measurements for validation. Adapted from LANKHORST ET AL. (2007b, © AGU).

baroclinic signature of the current down to about 700 m is identified. The near-surface velocities reach  $2 \text{ cm s}^{-1}$  when averaged over the distance of 800 km, in good quantitative agreement with results by KNUTSEN ET AL. (2005, asterisk at 300 dbar in figure 2.2). This defines a volume transport of around 5 Sv ( $1 \text{ Sverdrup} = 10^6 \text{ m}^3 \text{ s}^{-1}$ ). Error estimates from the mean sea surface height imply that this value is certain only to within 2.9 Sv, but agreement with the observations by KNUTSEN ET AL. (2005) suggests that the result is significantly better. Data coverage allows for a continuous time series since 2001/02 (figure 2.3), during which transport values have varied between 2 Sv and 7 Sv, with minima in 2001/02 and 2004, and maxima in 2002/03 and 2006. Thus, most of the variability is at interannual timescales near 2–3 years for the given interval. Obviously, water parcels that join the Irminger Current further north after a loop through the Iceland Basin (BOWER ET AL., 2002) are not captured in this IrmC section, but in the NADC section to the south.

The NADC section contains by far the largest transports of the three. Vertical profiles indicate that the baroclinic structure of the current reaches down to 1000 m, and that weaker eastward flow persists to depths beyond 1500 m, which agrees with findings by LANKHORST AND ZENK (2006, asterisk at 1500 dbar in figure 2.2, chapter 3 here). The section is approximately 1300 km long, which means that with averaged surface velocities near  $2.5 \text{ cm s}^{-1}$ , the mean volume transport is 20 Sv and in good agreement with e. g. the results by PÉREZ-BRUNIUS ET AL. (2004, streamlines in their figure 7). The error estimate from the mean sea surface height suggests an uncertainty of 3.5 Sv in this case. The time series begins in 2001 and lasts until now. Transport varies by about 3 Sv between 2001 and 2006, with minima near 17 Sv in 2003 and 2006 and maxima near 23 Sv in 2001 and

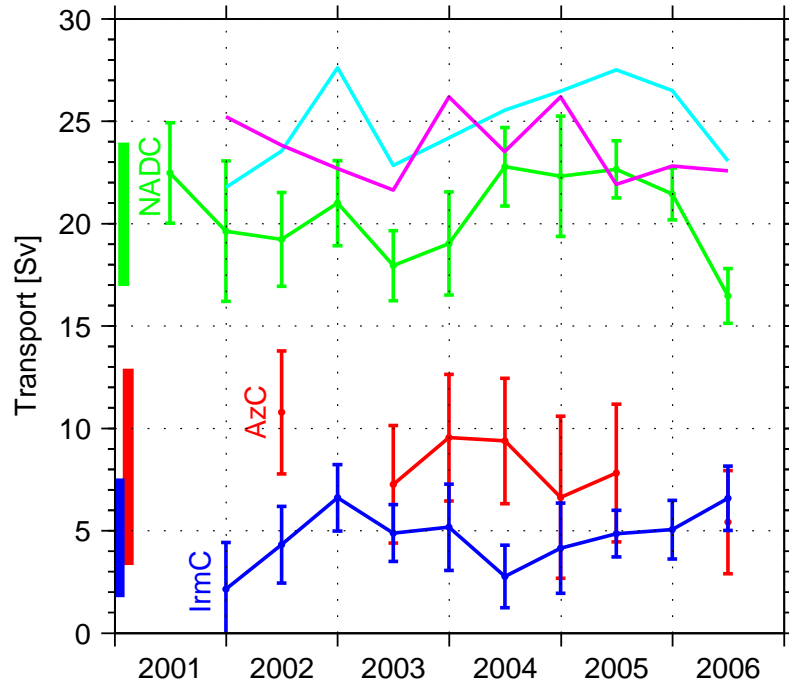


Figure 2.3: Time series of volume transport within the upper 1000 dbar across the IrmC, NADC, and AzC sections (blue, green, red; cf. figure 2.1). Error bars are explained in section 2.4.2. Thick bars near the left edge indicate uncertainties introduced by the mean SSH which are constant with time. The two additional time series are the sum of IrmC and NADC (cyan) and that of the section in figure 2.4 (magenta). Adapted from LANKHORST ET AL. (2007b, © AGU).

2004/05 (figure 2.3). This temporal pattern roughly represents the switching to and from a “southern mode” in the location of the NAC above the Mid-Atlantic Ridge as found by BOWER AND VON APPEN (2006, their figure 7) from satellite altimetry. During their “southern mode”, the main axis of the NAC crosses the Mid-Atlantic Ridge near  $50^{\circ}$  N, which is further south than the average. Here, during the same time interval, the NADC transport is below average. Again, dominant timescales are around 2–3 years, in agreement with the persistence of different flow patterns reported by BOWER AND VON APPEN (2006) for the longer time interval 1993–2005.

Despite the relatively large uncertainties, an anti-phase correlation is obvious between the IrmC and NADC sections in figure 2.3. The sum of the two, also shown in figure 2.3, undulates around 25 Sv with variability at the limit of the confidence intervals. However, the results by BOWER AND VON APPEN (2006) suggest that this should not be interpreted as a mere shifting of the mean current axis across the location where the profiles are taken, since their NAC axis is actually further away from the IrmC section during the time where we see lower NADC and higher IrmC transports. Instead, this highlights the complex evolution of the various current branches, of which little is yet understood.

The AzC section further south unfortunately lacks sufficient data coverage to derive variability, given the uncertainties of the measurements. However, from the mean data, a shallower signature (300 m) of the current and an overall transport estimate between 5 and

10 Sv are derived (figs. 2.2 and 2.3), which compares well with earlier results by KLEIN AND SIEDLER (1989).

## 2.4 Details of the Methodology

### 2.4.1 Validation

As an independent comparison to support the geostrophic velocities, two direct velocity measurements are included in figure 2.2. One is from the section repeatedly sampled by voluntary observing ship “Nuka Arctica” (KNUTSEN ET AL., 2005), which is close to the northernmost section of this study. “Nuka Arctica” has been equipped with an ADCP (acoustic Doppler current profiler), and the asterisk symbol at 300 dbar in figure 2.2 indicates mean northward velocity averaged along multiple ship tracks between the Irminger and Iceland Basins and between 250 and 350 m depth. The ship tracks are aligned zonally on average, therefore northward velocity corresponds to the across-section component. The other asterisk in figure 2.2 is derived from RAFOS float data (LANKHORST AND ZENK, 2006, chapter 3 here), from which velocity measurements were box-averaged, interpolated onto the corresponding section, and then rotated to derive across-section velocity. In both instances, agreement with the velocities from this study is good, which especially highlights the quality of the reference level chosen (i. e. the mean dynamic sea surface by MAXIMENKO AND NIILER, 2005).

For further validation, output from the numerical ocean circulation model ORCA05 was analyzed. The ORCA05 model is a  $\frac{1}{2}^\circ$  version of the global ocean-sea ice model described by BARNIER ET AL. (2006). It is forced by daily CORE data (LARGE AND YEAGER, 2004) for the period 1958–2000, applied to the ocean via bulk formulae. Due to the resolution, the model does not contain mesoscale eddies but has a fairly realistic large-scale and boundary current structure. Figure 2.4 shows vertical velocity profiles across another section in the North Atlantic, for which float and mooring data were available at either end of the section. Mooring data in this case are from the CIS and PAP sites of the ANIMATE array. The graphs show geostrophic currents from float observations alone, and from mooring observations alone, both derived from all-time means and referenced to the Maximenko-Niiler sea surface. Furthermore, the plot contains an averaged profile of the direct across-section velocities from the ORCA model (model years 1996–2000), and a geostrophic estimate using the ORCA hydrography at the section endpoints referenced to the direct velocities at depth. All four curves agree remarkably well, suggesting that the methodology is consistent and that assumptions regarding geostrophy and reference level are appropriate. In particular, agreement between the two model graphs demonstrates the validity of the method except for the Ekman layer in the top 100 m. For completeness, the transport time series derived from the observations is also included in figure 2.3. It averages just below 25 Sv with insignificant variability or trend throughout the observational period.

### 2.4.2 Error Estimates

To judge on the statistical significance of the transport values, possible sources of uncertainty are quantified in this section. Corresponding error bars in figure 2.3 account for the following uncertainties:

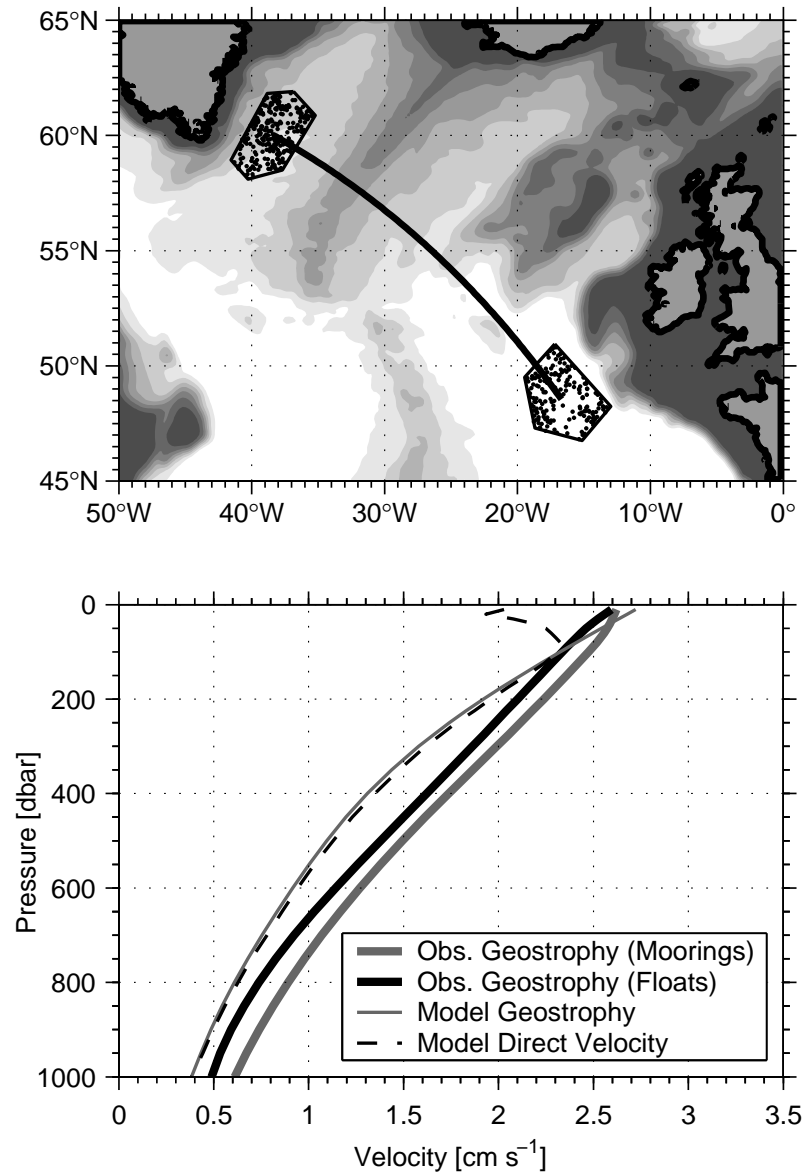


Figure 2.4: Location of (top) and averaged vertical velocity profiles (bottom) across another section in the North Atlantic. Here, both float and mooring data are available at either end of the section, although not simultaneously for the moorings. For validation of the method, results from geostrophy are shown for mooring and float data separately, and geostrophic velocities are compared against direct velocities in the ORCA05 model. Otherwise as figs. 2.1 and 2.2. Adapted from LANKHORST ET AL. (2007b, © AGU).



**Natural Variability:** To account for the chance of a profile being in a subsampled circulation feature like a mesoscale eddy, an error  $\sigma_{\text{eddy}}$  is estimated based on the number of profiles available,  $N_{\text{prof}}$ :

$$\sigma_{\text{eddy}} = \frac{1 \text{ Sv}}{\sqrt{N_{\text{prof}}}} \quad (2.1)$$

1 Sv was chosen from typical differences between successive float profiles, and this value is also consistent with estimates of eddy velocities and radii shown by LANKHORST AND ZENK (2006,  $10 \text{ cm s}^{-1} \cdot 10 \text{ km} \cdot 1000 \text{ m} = 1 \text{ Sv}$ , cf. chapter 3 and figures 3.11 and 3.12 here). Decorrelation time scales for temperature and salinity from the ANIMATE moorings are 3–5 d, and from the floats 10–15 d, hence each profile will be interpreted as statistically independent.

**Sensor Offset:** The following error estimate accounts for sensor offsets in temperature and salinity, based on the number of instruments  $N_{\text{sensor}}$  and the following choices of  $\Delta$  for the sections: 1.6 Sv (IrmC), 1.9 Sv (NADC), or 2.6 Sv (AzC):

$$\sigma_{\text{sensor}} = \frac{\Delta}{\sqrt{N_{\text{sensor}}}} \quad (2.2)$$

The estimates for  $\Delta$  are based on vertically constant offsets of -0.02 K in temperature and +0.05 in salinity, which are conservative estimates based on float performance and lead to an error in geopotential anomaly accumulating over 1000 m depth. Differences between the sections are caused by the nonlinearity of the equation of state of sea water and the change of the Coriolis parameter, both of which tend to worsen the results towards the south (i. e. towards warmer water and lower Coriolis parameter). Increasing the number of platforms,  $N_{\text{sensor}}$ , reduces the error, while retrieving multiple profiles from the same platform does not, thereby assuming that the sensor errors are statistically independent.

**Location Offset:** The (arithmetic) mean position of the available profiles is compared with a fixed location within the corresponding polygon (the mooring locations if available, the mean of the polygon vertices otherwise, cf. figure 2.1), and the distance  $D$  between the two comprises an error estimate for location mismatch:

$$\sigma_{\text{loc}} = 0.01 \frac{\text{Sv}}{\text{km}} \cdot D \quad (2.3)$$

This estimate is based on the hydrographic climatology of the NODC (Levitus) World Ocean Atlas, which was also used to design the polygonal areas such that expected offsets remain below 2 Sv for each polygon. These polygons and the climatological transport errors are displayed in figure 2.5.

All individual terms are computed for each polygon. For the corresponding section, the errors of the two neighboring polygons are in turn added up to:

$$\sigma_{\dots}^2 = \sigma_{\dots, 1}^2 + \sigma_{\dots, 2}^2 \quad (2.4)$$

A total error estimate  $\sigma_{\text{total}}$  is then composed of these individual terms by

$$\sigma_{\text{total}}^2 = \sigma_{\text{eddy}}^2 + \sigma_{\text{sensor}}^2 + \sigma_{\text{loc}}^2 \quad (2.5)$$

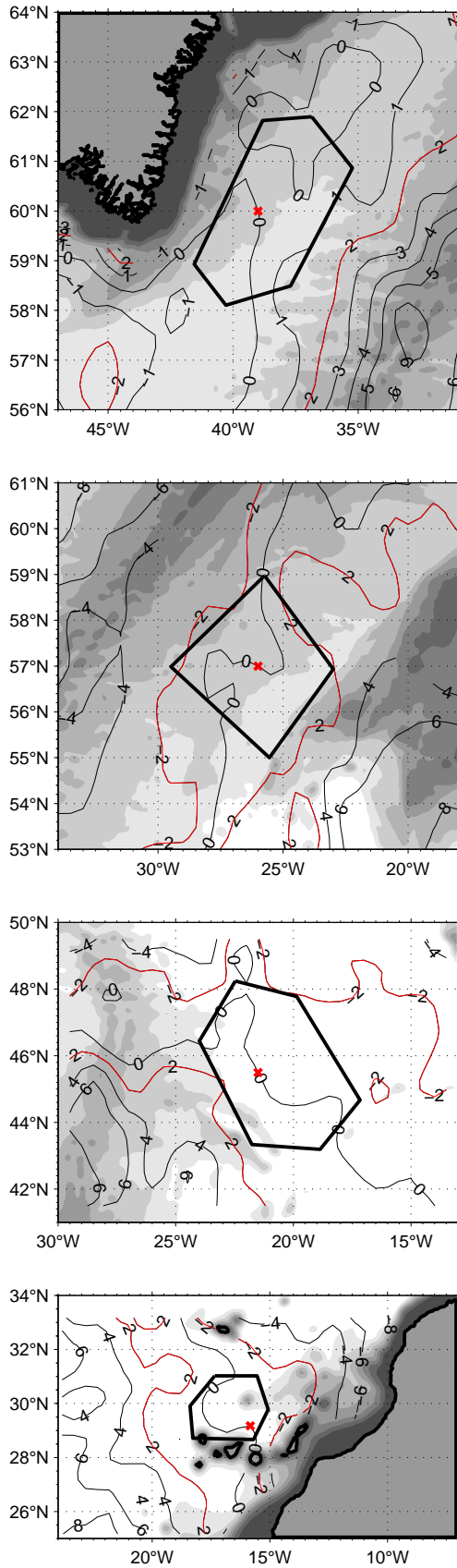


Figure 2.5: On the design of the polygons (cf. figure 2.1) and the location offset error of section 2.4.2,  $\sigma_{loc}$ . Contours show transport error in Sv relative to the locations of the red crosses, based on climatological hydrography (NODC (Levitus) World Ocean Atlas) referenced to 1000 m. Red contours highlight the isoline at 2 Sv. Polygon layout is such that associated transport error is below 2 Sv. From these figures, the value of  $0.01 \frac{\text{Sv}}{\text{km}}$  for the location error was derived.

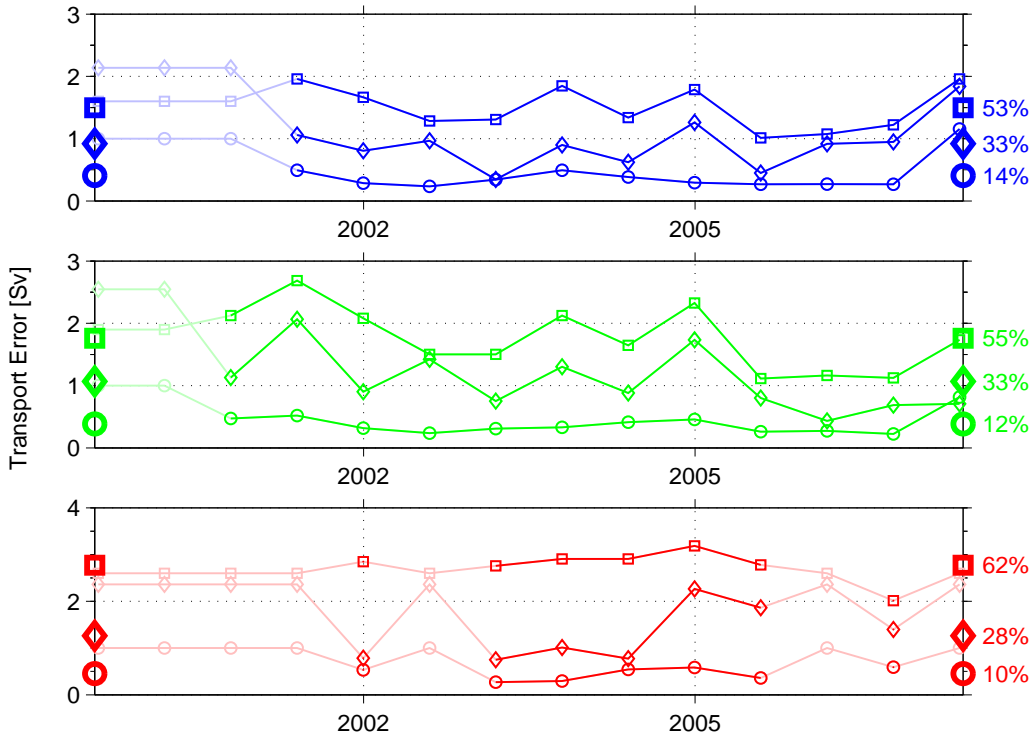


Figure 2.6: Individual error terms for the transports of figure 2.3 as described in section 2.4.2. Each panel/color corresponds to one section. *Circles*: Uncertainty due to natural variability,  $\sigma_{\text{eddy}}$ . *Squares*: Uncertainty due to sensor offset,  $\sigma_{\text{sensor}}$ . *Diamonds*: Uncertainty due to location offset,  $\sigma_{\text{loc}}$ . For times without data, defaults are shown in pale colors. Thick symbols at the sides represent means for times when data was available. Percentages at the right edge refer to ratios of these mean values. For all sections,  $\sigma_{\text{sensor}}$  introduces the largest uncertainties.

Figure 2.6 shows the temporal evolution of the three individual terms for each section. The average ratio of the three terms turns out to be:

$$\sigma_{\text{sensor}} : \sigma_{\text{loc}} : \sigma_{\text{eddy}} = 57\% : 31\% : 12\% \quad (2.6)$$

Uncertainties in the satellite altimetry are neglected because they are expected to be small due to the large areas and long time intervals over which the data are averaged: assuming that each polygon has space for 4 independent measurements and that there are measurements every 7 days results in approximately 100 degrees of freedom for each half-year interval. Accordingly, the formal mapping error of the altimeter product (typically 10% in the open ocean) is reduced to near 1%.

Error estimates in the mean dynamic sea surface height in figure 2.3 are based on the residual error estimate of 3.7 cm for the entire Atlantic by NILER ET AL. (2003), but our observations indicate that the error might be smaller. Anyhow, it can only influence the transports as a constant offset but has no effect on the variability seen in the figure, hence the separate error bars at the side.

## 2.5 Concluding Remarks

The geostrophic method is applied to three sections in the North Atlantic to derive volume transports of the currents across them, motivated by the relevance of these currents for European climate. The mean transports are found to be 5 Sv, 20 Sv, and 8 Sv (sections across the Irminger Current, North Atlantic Drift Current, Azores Current, resp.). Variability of the former two up to  $\pm 3$  Sv is documented on interannual time scales, mainly in anti-phase with a period near 2–3 years dominating the observational period 2001–2006. The results demonstrate the potential of the existing ocean observation systems, in particular when combining several sources of data. As an outlook into the future, one may hope for longer time series which enable a look at decadal time scales and bring the discussion closer yet to climate studies in a global sense. Two obvious next steps, however, would be to use the results as benchmarks for numerical models and to apply the methodology to other regions of interest.

## Chapter 3

# RAFOS Float Observations at Intermediate Depths in the Northeastern Atlantic Ocean

The circulation of the northeastern Atlantic Ocean at intermediate depths is characterized by water mass transformation processes that involve Iceland Scotland Overflow Water (ISOW) from the northeast, Labrador Sea Water (LSW) from the west, and Mediterranean Water from the south. Field observations from 89 eddy-resolving floats (RAFOS and MARVOR types) are analyzed. The trajectories show typical pathways of the water masses involved and the role that the complex bottom topography plays in defining them. Properties of the mesoscale eddy field show areas of intensified activity in the subpolar parts of the northeastern Atlantic, with cyclonic eddies being particularly energetic features. Interest in spreading paths and transformation processes of both LSW and ISOW is motivated by the role they play in the Meridional Overturning Circulation (MOC): both are components of the North Atlantic Deep Water, which makes up the cold reflux branch of the MOC.

This chapter reproduces parts of the following manuscript: LANKHORST AND ZENK (2006, © American Meteorological Society (AMS), reproduced by general permission to the author). Another publication briefly touches on individual trajectories and spreading routes of ISOW that are also discussed here: LANKHORST AND ZENK (2007).

### 3.1 Introduction

Between 1997 and 2002, 68 RAFOS floats were launched in the northeastern Atlantic as part of the *Sonderforschungsbereich* SFB 460 A3 research program. The main focus of the campaign was on water mass transformation in the Iceland Basin, but some floats also dispersed into the adjacent basins. Most of the instruments drifted isobarically at 1500 dbar, while a few were at 2600 dbar. A data report is available online (LANKHORST ET AL., 2004). Beginning in 1996, the Eurofloat project put floats in the subtropical northeastern Atlantic at different depths, amongst which were 21 floats of the MARVOR type drifting nominally at 1750 dbar. The shallower SFB floats (1500 dbar) nicely line up with the MARVOR instruments at 1750 dbar from Eurofloat, which had their main focus on the West European Basin further south. Together, these two data sets provide an unprecedented data coverage

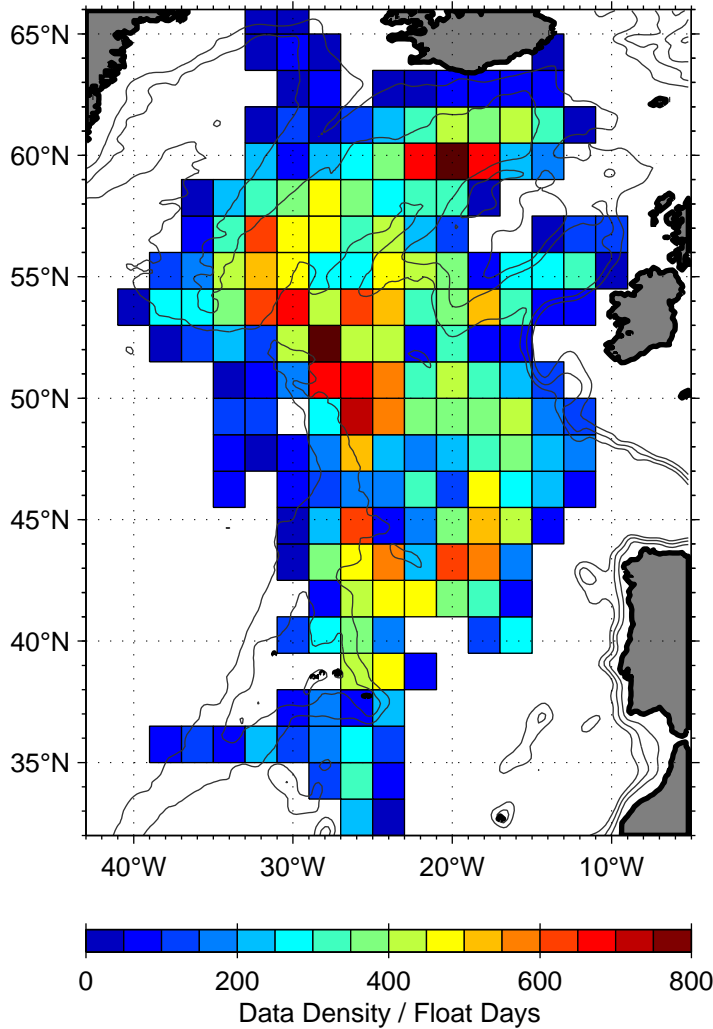


Figure 3.1: Data coverage by RAFOS floats from SFB 460 A3 at 1500 dbar and MARVOR floats from Eurofloat at 1750 dbar. Two SFB floats launched near Denmark Strait and eight floats at greater depths (2600 dbar) are not included. Dark red boxes indicate values beyond the color scale. Values are given in cumulative days of float data in boxes of  $1.5^\circ$ -by- $2^\circ$  (latitude/longitude) extent. Overall, the Iceland Basin and most of the West European Basin are well-sampled. Adapted from LANKHORST AND ZENK (2006, © AMS).

spanning virtually the entire northeastern Atlantic between the Azores and Iceland, as shown in figure 3.1.

Figure 3.2 illustrates the mean circulation by a selection of trajectories from 1500 dbar, essentially supporting the schematic diagram of figure 1.2. At that depth, the Iceland Basin is filled with a cyclonic gyre, which is fed by LSW through Charlie-Gibbs Fracture Zone (CGFZ) and by ISOW entering near the Faroe Islands. LSW is formed by winter convection in the Labrador Sea, while ISOW is an end product from cooling processes in the Nordic Seas spilling southward over the ridge, mainly through Faroe Bank Channel. The trajectories in the figure show the cyclonic circulation around the Iceland Basin, as well as a leakage of LSW southward into the West European Basin and a leakage of ISOW through gaps in the Reykjanes Ridge westward. In particular Bight Fracture Zone (BFZ) near  $57^\circ$  N seems to be a permanent escape route, in contrast to the traditional concept involving CGFZ. A few trajectories highlight the downstream path of the overflow waters following the topography all the way around the subpolar gyre and eventually into the Labrador Sea. On this path, additional overflow waters from Denmark Strait are entrained, and the eddy-rich detachment of the boundary current southwest of Greenland is also observed. A more detailed display of the mean circulation deduced from these float observations has

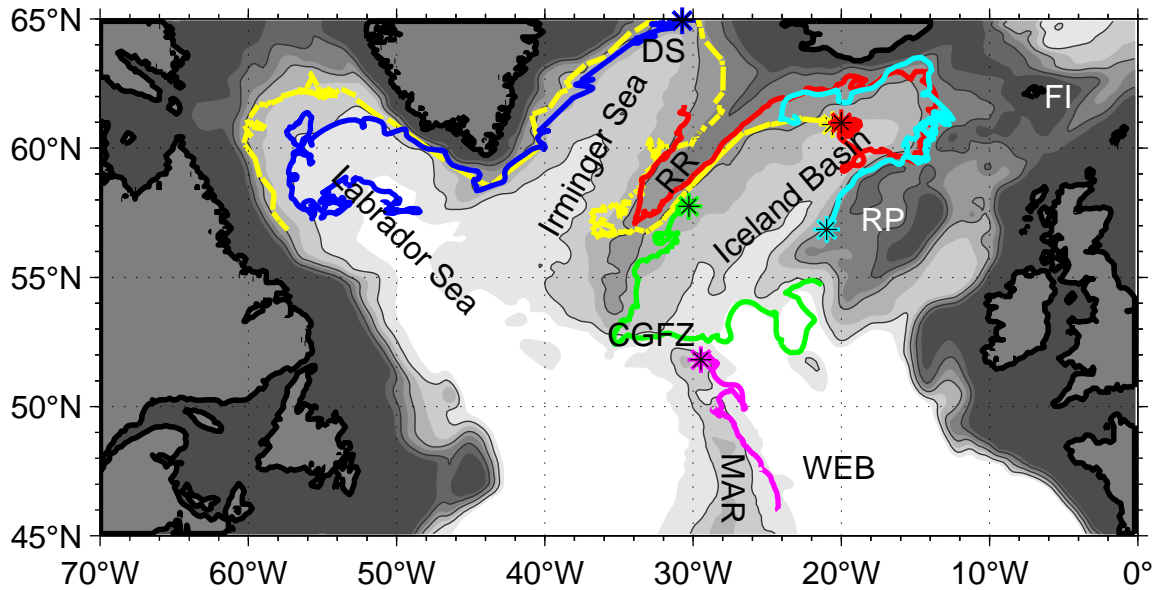


Figure 3.2: Selected float trajectories in the North Atlantic at 1500 m depth. Trajectories start at the asterisks. *Yellow*: Argo float 6900186, mission length 4 years. *Other colors*: RAFOS floats from SFB 460 A3, mission lengths 1–2 years. Abbreviations refer to topographic features: CGFZ Charlie-Gibbs Fracture Zone, DS Denmark Strait, FI Faroe Islands, MAR Mid-Atlantic Ridge, RP Rockall Plateau, RR Reykjanes Ridge, WEB West European Basin. Bathymetry is indicated by grey shading every 500 m and additional lines at 1000, 2000, and 3000 m.

been presented by BOWER ET AL. (2002) and discussed by LANKHORST AND ZENK (2006) and will not be repeated here. Instead, the following paragraphs will discuss a selection of trajectories in nine kinematically distinct regions and the mesoscale variability derived from the float observations, which continues the earlier analysis by LANKHORST (2003) to include revised analysis techniques and data collected since then. Integral properties of the mesoscale eddy field (e. g. time and length scales) will be presented and related to properties of individual eddy events to gain insights into the water mass transformation processes targeted in the SFB 460 A3 program.

## 3.2 Selected Trajectories

Figure 3.3 shows a map of the northeastern Atlantic with nine regions of special interest along the float pathways. The figure also provides detailed bathymetry and names of geographic features referred to in the text. Velocity data observed in these regions is comprehensively summarized in table 3.1.

Region 1 in the northeastern Iceland Basin is where ISOW enters the basin in a jet-like manner through Faroe Bank Channel. The highest velocities of the entire study area are consequently found here. Individual displacements exceeding  $60 \text{ cm s}^{-1}$  are observed, while large variability occurs as floats enter and leave the jet. LANKHORST AND ZENK (2006) give several examples where individual floats measured large temperature jumps, indicative

	Min.	Max.	Mean	Median	Std. Dev.
Region 1					
$u$	-43.73	27.11	1.36	4.98	15.69
$v$	-30.26	51.82	7.29	4.58	18.84
$ (u, v) $	3.06	67.81	20.89	17.41	14.45
$u_{\parallel}$	-24.77	42.91	7.42	5.42	16.45
$u_{\perp}$	-32.20	52.50	-0.00	-3.68	18.17
Region 2					
$u$	-22.31	3.53	-7.68	-7.48	4.55
$v$	-25.33	10.61	-6.66	-6.73	5.50
$ (u, v) $	1.08	28.13	11.21	11.03	5.35
$u_{\parallel}$	-3.23	27.82	10.16	10.06	5.69
$u_{\perp}$	-14.99	13.01	-0.00	0.48	4.31
Region 3					
$u$	-17.66	13.79	-1.73	-1.57	3.85
$v$	-16.38	13.06	-2.28	-2.18	3.96
$ (u, v) $	0.15	18.45	5.32	4.80	3.22
$u_{\parallel}$	-10.62	16.35	2.86	2.77	4.00
$u_{\perp}$	-14.41	16.92	-0.00	0.04	3.81
Region 4					
$u$	-22.11	33.14	3.80	2.98	8.65
$v$	-29.45	20.89	0.12	0.02	7.11
$ (u, v) $	0.32	44.33	9.64	7.86	6.84
$u_{\parallel}$	-22.18	32.22	3.80	3.03	8.63
$u_{\perp}$	-30.45	20.99	-0.00	-0.10	7.13
Region 5					
$u$	-7.05	13.45	0.57	0.43	2.74
$v$	-10.55	10.84	-0.77	-0.76	2.63
$ (u, v) $	0.10	13.45	3.36	3.03	2.01
$u_{\parallel}$	-9.24	11.90	0.96	0.92	2.78
$u_{\perp}$	-8.60	12.14	-0.00	-0.17	2.59
Region 6					
$u$	-16.21	17.34	0.38	0.15	3.28
$v$	-21.24	16.60	-0.66	-0.67	3.47
$ (u, v) $	0.01	22.36	3.88	3.20	2.88
$u_{\parallel}$	-17.49	21.43	0.76	0.66	3.43
$u_{\perp}$	-20.57	16.04	0.00	-0.11	3.32
Region 7					
$u$	-14.77	24.13	0.51	0.26	5.06
$v$	-24.28	35.10	0.02	0.36	5.87
$ (u, v) $	0.17	36.63	6.55	5.79	4.17
$u_{\parallel}$	-14.70	23.60	0.51	0.28	5.01
$u_{\perp}$	-24.39	35.53	0.00	0.33	5.91
Region 8					
$u$	-31.31	42.50	0.49	-0.36	9.23
$v$	-25.80	40.96	0.39	0.08	7.93
$ (u, v) $	0.14	49.46	10.16	8.71	6.74
$u_{\parallel}$	-33.43	41.06	0.62	-0.32	8.86
$u_{\perp}$	-46.21	33.09	-0.00	0.38	8.35
Region 9					
$u$	-19.36	23.53	-2.34	-1.75	4.32
$v$	-15.52	16.98	-0.77	-0.46	3.58
$ (u, v) $	0.08	25.11	4.45	3.73	4.21
$u_{\parallel}$	-19.61	21.93	2.46	1.54	4.57
$u_{\perp}$	-15.83	15.70	0.00	0.14	3.25

Table 3.1: Statistics of float velocities in the regions shown in figure 3.3. Minimum, maximum, mean, median, and standard deviation are displayed for zonal and meridional velocities  $u$  and  $v$ , for scalar horizontal velocity  $|(u, v)|$ , and for a coordinate system rotated to yield velocity components along ( $u_{\parallel}$ ) and across ( $u_{\perp}$ ) the mean velocity. All numeric values are given in  $\text{cm s}^{-1}$ . An appropriate interpretation of mean kinetic energy (MKE) would be  $\text{mean}(u_{\parallel})^2/2$ , and of eddy kinetic energy (EKE)  $(\text{std}(u)^2 + \text{std}(v)^2)/2$ . Adapted from LANKHORST AND ZENK (2006, © AMS).



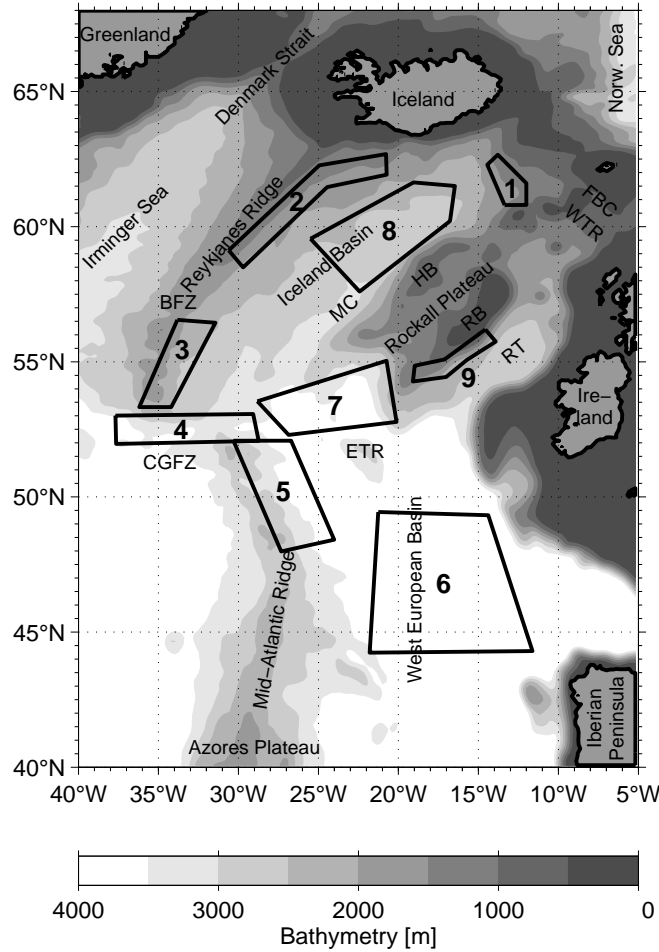


Figure 3.3: Map of the northeastern Atlantic with nine kinematically different regions of interest. Abbreviations of topographic features are: BFZ Bight Fracture Zone, CGFZ Charlie-Gibbs Fracture Zone, ETR East Thulian Rise, FBC Faroe Bank Channel, HB Hatton Bank, MC Maury Channel, RB Rockall Bank, RT Rockall Trough, WTR Wyville-Thomson Ridge. Adapted from LANKHORST AND ZENK (2006, © AMS).

of floats being exchanged between two different water masses. VAN AKEN AND DE BOER (1995) derive concentrations of these water masses for a hydrographic section in the area and verify them to be ISOW and LSW derivatives. ISOW then continues northwest, later westward, parallel to the bathymetry along the northern edge of the Iceland Basin.

Region 2 at the eastern flanks of Reykjanes Ridge highlights the downstream behavior of this jet. Flow is aligned strictly parallel to the ridge, which makes trajectories there look very “straight”, i. e. the ratio of eddy kinetic energy (EKE) versus mean kinetic energy (MKE) is low. Data from table 3.1 shows indeed that EKE is near  $25 \text{ cm}^2 \text{ s}^{-2}$ , whereas MKE is approximately  $50 \text{ cm}^2 \text{ s}^{-2}$ —quite in contrast to all other regions listed there, for which EKE is always greater than MKE. KRAUSS (1995) report strong entrainment in this region, increasing the volume transport of the consolidated overflow to 3.3 Sv.

Region 3 is further downstream yet, at the southern part of Reykjanes Ridge. By the time ISOW reaches this location, it has been subject not only to the entrainment processes,

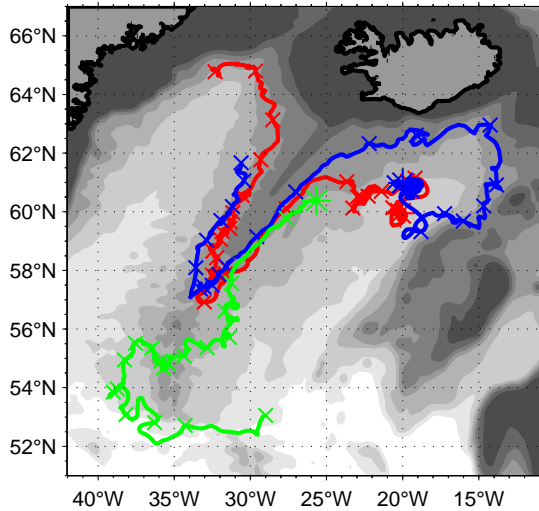


Figure 3.4: Three RAFOS trajectories at 1500 dbar, illuminating the characteristics of regions 1–4 of figure 3.3 (bathymetry identical). Trajectories begin at the asterisk symbols; additional ticks every 30 d. Adapted from LANKHORST AND ZENK (2006, © AMS).

but also to gradual sinking to greater depths, so that the floats at 1500 dbar represent only its upper part. Average velocities have dropped from just over  $10 \text{ cm s}^{-1}$  in region 2 to below  $3 \text{ cm s}^{-1}$  here, showing that the nature of the flow is not “jet-like” anymore, at least at the sampled depth. In this region, the ridge has multiple openings which allow the waters to pass across it into the Irminger Sea. A particularly large number of floats pass through Bight Fracture Zone near  $57^\circ \text{ N}$  (BOWER ET AL., 2002), well north of Charlie-Gibbs Fracture Zone (CGFZ,  $52\text{--}53^\circ \text{ N}$ ), which suggests that the naming convention of *Charlie Gibbs Fracture Zone Water* (amongst others, by SCHOTT ET AL. (1999)) is a little unfortunate at least for the waters at this depth. HANSEN AND ØSTERHUS (2000) already suggest that shallow portions of ISOW spill through fracture zones north of CGFZ, but mark this pathway with a question mark in their figure 6. The float observations here confirm these expectations.

Region 4 finally covers CGFZ. This large fracture zone is a key location for the circulation of the North Atlantic, hosting the North Atlantic Current (NAC) in the upper layers (BOWER ET AL., 2002; PÉREZ-BRUNIUS ET AL., 2004) and a major passage for exchange at greater depths. The fact that the NAC seems to be locked to this location has already been exploited in section 2, considering its downstream paths in the upper 1000 dbar, by selecting the measurement locations to either side of the region. Most of the floats at 1500 dbar record an eastward flow, averaging just below  $4 \text{ cm s}^{-1}$  (table 3.1). This represents the inflow of LSW into the eastern basins (cf. figure 1.2). Individual floats have recorded flow reversals towards either direction, indicative of variable spreading routes of the water masses under consideration here.

Figure 3.4 shows three exemplary trajectories to summarize the characteristics of regions 1–4: The float of the blue trajectory was eventually entrained into the ISOW jet west of Faroe Bank Channel (region 1) and followed along the Reykjanes Ridge, where the other two floats joined in, demonstrating the entrainment processes. Trajectories along the ridge (region 2) are swift and straight. Fracture zones in the southern Reykjanes Ridge (region 3) then allow for a transgression into the western basin. There, two trajectories follow the ridge back northwards, experiencing slower velocities which still lead the floats to the vicinity of Denmark Strait. The third float (green) returns to the eastern basin through CGFZ (region 4), thereby documenting this eastward pathway of LSW.

Region 5 on the eastern slopes of the Mid-Atlantic Ridge (MAR) south of CGFZ

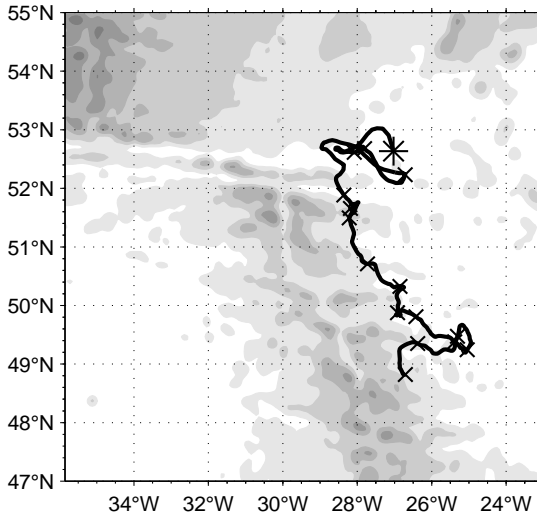


Figure 3.5: A RAFOS trajectory at 2600 dbar, documenting the flow of ISOW past CGFZ into the West European Basin. The trajectory starts at the asterisk; additional ticks are 30 d apart. Bathymetry as in figure 3.3. Adapted from LANKHORST AND ZENK (2006, © AMS).

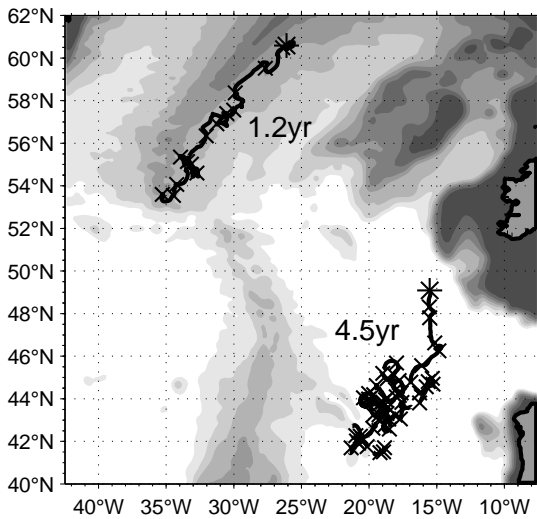


Figure 3.6: A RAFOS trajectory at 1500 dbar (north) and a MARVOR trajectory at 1750 dbar (south), documenting the differences in velocity between the two regions by their similar lengths but vastly different travel times. Trajectories start at the asterisks; additional ticks are 30 d apart. Interruptions in the southern trajectory are due to the surface intervals of the MARVOR float. Bathymetry as in figure 3.3. Adapted from LANKHORST AND ZENK (2006, © AMS).

contains one of several possible continuations of the eastward LSW path. Water is carried southeastward as a boundary current along the ridge at average velocities of  $1 \text{ cm s}^{-1}$ . The fact that the ridge is mostly deeper than the drift depth of the floats illustrates the importance of the topographic influence on the flow field. However, even at greater depth, a float at 2600 dbar documents southeastward flow there (figure 3.5). This shows that a fraction of ISOW can flow past the gaps in the MAR and ventilate the West European Basin.

Region 6 is located in the interior of the West European Basin, an area sampled mainly by the Eurofloat project. The average velocity is southwestward, but very slow near  $0.8 \text{ cm s}^{-1}$ . EKE is also low in the area, so that it is best characterized as a region of slow, sluggish motion. An illustration of this slowness is given by figure 3.6, which compares a trajectory from this region with one of regions 2 and 3. Both floats travelled over similar distances, but the southern one needed 4.5 years while the northern one lasted just over one year.

Region 7 east of CGFZ contains a pathway of LSW further eastward than the immediate vicinity of the MAR (cf. figure 1.2). Mean velocity is low ( $0.5 \text{ cm s}^{-1}$ ) and zonal. In this

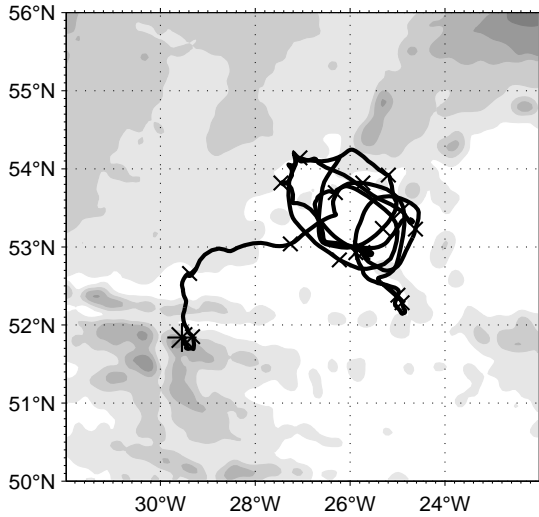


Figure 3.7: A RAFOS trajectory at 1500 dbar in a long-lived (444 d) anticyclonic eddy. The trajectory starts at the asterisk; additional ticks are 30 d apart. Bathymetry as in figure 3.3. Adapted from LANKHORST AND ZENK (2006, © AMS).

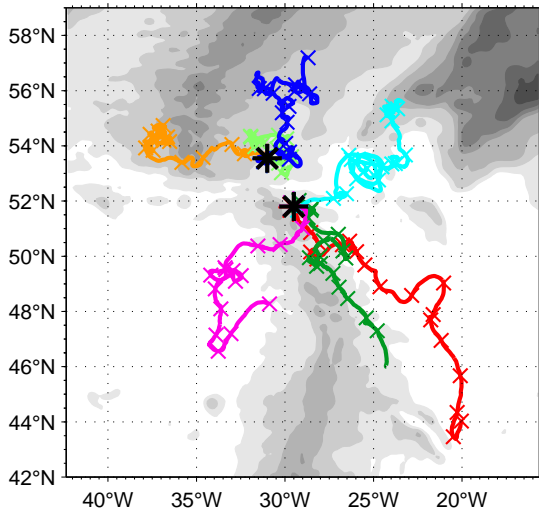


Figure 3.8: RAFOS trajectories at 1500 dbar launched east of CGFZ. Although start points are close to each other, very different spreading pathways are observed. The trajectories start at the black asterisks; additional ticks are 30 d apart. Bathymetry as in figure 3.3. Adapted from LANKHORST AND ZENK (2006, © AMS).

location, several large and long-lived anticyclones have been repeatedly observed in the trajectories, one example of which is given in figure 3.7. The float looped in the anticyclone for 444 d; superimposed on this clockwise motion are wiggles on shorter time scales caused by smaller eddies. This coincides with anticyclones of similar extent found mainly closer to the surface by MARTIN ET AL. (1998) and PINGREE AND LE CANN (1991).

Figure 3.8 shows multiple trajectories beginning at two locations at the eastern openings of CGFZ. The floats were moored and released successively with the *float park* technique introduced by ZENK ET AL. (2000). The southern trajectories document the pathways described for regions 5 and 7, ventilating the West European Basin. Three of the four southern floats began southeastward along the ridge, while the fourth one travelled eastward and was trapped in one of the large anticyclones of region 7. The northern floats show flow towards the Iceland Basin, but also in westward direction, repeating the point of high variability made for region 4.

Region 8 is situated in the central Iceland Basin. Exemplary trajectories are documented in figure 3.9 and reveal intense eddy activity superimposed on low mean propagation, as already obvious from table 3.1. In fact, EKE values are the second highest of all the

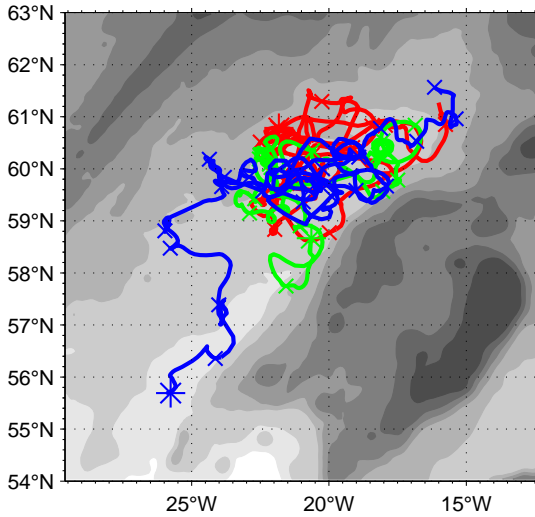


Figure 3.9: RAFOS trajectories at 1500 dbar in the central Iceland Basin show intense eddy activity. The trajectories start at the asterisks; additional ticks are 30 d apart. Bathymetry as in figure 3.3. Adapted from LANKHORST AND ZENK (2006, © AMS).

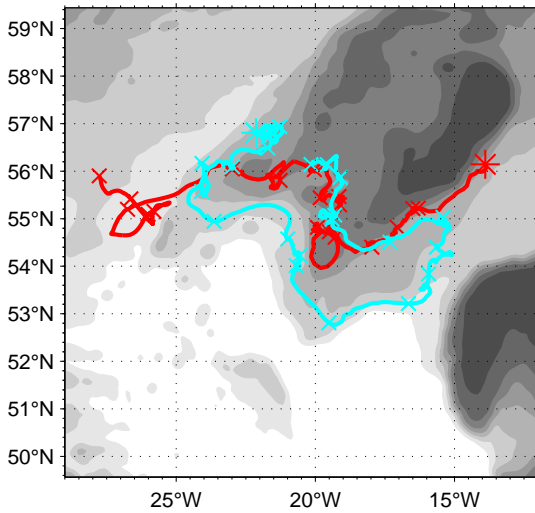


Figure 3.10: RAFOS trajectories at 1500 dbar south of Rockall Plateau document a boundary current adjacent to the plateau. The trajectories start at the asterisks; additional ticks are 30 d apart. Bathymetry as in figure 3.3. Adapted from LANKHORST AND ZENK (2006, © AMS).

regions (circa  $80 \text{ cm}^2 \text{ s}^{-2}$ ), whereas the mean velocity is northeastward at only  $0.6 \text{ cm s}^{-1}$ . This is in sharp contrast with the immediately neighboring region 2, where MKE is high and EKE low. As will be discussed in the section on the mesoscale eddy field, region 8 seems to be a prime region for water mass transformation involving LSW and ISOW.

Region 9 covers the southern edge of Rockall Plateau. A few trajectories (figure 3.10) show a boundary current flowing westward along the plateau. This would transport portions of ISOW that have leaked into Rockall Trough over Wyville-Thomson Ridge as opposed to following Faroe Bank Channel, and thus provide another pathway for ISOW into the Iceland Basin. This pathway has also been suggested by HANSEN AND ØSTERHUS (2000, their figure 6), and again the floats confirm their expectations by direct observations. Mean westward velocities are not slow ( $2.5 \text{ cm s}^{-1}$ ) but derived from few float observations only. The figure also shows a narrow eastward recirculation cell, which contributes to the LSW pathways seen in region 7.

### 3.3 The Mesoscale Velocity Field

In this section, the mesoscale variability of the velocity data from the floats is discussed. As integral properties, the Lagrangian integral time scale and EKE are the quantities to study. A corresponding length scale and diffusivity can be derived from these. All computations and data processing are described in section 3.4. The underlying theory is that of homogeneous and isotropic turbulence introduced by TAYLOR (1921) and repeatedly applied in physical oceanography (KRAUSS AND BÖNING, 1987; LUMPKIN ET AL., 2002). With the high data density achieved, the above properties are mapped with unprecedented resolution, extending previous data coverage at mid-depth (LUMPKIN ET AL., 2002) over almost the entire northeastern Atlantic north of  $35^\circ$  N, in the hope that the maps are particularly useful for comparison with computer models. The region features the transition line between the subpolar and subtropical regimes (region AA' in figure 19 of KRAUSS, 1986), which results in readily apparent contrasts of the mesoscale quantities. To relate these integral quantities to individual eddy events, an attempt is made to auto-detect eddies according to whether trajectories are “looping” or not. Because the floats used were designed to drift approximately isobarically, the entire following discussion assumes horizontal motion.

#### 3.3.1 Eddy Kinetic Energy, Integral Time Scale, and Derived Quantities

Although studies of EKE occur fairly frequently in the literature, the author is aware of only one subsurface map of this quantity in the Iceland Basin derived from float observations (LAVENDER ET AL., 2005). There, profiling floats are used to derive EKE and time scales, which will be shown to be inappropriate due to the poor temporal resolution of these instruments here. BOWER (2003) showed such maps derived via acoustic floats in a conference presentation, including the data from this study, but they had to be skipped in the accompanying article (BOWER ET AL., 2002). LUMPKIN ET AL. (2002) present maps of the Lagrangian integral time and length scales as well as diffusivity, but not of EKE. They do, however, explain the relationship between Lagrangian and Eulerian eddy properties, which may be of interest to the readers who are less familiar with float observations. Their data source already contains early versions of the Eurofloat data set, but not the SFB floats, so that their maps lack the Iceland Basin. Figure 3.11 shows a map of the Lagrangian EKE throughout the entire northeastern Atlantic derived from the data sets of the present study (nominally 1500–1750 dbar). Overall, values range from below  $10 \text{ cm}^2 \text{ s}^{-2}$  to beyond  $100 \text{ cm}^2 \text{ s}^{-2}$ . Compared to the western basin, EKE values are generally lower (typically less than  $50 \text{ cm}^2 \text{ s}^{-2}$ ), with three exceptions of increased EKE:

1. Highest values are found in the immediate “impact region” of ISOW in the far northeastern corner of the Iceland Basin. In this location, ISOW enters the Iceland Basin at relatively high velocities through Faroe Bank Channel. EKE values around  $100 \text{ cm}^2 \text{ s}^{-2}$  are found and apparently related to variability of the inflowing jet of ISOW, as shown in the previous section for region 1 there.
2. A much larger and better-resolved area is found in the central Iceland Basin at Maury Channel (deepest portion of the Iceland Basin) northwest of Hatton Bank (part of Rockall Plateau). EKE values of circa  $80 \text{ cm}^2 \text{ s}^{-2}$  are observed there, and individual trajectories appear highly “wiggly” to the naked eye (cf. region 8 of previous section and figure 3.9). The position of this EKE maximum is identical with spots of increased

EKE at the sea surface documented by HEYWOOD ET AL. (1994) and BERSCH (1995), both using altimeter data. Combining these with the float measurements, one sees that there is intensified mixing even below the near-surface North Atlantic Current which causes the higher EKE in altimetric data. This area seems to be a sink region for LSW, and the high EKE is the imprint of it being mixed with surrounding waters. In particular, there seems to be an influence by ISOW leaking over Wyville-Thomson Ridge, which is supported by salinity data from CTD lines (LANKHORST AND ZENK, 2006).

3. Another maximum of similar amplitude lies in and just west of CGFZ (region 4), but as this is the limit of the data coverage, nothing can be said about its extension further west (i. e. upstream along the NAC, which is located at depths in the upper 1000 m). This zone coincides directly with a tongue of increased kinetic energy derived by KRAUSS AND KÄSE (1984) from near-surface drifters ( $300\text{--}400\text{ cm}^2\text{ s}^{-2}$  near CGFZ) and by OWENS (1991) from SOFAR floats in 700 ( $440\text{ cm}^2\text{ s}^{-2}$  farther to the west at  $39^\circ\text{ N}$ ,  $55^\circ\text{ W}$ ) and 2000 m depth ( $120\text{ cm}^2\text{ s}^{-2}$ ). Apparently, the position of the highly energetic strip is defined by the North Atlantic Current and the subpolar front (ROSSBY, 1999). The variability in the immediate vicinity of CGFZ originates from the two water masses LSW and ISOW, tending towards opposite directions through the same gap. Flow reversals are therefore common and cause high EKE. Whether these are triggered by the location of the NAC and whatever happens further west is subject to ongoing research (SCHOTT ET AL., 1999; BOWER AND VON APPEN, 2006).

In the West European Basin, the low EKE of  $1\text{--}10\text{ cm}^2\text{ s}^{-2}$  reveals this to be a region of sluggish motions (region 6), although individual intense eddy events have been observed. The EKE map obtained by LAVENDER ET AL. (2005, their figure 17) from profiling floats, adjusted to depths near 700 m, fails to reproduce the high values in the Iceland Basin discussed here. Without any difference between the Iceland and the West European Basin, they find EKE to be near  $25\text{ cm}^2\text{ s}^{-2}$ , with a local maximum exceeding  $50\text{ cm}^2\text{ s}^{-2}$  southwest of Rockall Plateau. In the western basin, however, they find larger values, but still significantly below those reported from the other studies mentioned previously (a maximum of  $125\text{ cm}^2\text{ s}^{-2}$  near Flemish Cap compared to the  $440\text{ cm}^2\text{ s}^{-2}$  from SOFAR floats). The problem underlying the discussion of mesoscale variability using profiling floats is obviously that they do not resolve the mesoscale eddies. Therefore, it is important to consider the typical time scales of the flow field.

The Lagrangian integral time scale is a measure of the time it takes until the velocity of a float is no longer correlated with itself. With plots of a power spectrum in mind, one can interpret EKE as an average of the energy level (i. e. the vertical axis), and the integral time scale as an average of the frequencies (i. e. the horizontal axis) that carry significant amounts of energy.

In earlier literature, Lagrangian integral time scales around 10–12 d (MODE (mid-ocean dynamics experiment), FREELAND ET AL., 1975) and 7 d (POLYMODE area, ROSSBY ET AL., 1986b) have been reported for the open ocean at depths close to 1500 m. KRAUSS AND BÖNING (1987) derive values of circa 2–8 d for surface drifters with drogues at 100 m depth.

Figure 3.11 also shows the Lagrangian integral time scale. The plot contrasts values around 3 d in the Iceland Basin to those around 8 d in the West European Basin further south. The latter agrees well with results by LUMPKIN ET AL. (2002), although the extension

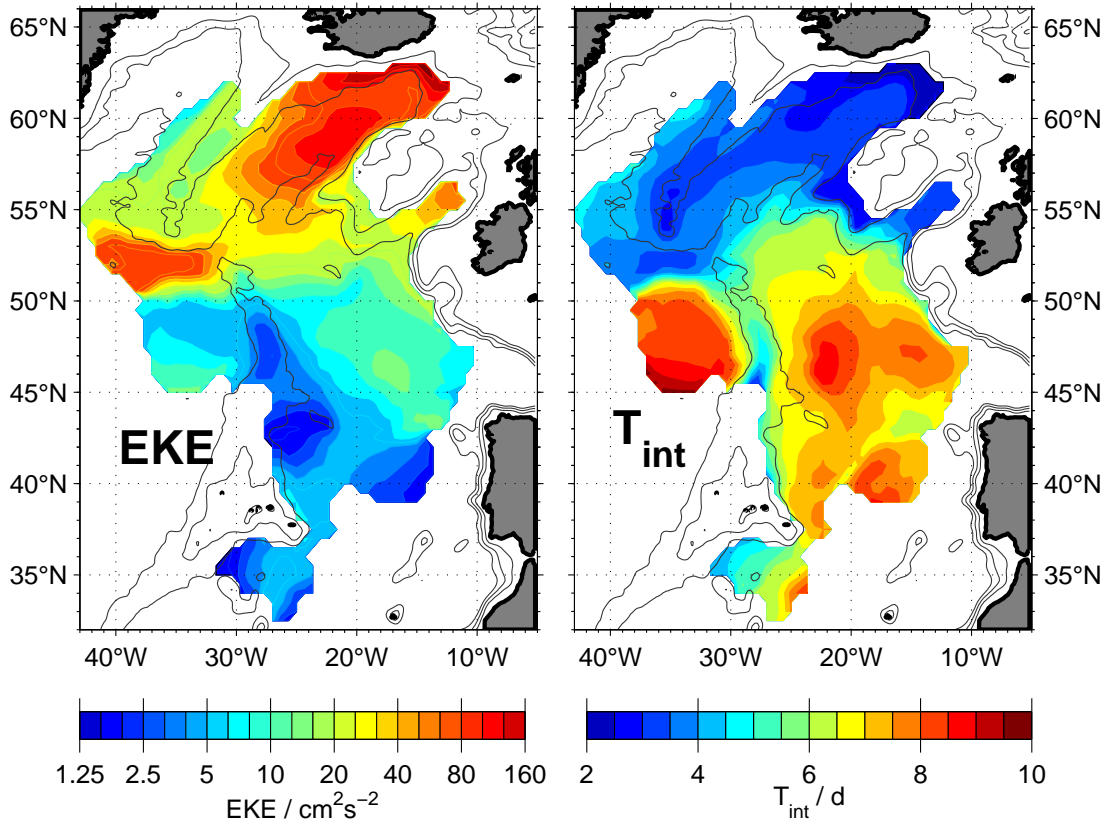


Figure 3.11: Lagrangian eddy kinetic energy (EKE, left) and integral time scale ( $T_{\text{int}}$ , right) at nominal depths of 1500–1750 m in the northeastern Atlantic. High EKE and short time scales in the central and northeastern Iceland Basin are in contrast with low EKE and longer time scales in the European Basins and around the Azores. Note that the color scale for the EKE plot is logarithmic. Bathymetry is shown at 1000, 2000, and 3000 m. Adapted from LANKHORST AND ZENK (2006, © AMS).

of the data set with the SFB floats into the Iceland Basin completes the side-by-side view of the two basins. Within the Iceland Basin, the time scales reach their lowest values of circa two days in the northeastern part, north of Hatton Bank. As the data is low-pass filtered with a cut-off period at 3 d, the actual values are likely to be even smaller. As expected, the area of the shortest time scales coincides with that of highest EKE, again indicating strong turbulent activity in the area. Generally, one would expect lower values in the subpolar areas, since the nature of the flow is more barotropic there, and thus the influence of the more rapidly changing near-surface motions is stronger at greater depths. However, the sudden drop at the line connecting CGFZ with Rockall Plateau—where the subpolar and subtropical gyres meet—remains remarkable.

The longer time scales in the West European Basin further south again confirm the impression of a more quiescent regime, which misses variability at the high-frequency part of the spectrum when compared to the subpolar areas.

The few values available from the western basin southwest of CGFZ (i. e. in the subtropical gyre) are around 8 d as well, not at disagreement with the early observations of MODE and POLYMODE. The short time scales following the Mid-Atlantic Ridge system



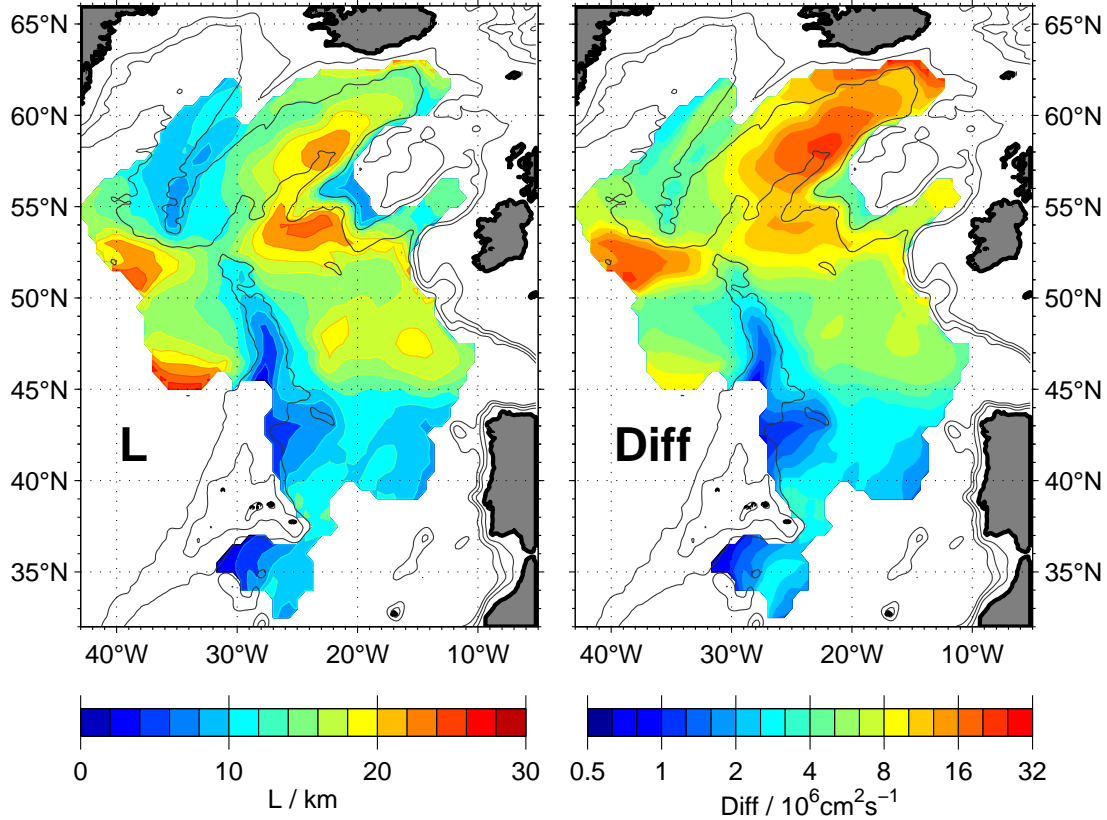


Figure 3.12: Lagrangian length scale ( $L$ , left) and horizontal diffusivity ( $\text{Diff}$ , right) at nominal depths of 1500–1750 m in the northeastern Atlantic. Longest length scales are found southwest of Rockall Plateau and west of CGFZ, while length scales directly above the MAR are shortest. Highest diffusivities are found in the central Iceland Basin, whereas the West European Basin typically has low values. Note that the diffusivity color scale is logarithmic. Bathymetry is shown at 1000, 2000, and 3000 m. Adapted from LANKHORST AND ZENK (2006, © AMS).

show how bathymetry confuses the flow one would otherwise see, quickly reducing (temporal) autocorrelation as the trajectories move from one obstacle to the next. This can be seen at depths significantly shallower than the depths of the obstacles themselves.

With these time scales, it becomes obvious why the profiling floats utilized by LAVENDER ET AL. (2005) must fail to resolve the mesoscale eddies, resulting in crude overestimations of the actual time scales and underestimation of the EKE. The average displacement duration of the profiling floats is 9.6 d, significantly larger than the time scales of down to 3 d identified here, which in fact is already at the limit of what the *acoustic* floats have resolved. The discrepancy between their results and those presented here is worst in the Iceland Basin, indeed where the shortest time scales are. The area southwest of Rockall Plateau (region 7 here) is their local maximum because time scales there are sufficiently large to be resolved, as is the case for the sluggish West European Basin.

Knowing EKE and the time scale, one can compute a corresponding length scale and a horizontal diffusivity estimate from these (cf. section 3.4). The Lagrangian length scale can be interpreted as a representative eddy size and is of similar order as the first baroclinic

Rossby radius. Figure 3.12 shows this length scale calculated accordingly, again extensively enlarging the database compared to that of LUMPKIN ET AL. (2002). Throughout the entire study area, the Lagrangian length scale is on the order of ten kilometers, with highest values of 20–25 km west of CGFZ and around Rockall Plateau. The maximum southwest of Rockall Plateau coincides with a region where several large anticyclones were observed (region 7 of previous section). On either side of the MAR, values are circa 10–15 km, and the shortest length scales of about 5 km are observed directly north of the Azores Plateau.

As the meaning of the horizontal diffusivity estimate is strongly restricted by the assumptions of homogeneity and isotropy of the eddy field, it may only be interpreted safely in the interior parts of the basins. Figure 3.12 also shows the horizontal diffusivity. The general distribution of this quantity follows the EKE pattern, because EKE is subject to larger spatial fluctuations in the area than the time scale, and the diffusivity estimate is simply the product of both. Within the Iceland Basin, its spatial distribution is complex, spanning a range of circa  $5\text{--}22 \cdot 10^6 \text{cm}^2 \text{s}^{-1}$ . The highest values are observed in the central Iceland Basin northwest of Hatton Bank, confirming that this is the primary location for transformation of water masses at mid-depth in the northeastern Atlantic. Another maximum of nearly equal amplitude is located west of CGFZ (see discussion of EKE above). Virtually the entire West European Basin is characterized by very low values ( $< 8 \cdot 10^6 \text{cm}^2 \text{s}^{-1}$ ).

In addition to the bulk of the SFB floats near 1500 dbar in the eastern basins, data from two floats at that depth in the western basin and eight deeper ones near 2600 dbar in the eastern basin are available. Figure 3.13 shows EKE and Lagrangian integral time scale computed for the two western floats. They were launched in Denmark Strait and advected into the Labrador Sea by the boundary currents around Greenland. While in the swift boundary current, the floats encounter EKE values of  $150 \text{cm}^2 \text{s}^{-2}$ . In the inner parts of the Labrador Sea, these values drop to  $30\text{--}50 \text{cm}^2 \text{s}^{-2}$ . Corresponding time scales are all below 4 d, indicating that these results are already affected by the temporal resolution of the float data (one position per day). Nevertheless, a localized minimum in the time scale and a maximum in the EKE near  $58^\circ \text{N}$  and  $55^\circ \text{W}$  is visible in the plot, which occurred in January/February 2000. This might be the imprint of vigorous mixing associated with wintertime convection.

The data amount from the eight deeper floats is sufficient to produce mapped fields of EKE and time scale, shown in figure 3.14. The overall distribution is remarkably similar to that of the shallower floats shown in figure 3.11, with highest values of EKE and shortest time scales in the central Iceland Basin and vice versa in the West European Basin. Just like near 1500 dbar, EKE can exceed  $100 \text{cm}^2 \text{s}^{-2}$  at time scales below 3 d, indicating intense mesoscale activity in the region.

### 3.3.2 Coherent Eddies

As discussed in the previous section, the Iceland Basin features high EKE and short time scales, indicative of enhanced turbulent mixing. A closer look at discrete eddies in the area at shallower depths has been performed by SHOOSMITH ET AL. (2005), who select float trajectories with looping parts by visual inspection. Their data set is reported to contain 19 anticyclones versus 18 cyclones in the Iceland Basin ( $c/a$  ratio 0.9) and 12 anticyclones and 7 cyclones in the West European Basin ( $c/a$  0.6). For the present study, an automatic detection scheme has been applied to identify looping trajectories (cf. chapter 4). Two

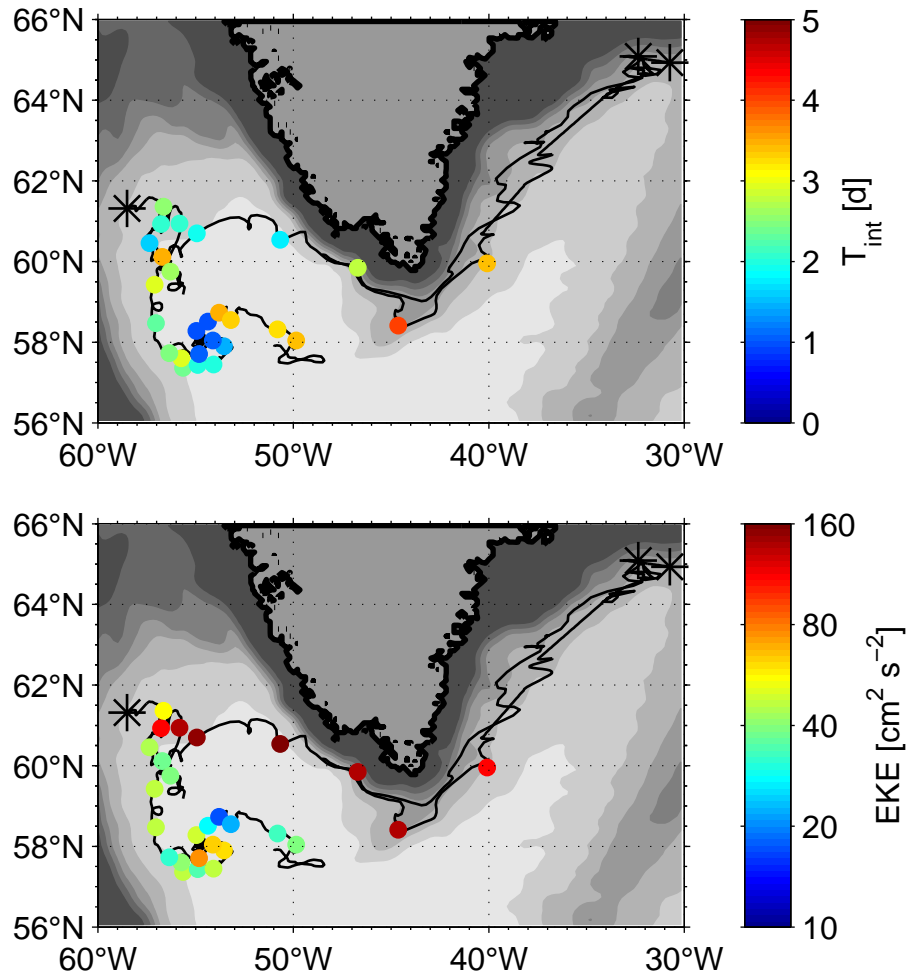


Figure 3.13: Data from two RAFOS floats from SFB 460 A3 at 1500 dbar launched in Denmark Strait. Trajectories begin at the asterisks. One float temporarily lost tracking; its trajectory is split in two. *Top*: Lagrangian integral time scale. *Bottom*: Lagrangian eddy kinetic energy (EKE). Both are computed along the trajectories in windows of 80 d duration overlapping every 20 d. Note that the EKE color scale is logarithmic. Data east of Greenland is partially removed due to poor tracking. Shading of bathymetry is in steps of 500 m.

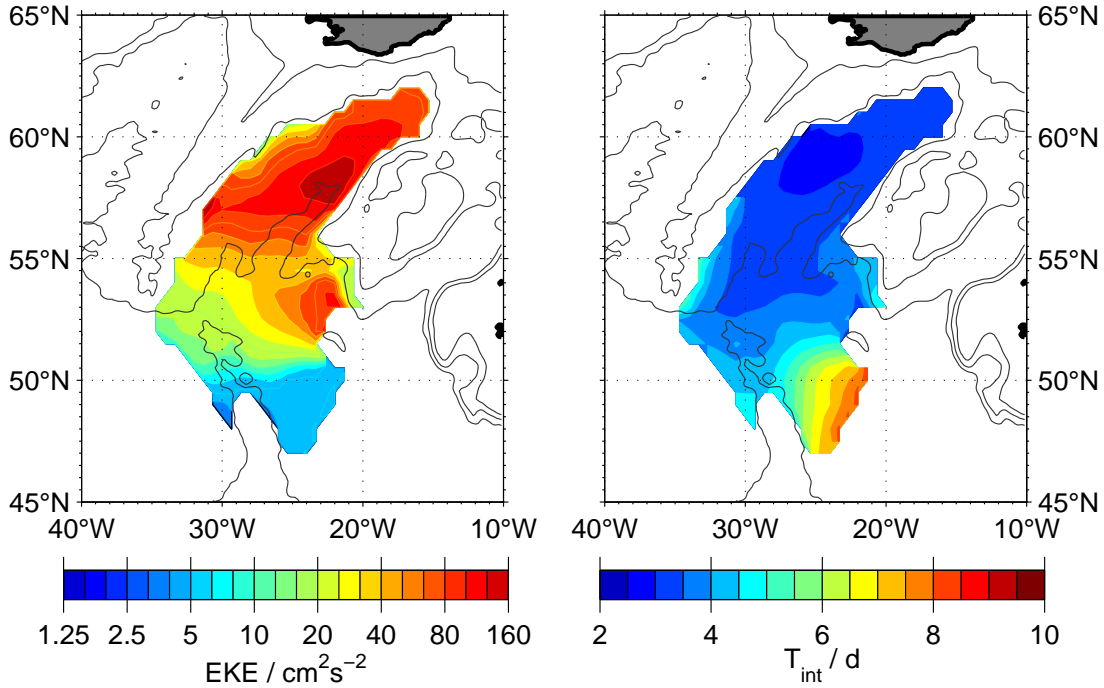


Figure 3.14: Lagrangian eddy kinetic energy (left) and integral time scale (right) derived from eight floats nominally drifting at 2600 dbar, otherwise as figure 3.11. The overall pattern resembles that found at 1500 dbar, with high EKE and short time scales in the Iceland Basin and vice versa further south. The EKE color scale is logarithmic. Bathymetry is indicated at 1000, 2000, and 3000 m.

completed revolutions are required to be counted as an eddy.

An analysis of SFB and Eurofloat trajectories confined to the Iceland Basin revealed 37 cyclones and 16 anticyclones using this method ( $c/a$  2.3). Of a total of 15968 days of trajectory data, 2222 (13.9%) were spent in cyclones, and 955 (6.0%) in anticyclones. While these percentages are obviously sensitive to the criteria applied during eddy detection, the ratio of cyclone days to anticyclone days ( $>2:1$ ) may be expected to be independent of these details. In the West European Basin, 43 cyclones and 28 anticyclones were identified ( $c/a$  1.5) among 23758 days of trajectory data. They were distributed among 1512 (6.4%) cyclone days and 1350 (5.7%) anticyclone days, respectively. The ratio of cyclone to anticyclone days is therefore down to almost 1:1. Figure 3.15 shows how the mean eddy periods are distributed. Especially at the shortest periods resolved, i. e. less than 10 d, the cyclones outnumber the anticyclones significantly in both basins. In relation to the total amount of data, the cyclonic eddies are significantly more abundant in the Iceland Basin than in the West European Basin. Compared to the findings by SHOOSMITH ET AL. (2005), more cyclonic vortices are found in both basins. A possible explanation is that the automatic detection also accepts quickly advected eddies, the trajectories of which are cusps rather than closed loops and therefore rejected by SHOOSMITH ET AL. (2005). It could be that these are more common in high-frequency eddies, and therefore that results by SHOOSMITH ET AL. (2005) are biased towards anticyclones in the direct comparison. PAILLET (1999) also found more anticyclones than cyclones in the Central Water using hydrographic section data, but his data does not cover the subpolar Iceland Basin, making a direct comparison

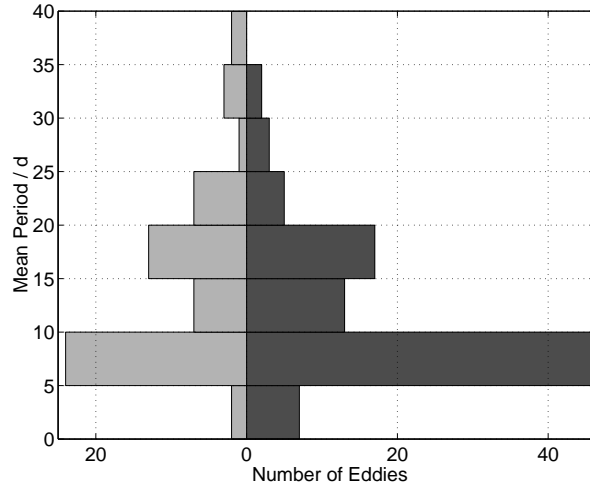


Figure 3.15: Histogram of mean eddy periods for auto-detected eddies in the entire study area. Data on anticyclones is in light grey, on cyclones in dark grey. At short periods ( $<10$  d), the cyclones outnumber the anticyclones significantly. Adapted from LANKHORST AND ZENK (2006, © AMS).

difficult.

Figure 3.16 shows spectra of the float velocity data, separated into Iceland and West European Basins. For each basin, separate spectra are displayed for the entire data set and for the extracted eddy segments within the trajectories. At first glance, it is obvious that the Iceland Basin contains a higher energy level by about one order of magnitude, as was already seen in the EKE map (figure 3.11). Additionally, the cyclones are more energetic (by a factor of about 4) particularly at high frequencies (beyond  $0.1 \text{ d}^{-1}$ ) than the remaining data in both basins. In the Iceland Basin, the high energy levels of the cyclones and their abundance suggest that these features play a significant role in the water mass transformation processes of the area. The outstanding energy levels of the cyclones at short time scales add to the remarkable difference between the subpolar and subtropical gyres as pointed out in the previous paragraphs, in particular as they seem to be more abundant in the former when compared to the total amount of data. A similar conclusion was drawn by BOEBEL ET AL. (2003), emphasizing the role of cyclones in mixing versus the well-known anticyclonic Agulhas rings off South Africa.

## 3.4 Methodology

### 3.4.1 Data Availability and Processing

The RAFOS float data from the SFB 460 A3 campaign can be browsed through in the internet data report (LANKHORST ET AL., 2004). Eurofloat data is made available through the WOCE float data center at <http://wfdac.whoi.edu>.

SFB 460 and Eurofloat data were processed using the software package ARTOA, introduced by MENZEL (1995) and improved recently by O. Boebel et al. (pers. comm., 2002). Position data was obtained once per day, but the trajectory data were filtered with a low-

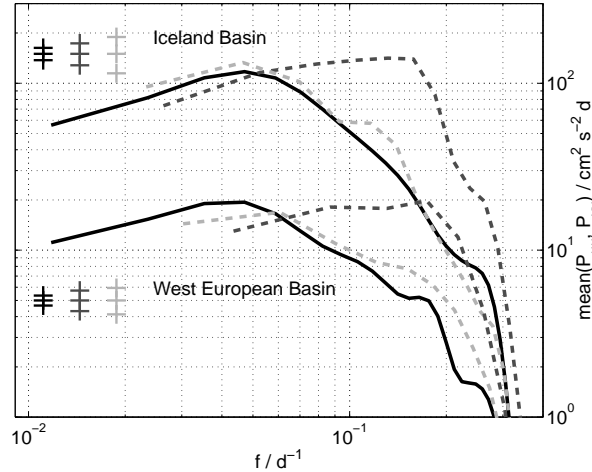


Figure 3.16: Lagrangian velocity spectrum of trajectories within the Iceland Basin (upper bundle of graphs) and West European Basin (lower graphs). The graphs show spectra of the entire data sets (solid, black) and of only the eddy segments (dashed, anticyclones light and cyclones dark grey). In both basins, the cyclones carry significantly more energy at short periods ( $<10$  d) when compared to the anticyclones or the total mean. Additionally, motions in the Iceland Basin are more energetic than in the West European Basin by almost an order of magnitude. Error bars indicate 95% confidence limits. A low-pass filter with a cut-off period of 3 d was applied to the trajectories, causing the rapid decrease at the right edge. Adapted from LANKHORST AND ZENK (2006, © AMS).

pass Butterworth filter with a cut-off period of 3 d to remove sub-mesoscale noise, e. g. tidal-inertial oscillations and tracking errors. All trajectories were inspected by eye to remove obvious errors (e. g. spikes, positions over shallow obstacles). Where information on clock drifts could not be deduced directly from the raw data, these were adjusted to make the floats come close to their launch and re-surfacing positions.

### 3.4.2 Calculation of the Integral Properties

The integral quantities (energy and time scales) were calculated using the software package DANA (Drifter ANALysis), presented by LANKHORST (2003). Trajectories were split up in overlapping windows of 85 d length. This seems to be a good compromise to be longer than the mesoscale and to not interfere with annual variability, and due to the cycle of the MARVOR floats (interruptions every 90 d), it enables all trajectories to be processed in the same fashion. For these segments, Lagrangian EKE and integral time scales were computed and mapped with an interpolation scheme that follows bathymetry (figure 3.11). The idea of this interpolation scheme is presented by DAVIS (1998) and is based on a *generalized distance* between two points, which is calculated from their geometric distance and the difference in barotropic potential vorticity. Decorrelation scales of 200 km and 0.1 ( $\lambda$  and  $\phi$  of equation 11b in DAVIS, 1998, respectively) were applied here. Taking bathymetry into account during mapping has the advantage that properties from boundary regimes are kept separate from the interior, while keeping decorrelation lengths in the interior large to increase the number of degrees of freedom. Length scales and diffusivities were calculated for each trajectory segment from EKE and time scales, and mapped with the same interpolation scheme (fig.

3.12). The calculation of the quantities was carried out as follows:

Let the horizontal Lagrangian velocity  $\mathbf{u} = (u, v)$  measured by a float be separated into its mean  $\bar{\mathbf{u}}$  and deviations  $\mathbf{u}'$  thereof, as in

$$u = \bar{u} + u' \quad \text{and} \quad v = \bar{v} + v'. \quad (3.1)$$

Then, the eddy kinetic energy is defined as

$$\text{EKE} = \frac{1}{2} \left( \overline{u'^2} + \overline{v'^2} \right) \quad (3.2)$$

and simply computed from the variances  $\overline{u'^2}$  and  $\overline{v'^2}$  of the velocity components. All of the following calculations were carried out for both  $u$  and  $v$  components, although only  $u$  is shown for simplicity. In the figures, means of both components are shown. With the (normalized) autocorrelation of  $u$  at time lag  $\tau$  written as  $R_u(\tau)$ , the Lagrangian integral time scale is defined as:

$$T_{\text{int},u} = \int_0^\infty R_u(\tau) d\tau \quad (3.3)$$

It is a measure of the time it takes until the velocity of a float is not correlated with itself anymore. Here, the integration was carried out only up to the first zero-crossing of  $R_u(\tau)$ . Different calculation techniques are discussed by LUMPKIN ET AL. (2002).

The Lagrangian length scale  $L_u$  is a measure of the distance a float travels during the time  $T_{\text{int},u}$ , that is, a typical spatial decorrelation scale or eddy size:

$$L_u = \sqrt{\overline{u'^2}} T_{\text{int},u} \quad (3.4)$$

Horizontal diffusivity is estimated by

$$D_u = \overline{u'^2} T_{\text{int},u} \quad (3.5)$$

provided that one is looking at motions on time scales significantly longer than  $T_{\text{int},u}$  itself (*random walk regime* as opposed to *initial dispersion*, cf. TAYLOR, 1921). As mentioned in the previous text, this is only true if the eddy field is reasonably homogeneous and isotropic.

### 3.5 Concluding Remarks

In this chapter, float trajectories from depths between 1500 and 2600 dbar in the entire northeastern Atlantic between Iceland and the Azores are analyzed. The flow regimes of both the subpolar and subtropical gyres are clearly controlled at depth by local bottom topography. In the north, two driving water masses (Labrador Sea and Iceland Scotland Overflow Waters, LSW and ISOW) are involved in the cyclonic circulation spanning the entire Iceland Basin. The southern parts are best described by a deep western boundary current along the Mid-Atlantic Ridge, and a region of sluggish motion in the inner West European Basin where Mediterranean and Labrador Sea Waters compete.

Nine different subregions of the eastern basins with individually different kinematic characteristics are identified, following the pathways of LSW and ISOW through the eastern basins. Areas of strong and highly stable mean currents are found to stand side by side with

regimes of intense variability or of generally slow motions. The role of Charlie-Gibbs and Bight Fracture Zones (CGFZ, BFZ) as exchange regions for water between the eastern and western basins across the Mid-Atlantic Ridge (BOWER ET AL., 2002) could be confirmed by selected float trajectories. Two pathways of ISOW suggested by HANSEN AND ØSTERHUS (2000, through BFZ and south of Rockall Plateau) could be directly observed and extended. Statistical properties of the mesoscale field coincide with observations by LUMPKIN ET AL. (2002). Significant improvements are made by adding the large SFB 460 data set from the subpolar area. In the Iceland Basin, areas of intense mixing and high-frequency motions ( $EKE \approx O(100 \text{ cm}^2 \text{ s}^{-2})$ ,  $T_{\text{int}} \leq 3 \text{ d}$ ) are found, which contrast sharply with values from the subtropics ( $EKE \approx O(10 \text{ cm}^2 \text{ s}^{-2})$ ,  $T_{\text{int}} \approx 8 \text{ d}$ ).

The automatic identification scheme for eddies in the trajectories (cf. chapter 4) was applied, the findings of which emphasize the role of cyclonic eddies as carriers of high energy at short time scales, and therefore possibly as major mixing agents.

As an outlook, one may expect the Argo array of floats to report sufficient amounts of data to monitor mean currents and hydrographic variability, with the exception that these instruments do not resolve mesoscale motions due to their reduced temporal resolution. A topic for future studies could be the strength of the influence of the meandering North Atlantic Current system. Data from the Mid-Atlantic Ridge region suggest that these processes of the upper water column have a significant imprint even at the depths under consideration here, in particular in the more barotropic subpolar area.



## Chapter 4

# A Self-Contained Identification Scheme for Eddies in Drifter and Float Trajectories

It is becoming increasingly recognized that the eddy field plays an important—possibly dominating—role for oceanic motions in many aspects, e. g. transport of fluid properties. This motivates the study of individual eddy events. In the Lagrangian coordinate system, vorticity possibly associated with eddies appears in two forms: as shear vorticity between neighboring particles, and as curvature of the trajectory of a single particle. Typical field experiments in physical oceanography using surface drifters or subsurface floats do not reach data densities high enough to produce enough encounters of drifters to calculate shear vorticity between them. However, curvature in individual tracks is easily observed. This study presents a methodology that extracts segments from within a trajectory that are “looping”, which will be interpreted as a drifter being caught in an eddy. The method makes use of autoregressive processes, a simple type of stochastic processes, which easily enable a fit to the non-perfectly shaped trajectory data one has to expect from field experiments. These processes also deliver frequency and persistence of the detected eddies by a very simple calculation, which makes the methodology highly suited for automatized scanning of larger data sets.

This chapter reproduces the following manuscript: LANKHORST (2006, © American Meteorological Society (AMS), reproduced by general permission to the author).

### 4.1 Introduction

The imprint of eddy vorticity in particle trajectories can be by shear and curvature. With field experiments in mind, data density is typically low and thus insufficient to deduce synoptic shear vorticity. The search for eddies in such trajectories is then restricted to analyzing curvature. With the aim of finding coherent vortices and deducing their internal structure, one would want to identify several revolutions around an eddy center, in contrast to shorter arc-like “curves” (which may well be caused by a coherent eddy nearby). The whole issue of identifying coherent eddy structures in trajectories is then reduced to finding “looping” segments within a trajectory, and the main difficulty is that data from field

experiments is noisy and of irregular shape.

The most natural way to deal with the issue is obviously inspection by eye, which has been applied frequently in oceanographic research (e. g. SHOOSMITH ET AL., 2005; FRATANTONI AND RICHARDSON, 2006). However, this is time-consuming and possibly subject to human error or bias. A different approach is made by BOEBEL ET AL. (2003), who use a computer algorithm to derive curvature from the (smoothed) tracks and count revolutions accordingly. However, they use threshold values for curvature and duration of the eddy event, and allow for equivalently defined exceptions from these. All of these thresholds are likely to depend on the flow characteristics of the region under study. Roughly at the same time, a software package called *DANA (Drifter ANALysis)* was developed by LANKHORST (2003), which contains an eddy detection algorithm based mainly on the fit of a stochastic process (an *autoregressive (AR)* process). This algorithm has now received further upgrades, tuning, and validation using the work by SHOOSMITH ET AL. (2005, from now on referred to as SRBR05), and is the subject of this discussion. Using the AR process has the advantage that the fundamental behavior of the underlying time series (i. e. oscillating or not, including persistence and period time scales) is easily read off from the fit parameters. The goal is to derive a method which is completely self-contained and requires no initial guess for any parameter (like threshold curvatures or initial guesses for time scales), although the method of course uses such thresholds internally. The mathematical (i. e. less tied to physical quantities) character of these thresholds gives rise to the hope that the method is useful for very different flow regimes. In fact, it has produced sensible results during test runs with RAFOS and SOFAR float data from depths between 700 and 2600 m from the North and tropical Atlantic. These test runs covered the relatively wide ranges of Lagrangian integral time scales from approximately 2 to 10 days and eddy kinetic energies between 1 and 150 cm<sup>2</sup> s<sup>-2</sup>, as shown elsewhere in this work.

## 4.2 Methodology

In this section, the methodology to detect looping parts within a trajectory (called “loopers”) is described. Because of their fundamental importance to the method, autoregressive processes are introduced first. This is followed by a listing of all criteria that need to be fulfilled before a trajectory segment is considered to be looping. A comparison with the study by SRBR05, who identified eddies in float trajectories by visual inspection, finishes the section.

### 4.2.1 About Autoregressive Processes

Autoregressive processes are a class of linear stochastic processes. An *autoregressive process of order n (ARn process)* is one that describes a process variable  $z_t$  by an equation like:

$$z_t = \phi_1 z_{t-1} + \phi_2 z_{t-2} + \dots + \phi_n z_{t-n} + \epsilon_t \quad (4.1)$$

The  $\phi_{\dots}$  are constant coefficients,  $t$  is the time (in discrete, equally separated steps), and  $\epsilon_t$  is a random noise process as a forcing. We are therefore looking at *time series* of a variable  $z_t$ . The name *autoregressive* comes from the fact that  $z_t$  is expressed in terms of itself at previous times. For interested readers, a very detailed discussion of time series analysis is

given by BOX ET AL. (1994). The following paragraphs try to summarize the aspects of AR processes that are important to the use presented here.

An AR process is *stationary* (i. e. all statistical moments are constant with time) exactly if all (possibly complex) solutions  $L$  of the *characteristic equation*

$$1 - \phi_1 L - \phi_2 L^2 - \dots - \phi_n L^n = 0 \quad (4.2)$$

are outside of the unit circle. This shall be assumed true from now on.

The normalized autocorrelation function  $R_z(\tau)$  (where  $\tau$  is the time lag) satisfies the associated homogeneous equation (cf. eq. 4.1 without the forcing term):

$$R_z(\tau) = \phi_1 R_z(\tau - 1) + \phi_2 R_z(\tau - 2) + \dots + \phi_n R_z(\tau - n) \quad (4.3)$$

The power spectral density  $p_z$  as a function of frequency  $f$  is then given by:

$$p_z(f) = \frac{2\overline{\epsilon^2}}{|1 - \phi_1 e^{-2\pi i f} - \phi_2 e^{-4\pi i f} - \dots - \phi_n e^{-2\pi i n f}|^2} \quad \text{with } 0 \leq f \leq \frac{1}{2} \quad (4.4)$$

Note that the shape of both the autocorrelation and spectrum is independent of the forcing term  $\epsilon_t$ , which can only influence the overall level as a constant factor.

Equations 4.1 and 4.3 can also be rewritten as linear difference equations of order  $n$ , after introducing some  $\Delta_z$  and  $\Delta_t$  terms. This emphasizes the close relationship to linear differential equations, which the reader may be more familiar with. The linearity (i. e. additivity and homogeneity of the solutions) is valid for both the difference and the differential versions, which is the underlying reason why these processes are called linear.

It is therefore not surprising that an AR2 process resembles a harmonic oscillator with stochastic forcing  $\epsilon_t$ . Depending on the coefficients  $\phi_{1,2}$ , the solutions to the homogeneous equation 4.3 can be damped exponentials only (overdamped oscillator), exponentially damped sinusoidals (underdamped oscillator), or the aperiodic, degenerated solution inbetween (critically damped oscillator). In terms of the characteristic polynomial (eq. 4.2), this means two real roots, two complex conjugates, or a degeneration into one root, respectively. The latter is defined by the parabola

$$\phi_1^2 + 4\phi_2 = 0 \quad (4.5)$$

for an AR2 process.

Let us now restrict ourselves to stationary, oscillating (i. e. underdamped) AR2 processes. Their coefficients are “below” the parabola of eq. 4.5, and their autocorrelation is described by

$$R_z(\tau) = e^{-d\tau} \cos(2\pi f_0 \tau) \quad (4.6)$$

with

$$d = -\ln(\sqrt{-\phi_2}) \quad \text{and} \quad f_0 = \frac{1}{2\pi} \arccos\left(\frac{\phi_1}{2\sqrt{-\phi_2}}\right) \quad (4.7)$$

The two coefficients  $\phi_{1,2}$  can be transformed into two time scales: a damping time scale  $d$  and an oscillation frequency  $f_0$ .  $d$  is the decay scale of the enveloping exponential and a measure of how long an oscillating motion may be expected to exist coherently. Note that  $d$  is real, because  $\phi_2 < -\frac{1}{4}\phi_1^2 \leq 0$ . Figure 4.1 shows two examples of AR2 processes with

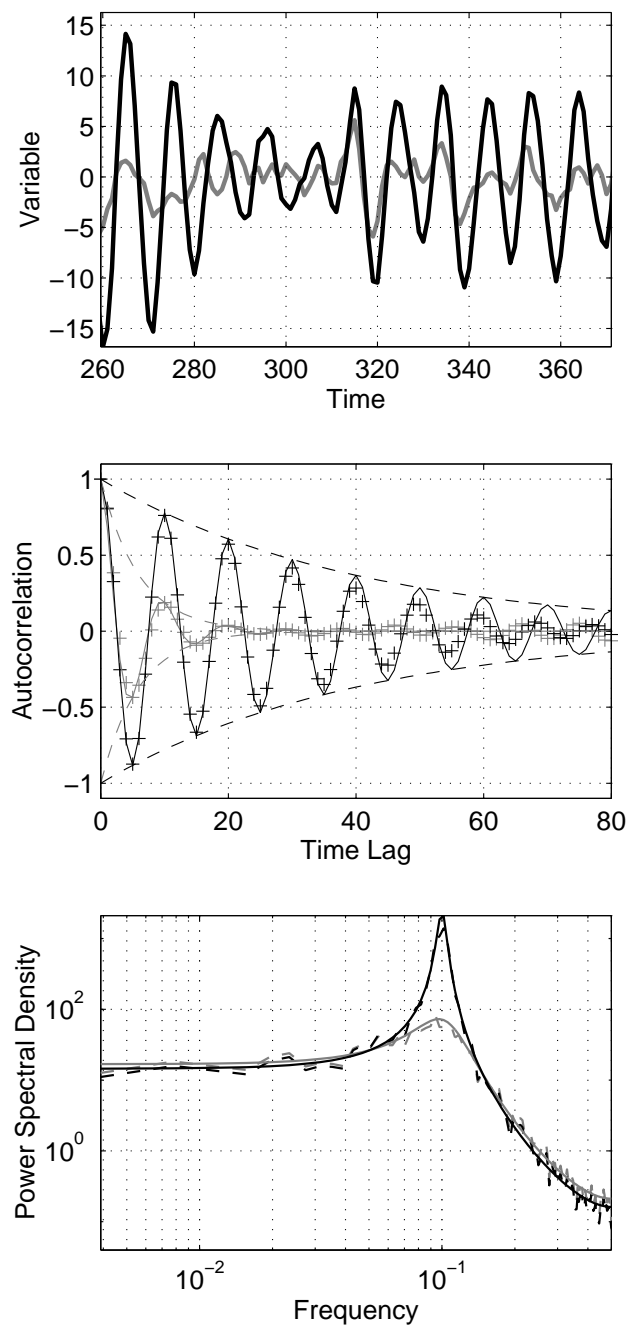


Figure 4.1: Example of two artificially generated time series of AR2 processes. Forcing and fundamental frequency ( $f_0 = \frac{1}{10}$ ) were identical for both, but decay time varied (grey:  $d = \frac{1}{6}$ , black:  $d = \frac{1}{40}$ ). *Top*: Close-up view of the time series. *Middle*: Sample (crosses) and theoretical (solid lines, from eq. 4.3) autocorrelation functions (dashed: enveloping exponentials from eq. 4.3). *Bottom*: Sample (dashed) and theoretical (solid, from eq. 4.4) spectra. Adapted from LANKHORST (2006, © AMS).

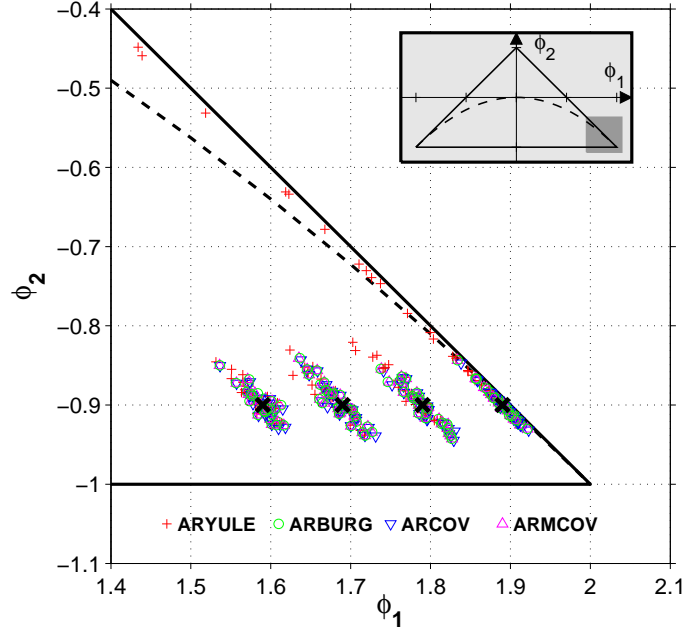


Figure 4.2: Ad-hoc test of AR fitting routines. Time series with known AR2 coefficients (black diagonal crosses) were created, and four fit routines were challenged to recreate these coefficients (different grey symbols). The *aryule* algorithm produced the worst results, while the results from the other three routines were almost identical. The *arburg* algorithm was chosen for the eddy detection process. Black solid lines indicate the triangle in which AR2 processes are stationary, and the dashed line is the parabola that separates periodic (below the parabola) from aperiodic (above it) solutions. The inset in the upper right-hand corner shows an overview of the entire stationarity triangle. See text for further details. Adapted from LANKHORST (2006, © AMS).

identical  $f_0$  but different  $d$ . Both time series oscillate at frequencies near  $f_0$ , but the one with weaker damping does so in a clearer and more energetic way. This behavior is also apparent in the autocorrelation and spectrum (shown in figure 4.1, too).

Stationary AR2 processes are those with coefficients within a triangle in  $\phi_1$ - $\phi_2$ -space, the corners of which are  $(-2, -1)$ ,  $(2, -1)$ , and  $(0, 1)$ . This triangle and the parabola (eq. 4.5) are indicated in the inset in figure 4.2. The remaining figure discusses numerous algorithms to fit an AR process to a given time series, i. e. to find the coefficients  $\phi_{\dots}$  and the strength of the forcing,  $\overline{\epsilon^2}$ , that best match the original time series. The Signal Processing Toolbox (MatLab, from now on SigProcTbx) software contains four such algorithms (called *aryule*, *arburg*, *arcov*, *armcov*), of which the first two use fairly common techniques (the *Yule-Walker equations* and *Burg's algorithm*, see BOX ET AL., 1994; PRESS ET AL., 1993, resp.). The performance of these algorithms was tested by challenging them with artificial AR2 time series with known coefficients. The coefficients were chosen to be in a range that would be expected from oceanic float data: both  $d$  and  $f_0$  are assumed to be small, which leads to coefficients in the lower right-hand corner of the “stationarity triangle”. It turned out that the simple *aryule* method performs worse than the other three routines (between the results of which there was almost no difference), so that *arburg* was selected for the eddy detection process. It is interesting to note that all fitting routines seem to reproduce the frequency

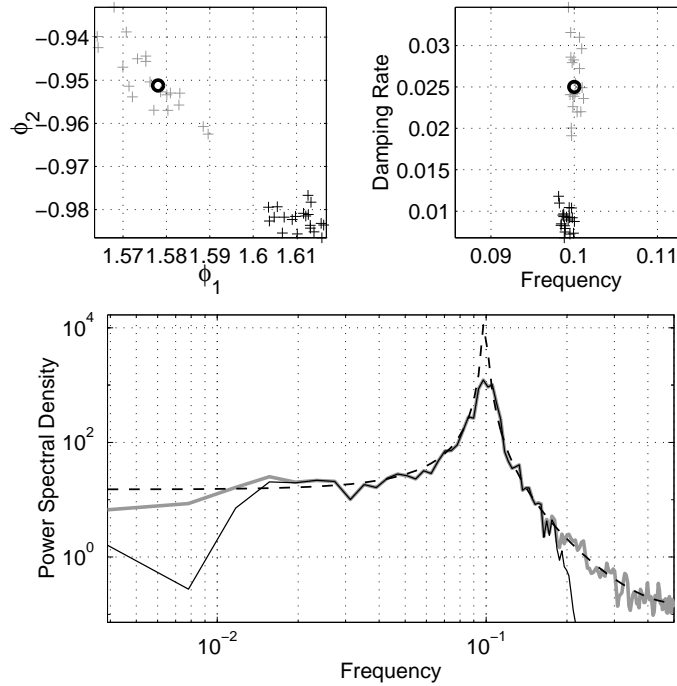


Figure 4.3: Test of AR2 fits applied to filtered time series. Time series with known AR2 (black circles in the upper panels) parameters were created, and a fit routine applied to reconstruct them (grey crosses). Then, a high-order bandpass filter was applied to the original time series, and the AR2 fit routine was applied again (black crosses). The fundamental frequency was still found with very good accuracy (upper right panel), while the damping scale was reduced due to the fact that the filter reduced some of the noise. For one realisation, spectra are shown (bottom panel, grey solid: sample spectrum of the original time series, black solid: sample spectrum of the filtered time series, black dashed: theoretical spectrum from eq. 4.4 using the coefficients from the fit to the filtered time series). The overall impression is that filtering does not affect analysis of the fundamental frequency, and that the AR2 fit works mainly on the parts of the spectrum that carry energy, thereby ignoring the steep cut-off implied by the filter. This behavior is wanted for the eddy detection process. Adapted from LANKHORST (2006, © AMS).

better than the damping scale. This can be seen from the clouds of scattered points around the true values, which are aligned parallel to the parabola of eq. 4.5 (lines of equal  $f_0$  are also roughly parallel to this parabola).

For the eddy detection process, it was necessary to apply a smoothing filter to the data prior to the AR2 fit, to ensure that the fit detects the desired signal. Repeated failures to do so were often related to high-frequency “noise” in the raw data (e. g. poor positioning or unresolved tidal-inertial oscillations), or simply two superimposed eddy-like features (a small, high-frequency eddy orbiting a large, low-frequency object). In almost every case, a simple low-pass filter was sufficient to suppress the unwanted signal, and has therefore been applied as a standard method. However, this carries an inconsistency with it: the spectrum of an AR2 process has a distinct shape (one spectral line with a decay proportional to  $f^{-2}$  at the high-frequency end) which is possibly very different from that of the filtered time series. As an ad-hoc validation of the procedure, an AR2 fit was applied to artificial time series

with known AR2 parameters. Then, a filter was applied to the original time series, and the fit routine was applied again. The results of this test are shown in figure 4.3: in all cases, the fundamental frequency of the AR2 process was found with great accuracy. The damping scale is reduced because filtering removes some of the noise. Nevertheless, the spectrum calculated from equation 4.4 using the coefficients from the fit to the filtered time series resembles that of the original time series (emphasizing the spectral line at  $f_0$  due to reduced noise), which generates exactly the behavior wanted for the eddy detection procedure. To create figure 4.3, a high-order Butterworth filter with a bandpass between  $\frac{1}{4}$  and 4 times the fundamental frequency of the AR2 time series was used. For the eddy detection (cf. next section), a much weaker filter will be applied, so that this may be considered safe.

### 4.2.2 Eddy Detection Criteria

The actual search for looping parts within a trajectory works as follows and is included in the DANA software by the author:

1. The position data of the trajectory is smoothed with a digital filter. As a careful default, a third-order Butterworth low-pass filter with a cut-off period of  $\frac{1}{20}$  of the window length (cf. next list item) is applied. The MatLab, SigProcTbx routines to create and apply the filter are *butter* and *filtfilt*. From the smoothed trajectory, zonal ( $u$ ) and meridional ( $v$ ) velocities are computed by simple differences.
2. The trajectory is split into overlapping windows. As a default for the window length, four passes with lengths of 2, 4, 8, and 16 times the Lagrangian integral time scale  $T_i$  are suggested.  $T_i$  should be computed as an average over all trajectories first. It is advisable that this quantity be reasonably homogeneous throughout the data set one wishes to study. Note that this step automatically adapts the algorithm to the particularities of the flow field, thereby eliminating the need for human input.
3. For each of these windows, means and trends of  $u$  and  $v$  are removed, and AR2 processes are fit to both  $u$  and  $v$  using the *arburg* algorithm (see previous section). This returns coefficients  $\phi_{...}$ , from which damping scales  $d_{u,v}$  and frequencies  $f_{u,v}$  are derived by eq. 4.7. Additionally, auto- and cross-correlations of  $u$  and  $v$  are computed for all windows, and the revolution angle of the trajectory is found by applying MatLab functions *unwrap* and *angle* to  $u + iv$ .
4. The trajectory segment will be considered looping if all of the following criteria apply:

**Oscillating:** The fit shows oscillations, i. e. both  $f_{u,v}$  are real.

**Equal persistence:**  $d_u$  and  $d_v$  are (almost) equal. This has been expressed as follows:

$$\left| \log_2 \left( \frac{d_u}{d_v} \right) \right| < 1.02 \quad (4.8)$$

Together with the next criterium, this ensures that the fits in  $u$  and  $v$  directions have the same characteristics, which is likely for coherent vortices but unlikely for random noise.

**Equal frequency:** Equivalently,  $f_u$  and  $f_v$  are (almost) equal:

$$\left| \log_2 \left( \frac{f_u}{f_v} \right) \right| < 0.15 \quad (4.9)$$

**Duration long vs. period:** The duration time scale is long compared to the detected period for both  $u$  and  $v$  components:

$$\frac{d_u}{f_u} < 0.9 \quad \text{and} \quad \frac{d_v}{f_v} < 0.9 \quad (4.10)$$

**Quality of the AR2 fit:** The AR2 process explains most of the actual variance, i. e. the noise level  $\overline{\epsilon^2}$  that the AR2 fit returns is below the sample variances  $\overline{u^2}$ ,  $\overline{v^2}$  times a scaling factor:

$$\frac{\overline{\epsilon_u^2}}{\overline{u^2}} < 0.59 \quad \text{and} \quad \frac{\overline{\epsilon_v^2}}{\overline{v^2}} < 0.59 \quad (4.11)$$

**Minimum revolution angle:** The revolution angle  $\theta$  is at least two complete revolutions:

$$\frac{1}{|\theta|} < \frac{1}{4\pi} \quad (4.12)$$

**Phase lag 90°:** The phase lag between  $u$  and  $v$  is near 90° or 270°, to extract near-circular motions. This is expressed by the cross-correlation  $R_{uv}$  between  $u$  and  $v$ , which must be near 0 for lag 0:

$$\frac{|R_{uv}(0)|}{\max(|R_{uv}|)} < 0.36 \quad (4.13)$$

The eddy period is then taken from  $f_{u,v}$ , and the sense of rotation from the sign of  $\theta$ . With geostrophic motions in mind, counterclockwise loops will be considered cyclonic eddies in the northern hemisphere and clockwise loops anticyclonic, and vice versa for the southern hemisphere. If a loop crosses the equator, this obviously fails, and the DANA software issues a warning.

The numeric values on the right-hand sides in the above list are initial threshold values that define the behavior of the fit routine. However, a sensitivity study indicates that the method is relatively inert to poorly chosen parameters (cf. validation of the method in next section). The parameters in equations 4.8, 4.9, 4.10, 4.11, and 4.13 have been found to yield best results in this sensitivity study.

The typical application that the algorithm was developed for is subsurface RAFOS float trajectories at intermediate (e. g. 500–3000 m) depth and position fixes in regular intervals of typically one day. An example of such a trajectory with three eddy features is given in figure 4.4. These demonstrate the difficulties one encounters during the automatic detection: advection, varying periods, and irregular shapes of the eddies. Near the start of this trajectory, there is a cyclonic eddy which translates in a curve towards the northeast, while the float slowly leaves the eddy. Thus, the revolution period from the float track increases from approximately 8 to 20 d before the eddy is left. Later, the float is caught in a large stationary anticyclone, in which the trajectory is of rather irregular, non-circular shape. Periods vary between 30 and 80 d. Towards the end, there is a small cyclone (period circa 6 d) which moves erratically. All three eddy features are detected by the algorithm using the above methodology (with the exception that another time window of 160 d length was applied to include the large anticyclone).



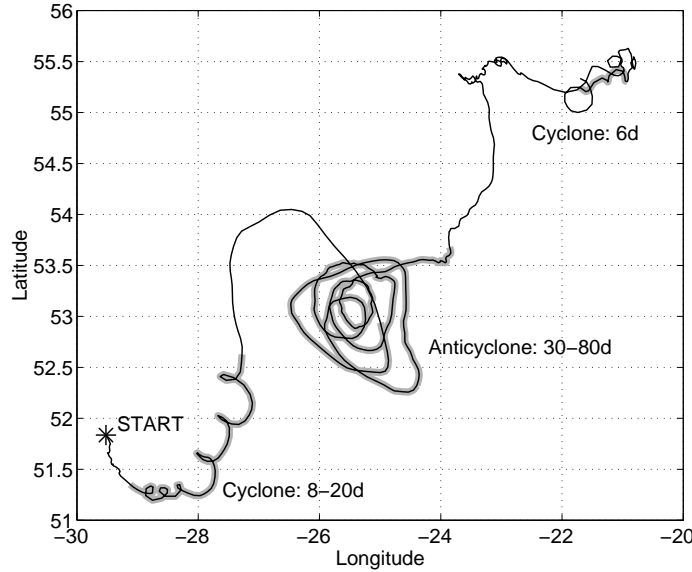


Figure 4.4: Sample trajectory of a RAFOS float at 1500 m depth in the northeastern Atlantic with three eddy features. These demonstrate several difficulties in the detection process: eddy translation (both cyclones), irregular shape (the anticyclone), and varying revolution period as the float changes its distance from the eddy center (all). The shading indicates what the automatized algorithm of this manuscript detected as eddies. To include the large anticyclone, an additional time window of length 160 d was applied in this computation. Adapted from LANKHORST (2006, © AMS).

### 4.2.3 Validation

This section will briefly review the performance of the AR2 fits with respect to the detected periods, which is followed by a comparison of the entire eddy detection algorithm with the work by SRBR05.

For a scientific analysis of the eddy parameters, knowledge of the period is essential. Information on the eddy size is then easily obtained by multiplying the (detrended or, alternatively, RMS) float velocity with the period. As suggested by figures 4.2 and 4.3, the AR2 fit routines are fairly precise when detecting the fundamental frequency. To verify this further, periods of a random selection of eddies from RAFOS float trajectories collected during IFM-GEOMAR projects were estimated visually, and these estimates were compared to the results from the DANA software which uses the algorithm described in the previous section. The results of this comparison are shown in figure 4.5, which verifies a good performance of the algorithm. At long periods, the algorithm tends towards underestimation, which can be explained as follows: the longest window length sets an upper limit to what can be detected. If eddy periods near this length exist, the automatic algorithm will only find those parts that are short enough to fit in, which could be bad frequency estimates, while the better estimates are ruled out by the criterium that two complete revolutions are required. In such a case, the visual inspection will detect the “true” values better. The slope of the linear fit indicated in the figure is approximately 0.81; it increases to 0.97 if only eddies with periods below 25 d are considered, which is highly satisfactory considering the noisiness of the data.

As a thorough validation of the methodology as a whole, a comparison to the results

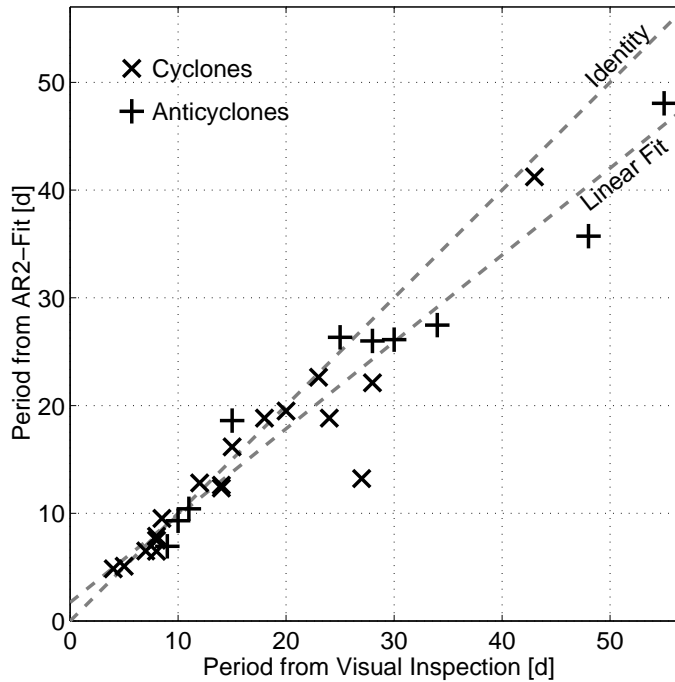


Figure 4.5: Validation of the detected eddy period. A number of float trajectories from different depths (700–1500 m) and regions (subpolar and tropical Atlantic) was inspected visually for eddies. Their periods were estimated and compared to those from the automatic detection scheme using the AR2 fit. As suggested in figure 4.3, the periods are found with great accuracy by the AR2 fit (compare the results to the identity function indicated). Adapted from LANKHORST (2006, © AMS).

by SRBR05 was carried out. There, a data set from the northeastern Atlantic is inspected visually for eddies, which results in a total of 108 loopers, of which 52 are cyclonically looping and 56 anticyclonically looping ( $\frac{52}{56} \approx 0.93$ ). Analyzing the same data set with DANA using the methodology of the previous section, a total of 105 loopers are found, distributed among 62 cyclonic and 43 anticyclonic loopers ( $\frac{62}{43} \approx 1.44$ ).

Of the 108 loopers identified by SRBR05, 60 are recognized by DANA (56%). However, this ratio increases substantially if events with very few revolutions are not considered, because most of the discrepancies between the DANA algorithm and SRBR05 occur with such short-lived events. In fact, if only those loopers with more than 3 completed revolutions (as indicated by SRBR05’s appendices A and B) are considered, DANA identifies 47 of 57 events (83%). Further details on this effect are listed in table 4.1. The explanation for this is that the eddy detection criteria of this manuscript are naturally fulfilled better the longer the looping record is (agreement reaches 97% when considering only loopers with more than 5 revolutions). Furthermore, of the eddies with fewer than 3 revolutions observed, at least 8 do not complete 2  $360^\circ$ -circles and can therefore not be found by DANA, while they are recognized by SRBR05 because two closed loops are completed before reaching a  $720^\circ$  revolution angle<sup>1</sup>. Vice versa, DANA will detect cycloidal cusps as loopers even if they are elongated so that they do not have closed loops, because the data are detrended first. These

<sup>1</sup>Difficult to describe in words. Consider this:

Table 4.1: Dependence of the eddy detection on the number of completed revolutions. The first column indicates how many loopers are found by the reference SRBR05, the second column shows how many of these loopers are also identified by the DANA software. Column 3 contains the ratio of these numbers, and column 4 the number of revolutions completed as indicated in SRBR05 (their app. A and B). Adapted from LANKHORST (2006, © AMS).

Loopers by SRBR05	Loopers common	Ratio	Num. revolutions
108	60	55.6%	all
93	60	64.5%	>2.0
57	47	82.5%	>3.0
45	41	91.1%	>4.0
35	34	97.1%	>5.0

cases are not considered by SRBR05. Several cases are indeed very difficult to decide on, both by eye and by the automatism, and the overall impression is that the agreement is good enough to be limited by the capabilities of both the automatic scheme and the human eye (and not only the former).

To find best agreement between DANA and SRBR05, the parameters of equations 4.8, 4.9, 4.10, 4.11, and 4.13 have been tuned by testing more than 10000 combinations of different values (the other criteria refer to physical properties that are not supposed to be varied). The goal was to find parameters that would maximize the common times spent in loopers in both methods, while yielding equal total looper times in each method. With the above numbers, DANA finds 9073 looper days, of which 5268 (58%) are common with the 9086 found by SRBR05 (figure 4.6). Although the parameters were varied throughout a large domain (by factors of up to 50% for eq. 4.10 and exceeding 300% for all others) in the sensitivity study, this ratio of common looper time to total looper time of either method never fell below 42%, indicating that the method is relatively insensitive to poorly chosen parameters. It should be noted that these numbers include all data, in particular those loopers for which different behavior between DANA and SRBR05 can be explained as in the previous paragraph. Therefore, the agreement of 58% must be considered highly satisfactory.

To demonstrate overall agreement, figures 4.7 and 4.8 show an overview of the results by SRBR05 and the present study. In figure 4.7, all trajectories are shown (“spaghetti diagram”), with the looping parts color-coded according to which of the two methods identified them. The 5268 days commonly identified are shown in green, while the data labeled by none or only one method is in different colors. It is obvious at a glance that DANA identifies features with strong advective motion (wavy lines without closed loops), which SRBR05 do not consider. However, visual inspection revealed that in several such cases there was clearly a pattern that one could consider to be a quickly moving eddy feature. This may be the reason why DANA finds more cyclones than SRBR05, as there seem to be more small cyclones which are rapidly advected when compared to corresponding anticyclones (agrees well with findings by LANKHORST AND ZENK, 2006, chapter 3 here). Figure 4.8 shows that the discrepancy between the cyclone-anticyclone ratios is worst in the western basins, which are known to contain the strong North Atlantic and Irminger Currents possibly advecting the eddies around. It obviously remains beyond the scope of the DANA detection algorithm to differentiate between eddies and other circulation patterns (e. g. wave motions) that may

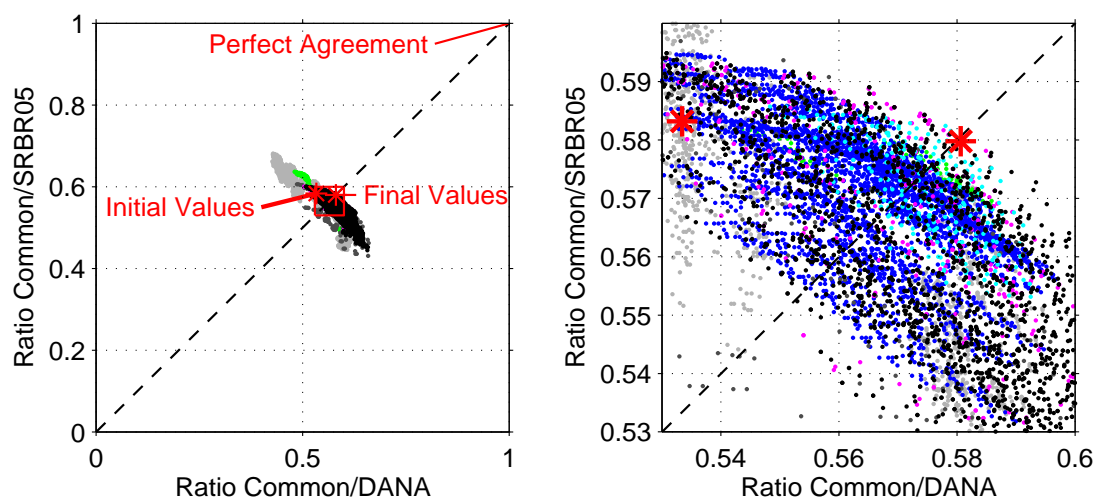


Figure 4.6: Parameter sensitivity study. For more than 10000 combinations of parameters in the eddy detection algorithm, the ratio of eddy time identified by both the algorithm (DANA) and by the reference study (SRBR05) versus that by only one of the methods is shown. Perfect agreement is at (1,1). The goal of the tuning was to be as far up and right on the identity (dashed line) as possible. Although parameters were varied by more than 300%, the cluster of points remains fairly tight in this diagram, indicating that the methodology is inert to poorly chosen parameters. Red symbols show results from initial and final parameters. The right panel is a close-up of the red box in the left panel.

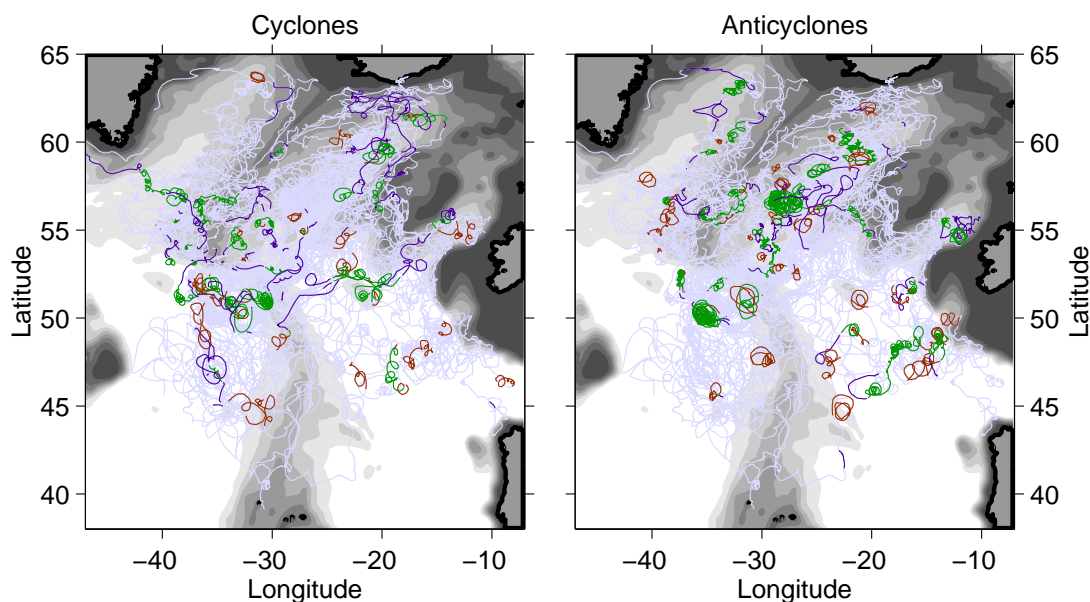


Figure 4.7: Comparison between identified loopers according to the algorithms of SRBR05 and DANA. *Light blue*: No loopers detected by either method. *Dark blue*: Loopers detected by DANA only. *Red*: Loopers detected by SRBR05 only. *Green*: Loopers detected by both methods. Adapted from LANKHORST (2006, © AMS).

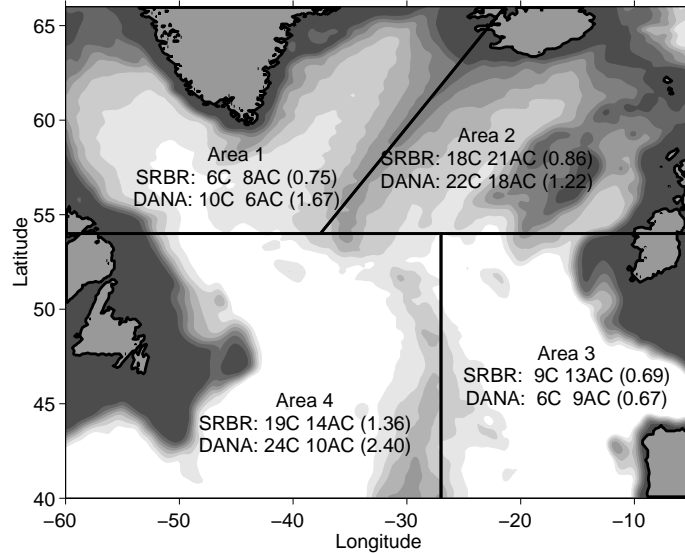


Figure 4.8: Comparison of “looper” detection by SRBR05 (data is from their table 1 and their figure 4) and by the DANA algorithm within a RAFOS float data set at mid-depth in the North Atlantic. In four areas, cyclonically and anticyclonically looping trajectory segments are counted (C and AC, resp.). The numbers in brackets are quotients of these. Adapted from LANKHORST (2006, © AMS).

both create the same cycloidal Lagrangian drift tracks. There are also many cases where the record lengths of the loopers identified by DANA do not match those by SRBR05, which is natural but decreases the percentage of agreement significantly. Otherwise, agreement between the two methods is as described in the previous paragraphs and is expected to satisfy scientific needs.

### 4.3 Concluding Remarks

A self-contained identification scheme for looping segments within float or drifter trajectories is presented. The underlying scientific question is the analysis of coherent eddies, which will result in such loops if a drifter or float is caught in an eddy for a sufficient time. The detection algorithm splits each trajectory up into overlapping time windows, and for every window a set of criteria is applied to decide whether this trajectory segment is considered looping or not. The criteria are based on fundamental statistic properties such as auto- and cross-correlations, and in particular on fits of 2nd-order autoregressive (AR2) processes to the velocity time series. From the AR2 coefficients, it is easily read off whether a time series is oscillating, and periods are derived with good accuracy. Validation has been carried out for the suitability of the AR2 fit routines for this purpose. A comparison to the study by SRBR05, who identified looping trajectories by visual inspection, yielded good agreement to the results found here using the same float data set. As a limitation, the eddy field parameters (i. e. typical eddy periods and sizes) should be reasonably homogeneous throughout the data set under study. The algorithms to formulate the various criteria in computer language are readily available, and a software package called DANA (Drifter ANALysis), first presented by LANKHORST (2003), has the methodology of this study im-

plemented in MatLab code. The advantages of having an automatized computer algorithm for the eddy detection are obviously the aspect of saving time and using objective criteria rather than the human eye. In the study by LANKHORST AND ZENK (2006, chapter 3 here), DANA has been applied to reveal a distinct asymmetry in the abundances of cyclones versus anticyclones in another float data set of the subpolar North Atlantic. It may be interesting to re-analyze other data sets with this question in mind, which is now possible in a rather effective manner.

## Chapter 5

# Zonal Intermediate Currents in the Equatorial Atlantic Ocean

Float data from depths in the Antarctic Intermediate Water (AAIW) are used to investigate the equatorial circulation of the Atlantic Ocean. Bands of zonal flow, alternating in direction approximately every  $2^\circ$  in latitude, are found. Longitudinally, these bands are found to be coherent over virtually the entire study area, i. e. over several thousand kilometers. Analysis of intraseasonal variability shows that the flow directly at the equator has a particularly strong seasonal cycle with a maximum westward velocity in boreal fall. The study of the near-equatorial circulation is motivated by the question how the flow behaves in the absence of the Coriolis force, and especially how the different water masses involved in the Meridional Overturning Circulation (MOC) cross this region. Until recently, numerical models were unable to show the strong zonal currents and their impact on the flow field. These observations hopefully provide a sound baseline for future modelling studies as well as interpretations of other observations. The underlying database and processing methodology is identical to that of chapter 6 and is described in detail in section 6.4.

Results are partly reproduced from the following manuscript, hereafter referred to as OLFRRZ06 (© American Geophysical Union (AGU), reproduced by general permission to the author): OLLITRAULT, LANKHORST, FRATANTONI, RICHARDSON AND ZENK (2006).

### 5.1 Introduction

The equatorial dynamics are different from other parts of the ocean due to the absence of the Coriolis force, which governs much of the dynamics elsewhere, as shown e. g. by the geostrophic computations in the North Atlantic in chapter 2. The question how the waters involved in the MOC actually cross the equator and penetrate through this dynamically different regime has puzzled oceanographers for some time. RICHARDSON AND FRATANTONI (1999) find that deep float trajectories lead from the western boundary current into the interior of the ocean and back on mainly zonal pathways. SCHOTT ET AL. (2003) have assembled mean zonal currents across  $35^\circ$  W from numerous ADCP measurements near the equator, finding strong currents of alternating directions at different depths. Their strongest current over all depths is the Equatorial Undercurrent (EUC), with eastward velocities exceeding  $50 \text{ cm s}^{-1}$  at depths of around 100 m on the equator. At an intermediate depth

of 800 m, they find eastward currents near  $2^\circ$  N/S and westward currents near  $4^\circ$  N/S and at  $0^\circ$ . It is this latitudinally alternating, but longitudinally coherent structure that is referred to as equatorial *jets*, which also extends to other depths not mentioned here. JOCHUM AND MALANOTTE-RIZZOLI (2003) clearly dislike the term *jets* but instead refer to the current structure as a superposition of planetary waves—at wavelengths reportedly exceeding the basin width, it remains somewhat unclear what the difference between such wave-induced circulation and a jet would be, though. Anyhow, they conclude with a clear statement requesting a more profound observational database, arguing that the early results by SCHOTT ET AL. (1998) might be based on sparse data suffering from aliasing in the wave field. In the same volume already, SCHMID ET AL. (2003) report findings from profiling floats drifting at intermediate depth in the area, clearly in agreement with the results by SCHOTT ET AL. (2003). Meanwhile, the amount of float data in the area has increased further, particularly through the French SAMBA (Subantarctic Motion in the Brazil Basin) project and the international Argo array. OLFERZ06 have combined these and multiple other data sets to map out the equatorial zonal currents near 800 m depth with an unprecedented, basin-wide data coverage. The following discussion will review these findings. From the database described in chapter 6.4, only data from the ten-day (or equivalent) displacements of floats are used in this chapter. Float depths between 600 and 1050 dbar are considered to be within the AAIW, with the majority of the data from either near 800 or 1000 dbar.

## 5.2 Results from Float Observations

Figure 5.1 shows averaged zonal and meridional velocities derived from all float observations available in the AAIW depth range. The zonal component has a pronounced tendency to produce zonal bands of alternating flow direction, which is completely absent in the meridional component. In particular, the near-equatorial currents described by SCHOTT ET AL. (2003) are clearly seen and demonstrated to extend across the entire Atlantic: at the equator, the mean flow is westward (Equatorial Intermediate Current, EIC), averaging near  $5 \text{ cm s}^{-1}$ . Towards either side of the EIC, there is eastward flow near  $2^\circ$  latitude (Northern/Southern Intermediate Countercurrent, NICC and SICC), averaging between 5 and  $10 \text{ cm s}^{-1}$ . Further out yet, at  $4^\circ$  latitude, the flow is westward again. OLFERZ06 use the naming convention of Northern/Southern Equatorial Intermediate Currents (NEIC/SEIC) here. Even further south, the zonal bands are clearly obvious, although weaker: eastward bands are found near  $6^\circ$  S and  $10^\circ$  S, while westward flow is at  $8^\circ$  S and  $12^\circ$  S. In the northwestern tropical Atlantic (north of  $5^\circ$  S and west of  $35^\circ$  W), the band structure is slightly bent out of shape, which is particularly obvious for the NICC and the NEIC. These currents are then aligned approximately in the direction WNW–ESE rather than strictly zonal, which makes them follow the coast of South America further north. A likely reason for this bending is interaction with topography and/or the western boundary current. Indeed, RHINES (1975) has described dynamics leading to zonally aligned current bands, and when topography plays a role, these bands become aligned parallel to lines of constant  $f/h$  ( $f$ : Coriolis parameter,  $h$ : water depth).

In both the zonal and the meridional velocity components, the western boundary current is obvious. It is called North Brazil Current (NBC), or North Brazil Undercurrent (NBUC), to differentiate between the flow at the surface (NBC) and at intermediate depths (NBUC, JOHNS ET AL., 1998). From the figure, a northward component is seen all along the coast of South America up to approximately  $8^\circ$  N. Simultaneously, an alongshore component



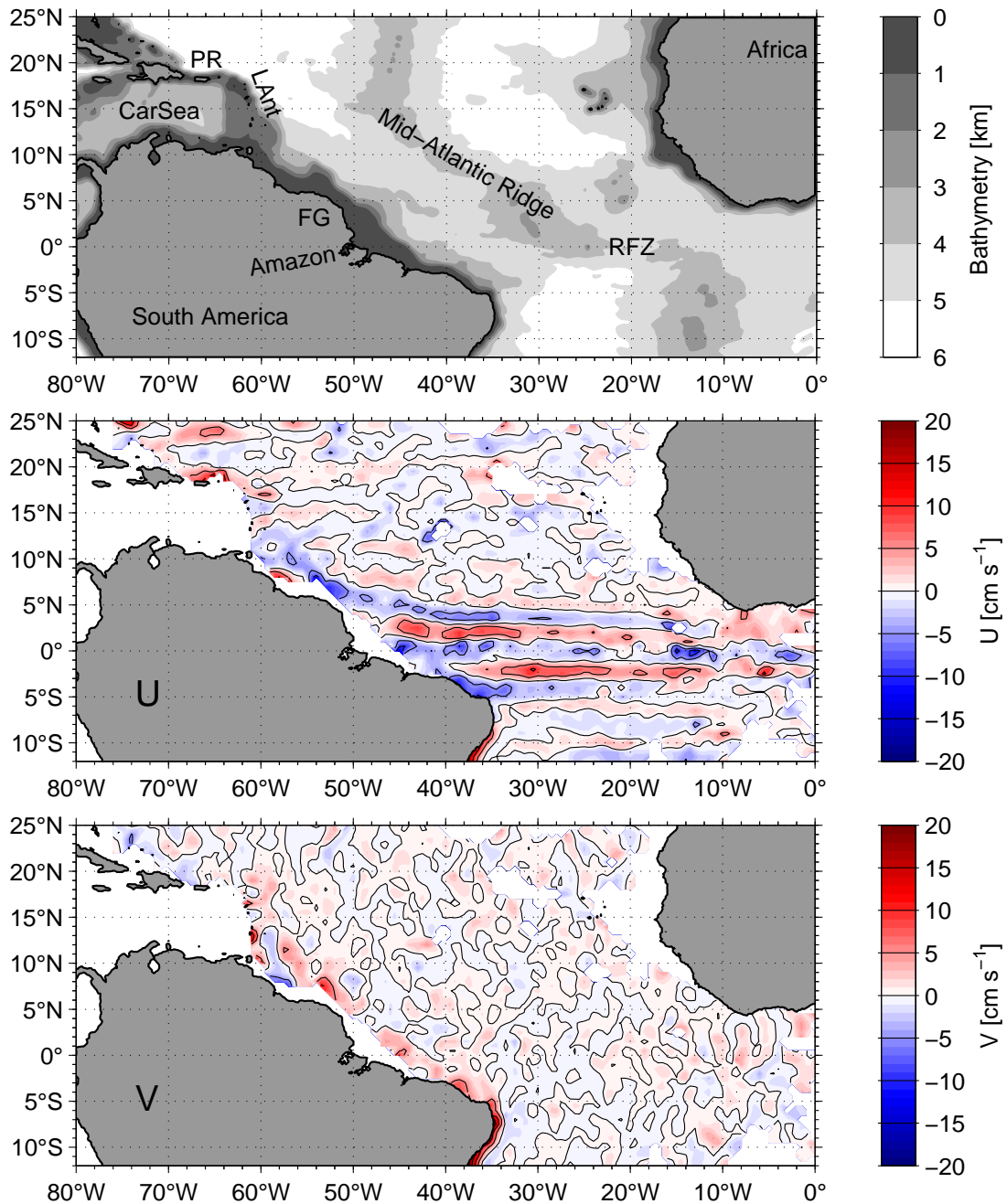


Figure 5.1: *Top*: Geographic overview over the tropical Atlantic. Abbreviations are: CarSea Caribbean Sea, FG French Guiana, LAnt Lesser Antilles, PR Puerto Rico, RFZ Romanche Fracture Zone. *Middle and bottom panels* show mean velocities derived from float observations in the AAIW layer (600–1050 dbar). *Middle*: Zonal velocity component ( $U$ ). *Bottom*: Meridional velocity component ( $V$ ). For  $U$ , zonal bands of alternating flow direction are the strongest features especially near the equator, which are completely absent in the  $V$  component. For  $V$ , the strongest current is the intermediate western boundary current, the North Brazil Undercurrent (NBUC).

is seen in the zonal velocity, which is eastward south of  $7^\circ$  S and westward north of there. Individual trajectories show several cases of interaction between the boundary current and the zonal bands of the interior. Interestingly, localized maxima in northward velocity of the boundary current occur just north of where the westward EIC and NEIC feed into it ( $1^\circ$  N and  $7^\circ$  N). This might indeed be a direct evidence of interaction between the two current regimes. Apart from the zonal current bands and the boundary current, the mean flow is not significantly different from zero. This is particularly obvious in the plot of meridional velocity, which is dominated by noise in the open ocean.

The depth range of 600–1050 dbar chosen for the AAIW here is relatively thick, knowing that there can be strong vertical shear in the equatorial region. This is likely of minor concern at latitudes greater than  $2^\circ$  on either hemisphere, as indicated by the more barotropic nature of the flow there found by SCHOTT ET AL. (2003). However, to avoid combining data from dynamically different depth ranges, OLFZR06 separate the float data into two layers: one around 800 dbar, mainly sampled by floats of the SAMBA project, and one around 1000 dbar, mainly based on Argo. Figure 5.2 shows their plots of the zonal velocity. Indeed, the two layers agree well except at the equator, where data coverage of the lower layer is relatively poor. Outside the area where the upper layer is well-sampled, the Argo floats of the lower one complete the picture, especially with the zonal current bands south of  $5^\circ$  S. A feature that is only seen in data from the 800 m layer is the intensification of the NICC and the EIC above bathymetric obstacles: both have maxima in velocity at pronounced topographic features. For the NICC, maxima at the Mid-Atlantic Ridge (MAR, here  $32^\circ$  W– $24^\circ$  W) and at a seamount near  $38^\circ$  W are seen. The EIC has distinct maxima at  $25^\circ$  W and  $15^\circ$  W, where the promontories of the MAR are situated on either side of Romanche Fracture Zone.

Figure 5.3 shows zonally averaged zonal velocities for both the 800 dbar and the 1000 dbar layers in a box bounded by  $12^\circ$  N/S,  $33^\circ$  W, and  $20^\circ$  W. From the upper layer, the mean velocities of the NEIC, NICC, EIC, SICC, and SEIC are  $-5$ ,  $9$ ,  $-6$ ,  $8$ , and  $-5$   $\text{cm s}^{-1}$ . As mentioned before, agreement between the two layers is good except at the equator. When the data of the deeper layer is taken only from a box entirely west of the MAR, though, the results from the two layers are identical within the confidence limits even there. OLFZR06 then speculate about the causes of the differences, which are particularly pronounced above and east of the MAR, possible reasons being a general shoaling of the jets to the east, interaction with topography, or just poor data coverage.

To investigate temporal variability, the data were sorted by month and then zonally averaged to create figure 5.4, assuming that the monthly averages are independent of the year in which they were sampled. Based on the findings of the previous paragraph, only data from the western basin is used. The result shows the pronounced seasonal cycle of the EIC and—to a lesser degree—the other equatorial currents. Virtually the entire westward signal of the EIC is concentrated in boreal fall (July–November), with another minor westward peak in April and stalling or even eastward currents inbetween. This is in strikingly good agreement with results by SCHOTT ET AL. (2003), who derive a similar cycle from their shipborne ADCP observations from 13 cruises at  $35^\circ$  W. This is especially noteworthy because their seasonal cycle is based solely on fitting annual and semiannual harmonics to the observations, and only three of their observations are actually in boreal fall. With the completely independent float observations here and their statistical significance, a lot of confidence is gained on the issue, which might even reduce the doubts expressed by JOCHUM AND MALANOTTE-RIZZOLI (2003). The NICC and SICC both appear to be present

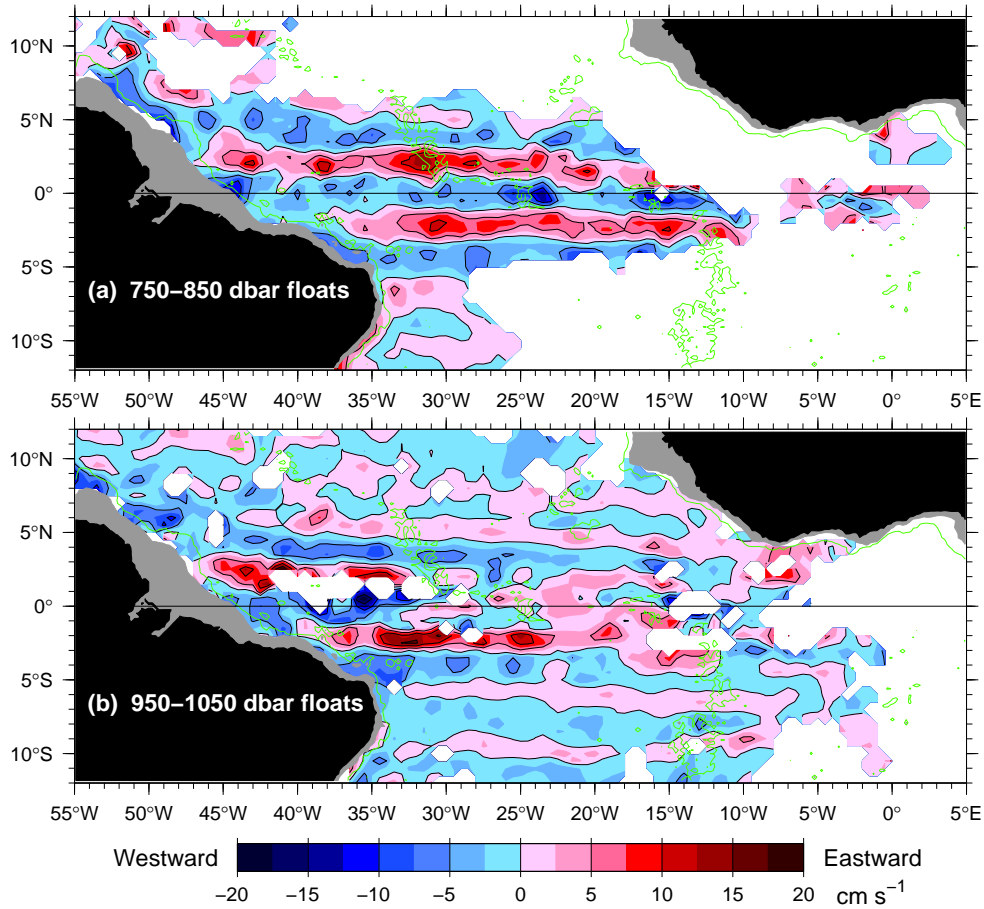


Figure 5.2: Map of mean zonal velocities derived from float observations in the AAIW layer. *Top*: From float displacements between 750 and 850 dbar, mainly sampled by the SAMBA project. *Bottom*: From float displacements between 950 and 1050 dbar, mainly sampled by Argo. Bathymetry is shown at 1000 m (grey) and 3000 m (green). Reproduced from OLFZR06 (© AGU 2006).

throughout the year, although their widths seem to reduce when the bulk of the EIC appears in boreal fall. At the same time, they appear to be pushed away from the equator to their highest latitudes at almost  $3^\circ$  N/S. In boreal winter (January and February), their mean axes are significantly closer to the equator ( $<2^\circ$  N/S), and their eastward current signature is connected across it in the absence of the EIC. The westward NEIC has a broad peak intensity between March and July but is indeed present year-round. Similarly, the SEIC can be seen in the diagram, although with weak data coverage in late summer. With this in mind, it is seen strongest in boreal winter and spring, and stalling in late summer.

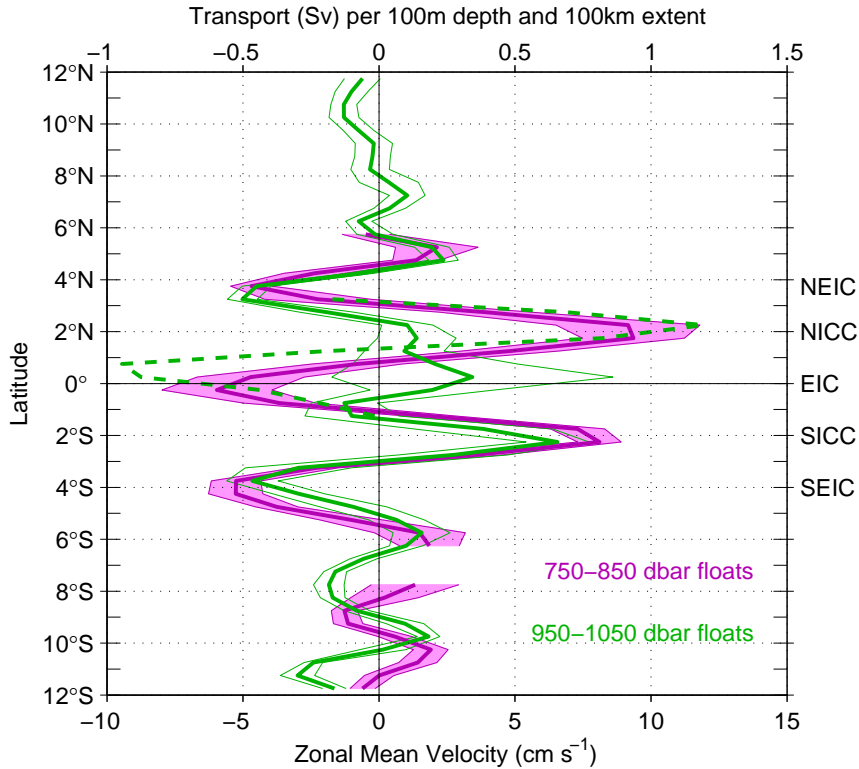


Figure 5.3: Zonally averaged zonal velocities derived from float observations in the AAIW layer (same data as in figure 5.2) for the box between  $33^\circ$  W and  $20^\circ$  W. Data is from 10-day displacements. Confidence limits are based on the variance of the ensemble of displacements and on the number of displacements divided by two. *Purple*: Data from floats near 800 dbar. *Green*: Data from floats near 1000 dbar. *Green dashed*: From 1000 dbar, but from an area completely west of the Mid-Atlantic Ridge. Figure reproduced from OLFZR06 (© AGU 2006).

## 5.3 Concluding Remarks

### 5.3.1 Equatorial Current Bands at Other Depths

While the previous paragraphs have discussed the equatorial currents at the depth of AAIW, zonal bands of zonal currents are clearly visible at other depths, too. In fact, they can be seen from the surface to the deep ocean. At the surface, various branches of the South Equatorial Current and the Equatorial Countercurrent contribute to them, followed by the swift Equatorial Undercurrent and the South Equatorial Undercurrent (SCHOTT ET AL., 2003). Recent float observations are available at these shallower depths, too (FISCHER ET AL., 2007). However, the depth of the AAIW is special in that such an amount of float data has been collected there, enabling the basin-wide mapping of the currents. At greater depths of 1800 m in the uNADW, RICHARDSON AND FRATANTONI (1999) report velocities from SOFAR floats that reveal a pattern very similar to the one seen in the AAIW here, in agreement with the section shown by SCHOTT ET AL. (2003). The pattern reported resembles at least the four bands of the NEIC, NICC, EIC, and SICC as seen in the AAIW (RICHARDSON AND FRATANTONI, 1999, their figures 11 and 12).

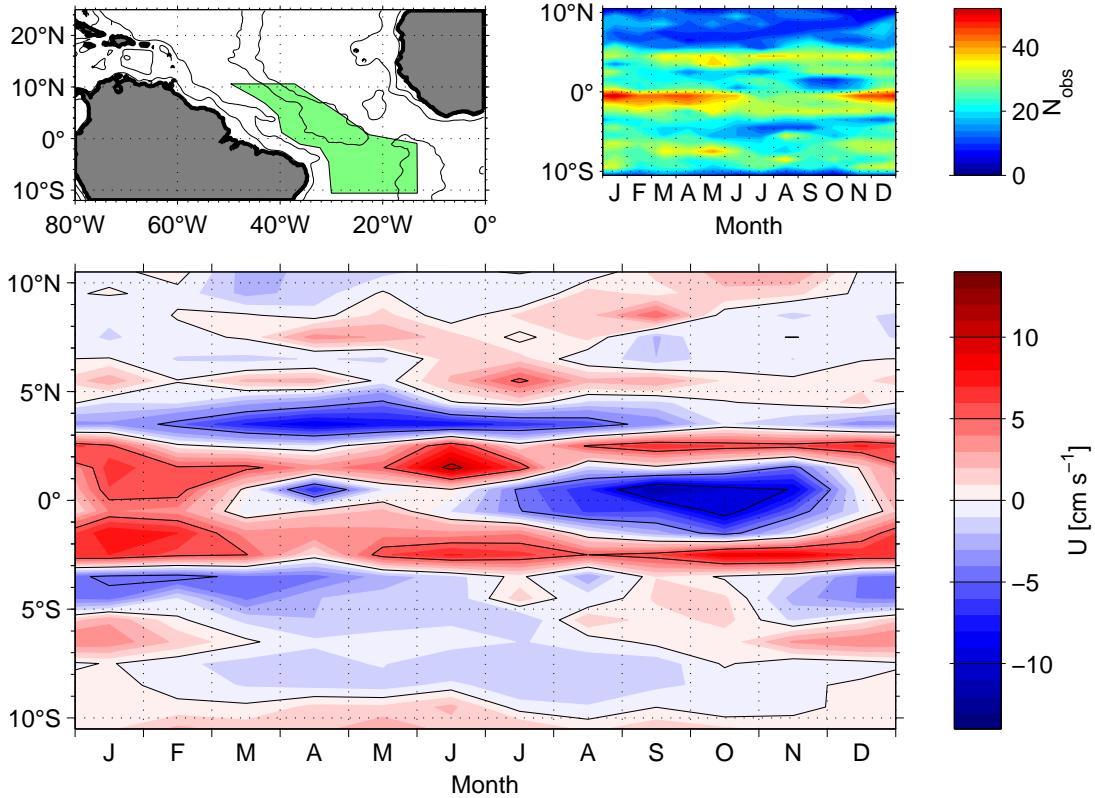


Figure 5.4: Seasonal variability of zonal velocity in a multi-year average. *Top left*: Data is from within the box indicated on the map. Bathymetry is outlined at depths of 1000 and 4000 m. *Top right*: Number of observations. Each observation is a float displacement of approximately 10 d duration. *Bottom*: Zonal velocity as a function of month and latitude (Hovmöller diagram). Data from different years are combined if they were in the same months. The strongest signal is the onset of the EIC in boreal fall. NICC and SICC show a latitudinal displacement around this EIC onset.

### 5.3.2 Notes on Dynamical Aspects

The theory behind the zonal current bands is not yet fully agreed upon (JOCHUM AND MALANOTTE-RIZZOLI, 2003), although there seems to be general agreement that geostrophic turbulence has a tendency to produce zonally elongated patterns. These notions have been presented by RHINES (1975), who outlines a transition from an isotropic eddy field to an anisotropic regime dominated by planetary waves and eventually to the final state of zonal current bands of alternating direction. This evolution occurs as the two-dimensional geostrophic turbulence transports eddy energy towards larger spatial scales, but can obviously be interrupted if eddy activity is damped away too rapidly. Indeed, such damping is a likely reason for the fact that JOCHUM AND MALANOTTE-RIZZOLI (2003) find a flow field dominated by planetary waves but no stable zonal current bands in their model results. RHINES (1975) speculates about the final state of steady zonal alternating flow as having a spatial “scale somewhat larger than, but of the order of  $(2U/\beta)^{\frac{1}{2}}$ ”.  $U$  is a typical velocity scale and  $\beta$  the northward gradient of the Coriolis parameter. With  $U = 10 \text{ cm s}^{-1}$  and  $\beta = 2.3 \cdot 10^{-11} (\text{m s})^{-1}$ , a length scale of 93 km is derived, quite consistent with the

observed spacing between alternating currents of around  $2^\circ$  in latitude (222 km) as shown in figure 5.3. We shall conclude here in the belief that the dynamics leading to alternating zonal current bands are likely circumscribed by RHINES (1975), bearing in mind that the real ocean is subject to topographic constraints, stratification, and temporally varying forcing. More recently, numerical models have begun to show that such zonal bands seem to be an omnipresent feature of the ocean circulation, indicating the progress made in numerical techniques (higher resolution and lower numerical dissipation, RICHARDS ET AL., 2006).

## Chapter 6

# On the Circulation in the Northwestern Tropical Atlantic

Initiated by the float observations of the MOVE (Meridional Overturning Variability Experiment) project east of the Lesser Antilles, this chapter is concerned with the circulation of the northwestern tropical Atlantic. The area of interest is roughly delimited in the southeast by the equatorial current system discussed in the previous chapter, and in the west by the American coast and the Antilles islands. A natural limit to the east is the Mid-Atlantic Ridge (MAR), and to the north, the Tropic of Cancer marks the edge of the region under investigation here. Float data from two depth layers are analyzed: from the AAIW layer (Antarctic Intermediate Water, 600–1050 dbar) and from the uNADW layer (upper North Atlantic Deep Water, 1200–2050 dbar). Floats within the MOVE project were originally launched to ease the interpretation of the mooring data of the same experiment, but have been combined with other datasets here to complete the picture to a basin-wide view. It is found that the boundary currents and the equatorial currents are the only regimes with significant mean velocity. Consequently, the mesoscale eddy field is also investigated with the acoustically tracked floats, reporting on its time, space and energy scales. The database common to this and the previous chapter is described in section 6.4, and the methodology underlying the analysis of the mesoscale follows the notions outlined in section 3.4.

A manuscript based on these findings is in preparation (LANKHORST, FRATANTONI, OLLITRAULT, RICHARDSON, SEND AND ZENK, 2007a).

### 6.1 Mean Currents

For the AAIW depth range, the mean currents are already shown in figure 5.1. In the basin interior, they are insignificantly different from zero except for the prominent equatorial current system. Other areas where sufficiently strong mean flow is observed is in the boundary current off South America (North Brazil Undercurrent, NBUC), and eastward flow at the very northwestern limit of the study region ( $24^{\circ}$  N,  $60$ – $70^{\circ}$  W) and immediately north of Puerto Rico. East of the Lesser Antilles ( $10^{\circ}$  N– $20^{\circ}$  N), there is no clear signature of either equatorial zonal currents or a boundary current, although the plot of zonal velocity continues to show longer zonal coherence of the patterns than meridional

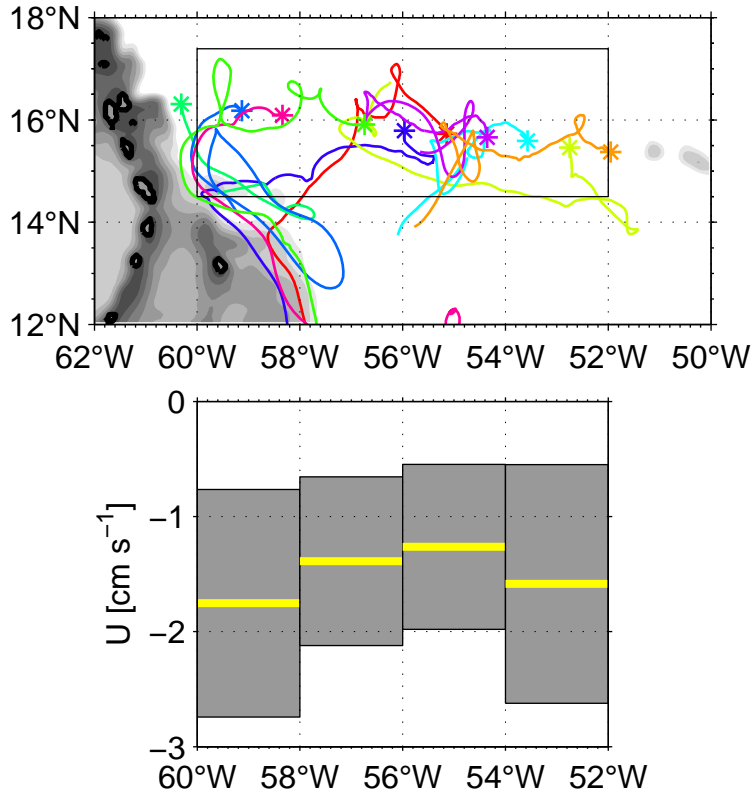


Figure 6.1: Mean zonal velocity for the MOVE floats nominally at 1400 dbar. *Top*: Map; individual trajectories start at the asterisks. Bathymetry as in figure 3.3. Data from within the black box are used in longitudinal bins of  $2^\circ$  extent to compute zonal velocities. *Bottom*: Mean zonal velocities (yellow) in four longitudinal bins and 95% confidence limits (grey) based on a decorrelation time of 8 days. Westward velocities are statistically significant in all bins.

coherence. However, this is at or below the noise level.

For the uNADW depths, data density is not sufficient to produce a similar map, but a general westward motion is clearly seen in the MOVE floats occupying the area east of the Lesser Antilles (figure 6.1). All floats have a tendency to drift westward there, which is statistically significant and might be the return flow of a basin-wide recirculation cell or part of yet another zonal current band. Individual trajectories are entrained into the southward boundary current when approaching the continental slope. A net meridional velocity is not obvious except in the southward Deep Western Boundary Current (DWBC). Other areas of significant mean flow are identified by RICHARDSON AND FRATANTONI (1999) in the DWBC off South America and in the equatorial current bands.

To cross-validate the float observations and to further investigate the structure of the boundary currents, a comparison with mooring data from different sections across the boundary was carried out (figures 6.2, 6.3, and 6.4). For each depth layer (AAIW and uNADW), three imaginary sections are defined. Float displacement data from near those sections (for exact locations, cf. figures and the captions) were averaged into bins of 100 km extent, and across-section velocity derived for these bins. The figures show the binned float data and mooring data.



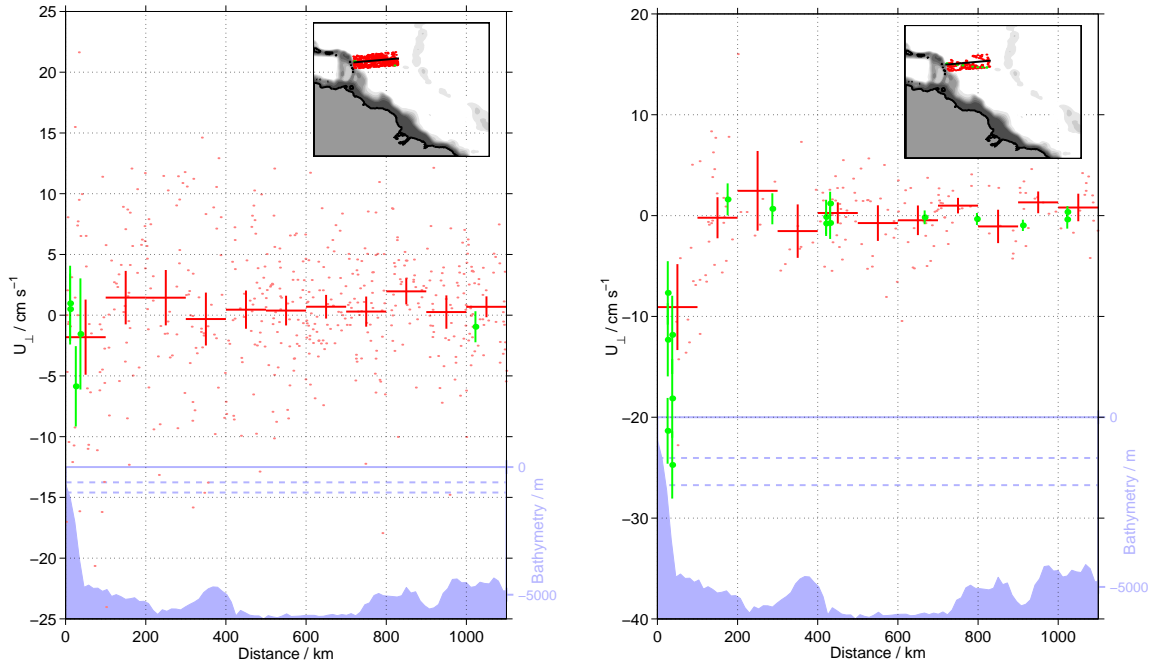


Figure 6.2: Velocity perpendicular to a section east of the Lesser Antilles. *Left:* In the AAIW layer. *Right:* In the uNADW layer. The map insets show where the data is from (red dots: float measurements, green dots: mooring locations), and the targeted section (black lines). Data from within 167 km (equivalent to  $1.5^\circ$ ) to either side of the section was used. The main frames contain all float measurements (light red dots), the float data binned into boxes of 100 km width (red crosses), and mooring data (green symbols). Superimposed in light blue is the bathymetry with the AAIW or uNADW depth ranges (dashed, bathymetry scales at bottom right). Vertical error bars for float and mooring data are 95% confidence limits based on decorrelation times of 10 d. Mooring data is from the MOVE (IFM-GEOMAR) and GAGE (M. McCartney, WHOI, personal communication) experiments. For the AAIW, there is no significant mean flow across the section, whereas the southward boundary current stands out in the uNADW. Multiple green dots are from different mooring deployment periods within MOVE.

For the AAIW layer, no significant velocity is found across the northern section (figure 6.2), consistent with the moorings of the MOVE array. Data at the western boundary close to Guadeloupe may leave room for speculating about a southward mean at the edge of the confidence limits. As a consequence, AAIW as a water mass might actually reach this location through the Caribbean, which it could enter through several passages in the southern Windward Islands and exit through Anegada Passage to the north of the section considered here (D. Fratantoni, personal communication). Indeed, two out of thirteen MOVE floats entered the Caribbean between Martinique and Dominica. In any case, the clear signature of the boundary current carrying AAIW northward, as is seen off the American coast further south, has ceased to exist at this latitude. This boundary current, the NBUC, is the dominant feature of the sections shown in figures 6.3 and 6.4. A comparison with figure 5.1 shows that the sections here are located where the NEIC and the EIC merge with the NBUC. Between the two locations, the signature of the NBUC actually disappears (figure 5.1 near  $48^\circ$  W), at least in this average derived from the float displacements. For the NBUC at the

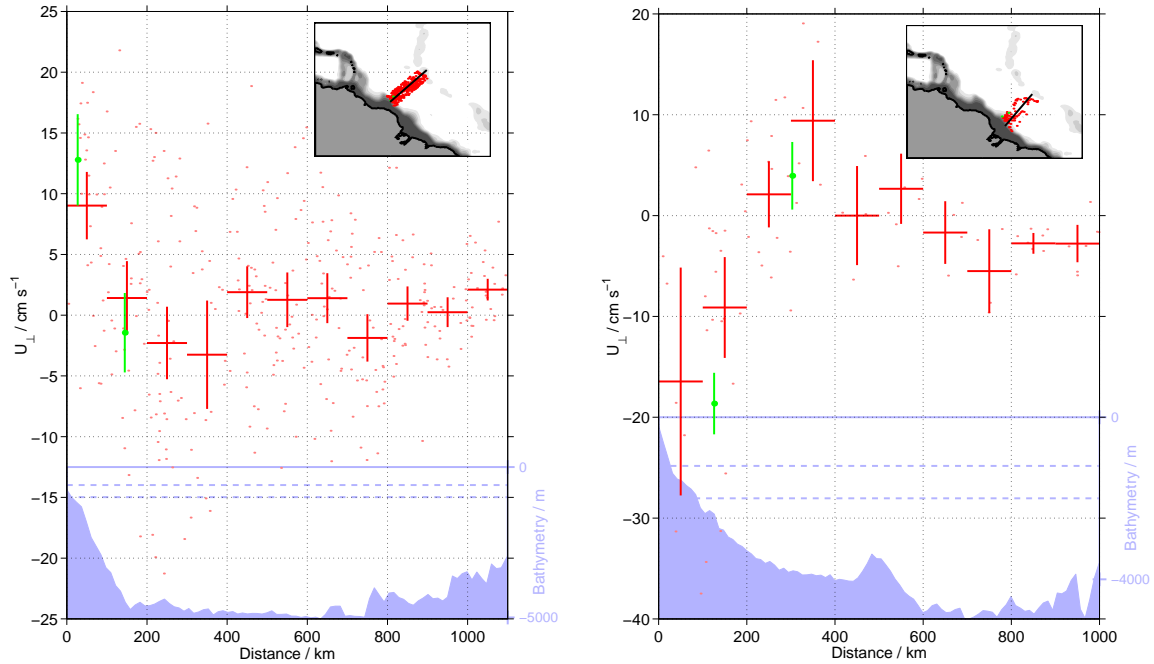


Figure 6.3: Velocity perpendicular to two sections off French Guiana. *Left:* In the AAIW layer. *Right:* In the uNADW layer. Like figure 6.2, but for the uNADW layer, data from within 222 km (equivalent to  $2^\circ$ ) to either side of the section was used due to data sparsity. Mooring data are from JOHNS ET AL. (1990, left) and JOHNS ET AL. (1998, right). In the AAIW, the northwestward NBUC is seen, whereas the boundary current at the uNADW is southeastward.

sections, mean northwestward speeds near  $5\text{--}15\text{ cm s}^{-1}$  are consistently observed both by the floats and by the moorings. The float data elegantly complete the spot measurements by the moorings especially by continuing the measurements into the open ocean. This is particularly useful in figure 6.4, which reaches far into the alternating bands of the equatorial currents discussed in the previous section and again reveals the EIC/NBUC (first 200 km off continental slope), NICC (200–400 km), and the NEIC (400–600 km) in this side-by-side view. SCHOTT ET AL. (1993) actually cast doubt on their southeastward (NICC) mooring records there due to large intraseasonal variability and shortened record length. These float observations clearly show the same pattern as the moorings and put the results within the context of the equatorial zonal currents. Further out yet, alternating flow patterns remain visible but do not exceed the confidence limits.

For the uNADW depth range, all three sections show the DWBC flowing along the coast towards the southeast. Average velocities range from  $10$  to  $30\text{ cm s}^{-1}$  at the core, increasing from north to south. While in the northern section (figure 6.2), no significant flow across the section is observed away from the boundary, there are indications of alternating flow across the other two sections. In particular, the uNADW field in the southernmost section (figure 6.4) shows similarities with that of the AAIW offshore, although the boundary currents are in opposite directions, which repeats the findings by RICHARDSON AND FRATANTONI (1999) mentioned earlier.

The fact that the agreement between the float and mooring observations is remarkably

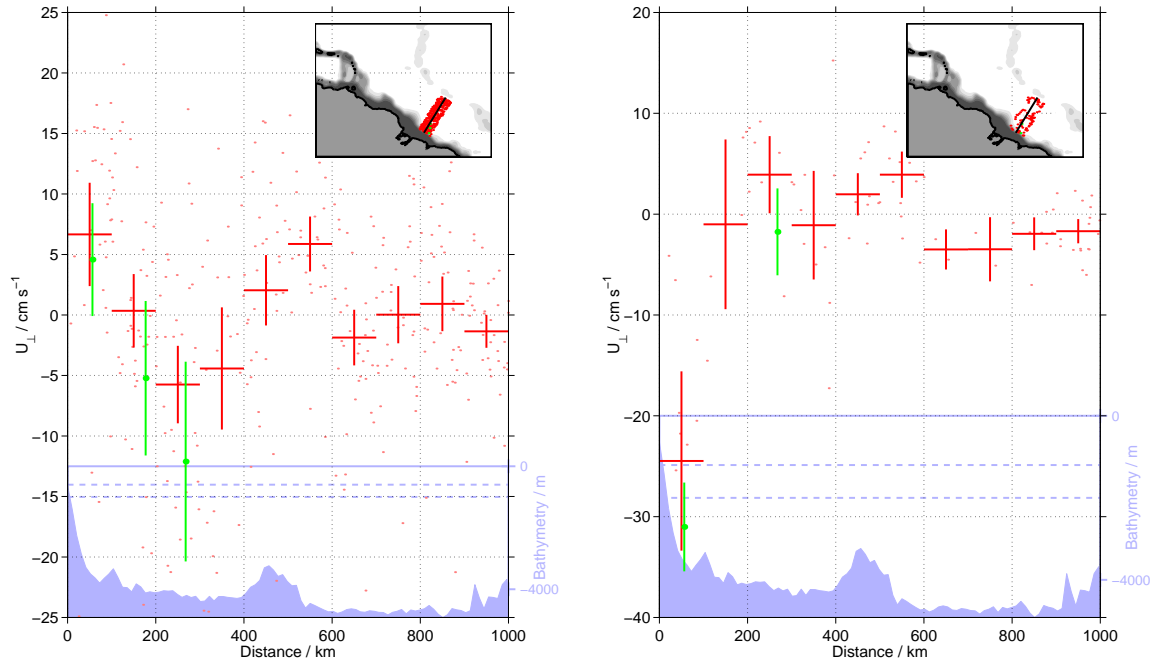


Figure 6.4: Velocity perpendicular to two sections off northern Brasil. *Left*: In the AAIW layer. *Right*: In the uNADW layer. Like figure 6.2, but for the uNADW layer, data from within 222 km (equivalent to  $2^\circ$ ) to either side of the section was used due to data sparsity. Mooring data are from SCHOTT ET AL. (1993). In the AAIW, the northwestward NBUC is seen, whereas the boundary current at the uNADW is southeastward. Offshore bands of alternating flow direction are related to the equatorial current system discussed in chapter 5.

good reduces concerns arising from combining float data from different times and depths (cf. figure 6.9), and is also meant to add further confidence to the results of the discussion of the equatorial current bands in chapter 5.

As seen from figures 6.2 through 6.4, the DWBC is the dominating signal in the uNADW layer. Data from the MOVE project actually allow for a closer look at the boundary current structure there: figure 6.5 shows a snapshot of three trajectory segments from the MOVE floats at nominally at 1400 dbar in the DWBC. Their different overall lengths during the same time interval amount to average speeds of 14.6, 10.7, and 8.6  $\text{cm s}^{-1}$ , decreasing away from the boundary and demonstrating the horizontal shear associated with the DWBC. This independently results in a width of the boundary current of circa 150 km by simple extrapolation, in agreement with what the previous figures (6.2–6.4) have shown.

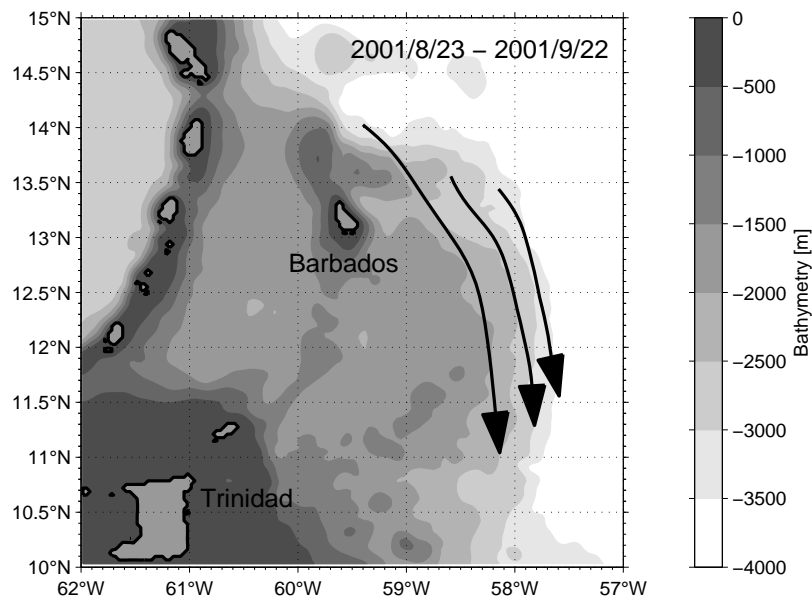


Figure 6.5: Snapshot of three simultaneous trajectories in the DWBC east of the Lesser Antilles. All trajectories are from the same time period, revealing the horizontal shear associated with the intensification of the current towards the boundary. Data are from MOVE RAFOS floats nominally at 1400 dbar.

## 6.2 Mesoscale Variability

The previous paragraphs have shown that the observed mean velocities in the inner basins away from the equatorial region are virtually insignificant. However, many individual float trajectories have relatively high velocities. For the MOVE floats in the AAIW layer, where mean velocity is zero, the RMS value of the ten-day displacement velocities is still  $4.4 \text{ cm s}^{-1}$ , and more than 20% of the ten-day mean velocities exceed  $10 \text{ cm s}^{-1}$ . This clearly motivates a closer look at the mesoscale velocity field. Due to their high temporal resolution (at least one position per day), the acoustically tracked floats of the MOVE, NBC, and SAMBA campaigns are used for this, along with a limited number of older SOFAR and WOCE-era RAFOS floats. The treatment of the data is essentially identical to that presented in the corresponding section on the northeastern Atlantic (section 3.4). Similar maps of energy and time scales are presented, but these will not be combined to produce a diffusivity estimate as the assumption of isotropic turbulence is invalid at least in the equatorial zonal currents. The temporal window for detrending in the computation of energy and time scales was chosen at 80 d to account for a few SAMBA trajectories which had shortened tracks of acoustic reception. The inconsistency from the fact that the NBC floats were deliberately launched into North Brazil Current rings and thus might bias the statistics is of minor concern due to their small number and the fact that most of them seem to have been below the influence of the rings (FRATANTONI AND RICHARDSON, 2006).

Figure 6.6 shows maps of Lagrangian eddy kinetic energy (EKE) and integral time scale for the AAIW layer in the northwestern tropical Atlantic, methodologically similar to figure 3.11 in the section on the North Atlantic. EKE is highest near the boundary (exceeding  $100 \text{ cm}^2 \text{ s}^{-2}$ ) and decreases to values near or below  $50 \text{ cm}^2 \text{ s}^{-2}$  in the interior basin, especially to the north. A suspicious fan of increased EKE reaches offshore from  $10^\circ \text{ N}$  and  $55^\circ \text{ W}$ , which corresponds to the northernmost extent of the equatorial currents defined by the NEIC reaching the boundary. At roughly this location, the NBUC ceases to exist, which is marked by its rings closer to the surface. FRATANTONI AND RICHARDSON (2006) discuss an energetic, small cyclone there, which is surprising as they expected the large anticyclonic NBC rings as found by RICHARDSON ET AL. (1994). Interestingly, a second such cyclone is sampled independently by a SAMBA float, suggesting that this particular type of eddy might occur frequently there. A small area between Barbados and the southernmost Windward Islands (centered around  $60.5^\circ \text{ W}$  and  $12.5^\circ \text{ N}$ ) is separated from the open Atlantic by a submarine ridge and also has high EKE, although the area is sampled by just one float. Another broad maximum of EKE just below  $100 \text{ cm}^2 \text{ s}^{-2}$  spans the equatorial area, especially between the equator and  $5^\circ \text{ N}$ . This is the region where a lot of energetic interaction with the equatorial currents and the boundary (NICC and EIC) is observed.

The Lagrangian integral time scale is longest in the interior basin away from the equator and reaches values of typically just below 10 d, which would connect well with the POLY-MODE data (ROSSBY ET AL., 1986b). Closer to shore and within the equatorial region, shorter time scales around 5 d are observed. The float captured southwest of Barbados has also experienced short time scales. Corresponding length scales are 20–30 km for the open ocean, exceeding 50 km in the boundary current regime off the Amazon, and near 50 km in the equatorial area offshore.

The same information is also shown by figure 6.7, which shows average energy and time scales as a function of distance offshore for two regions: one east of the Lesser Antilles

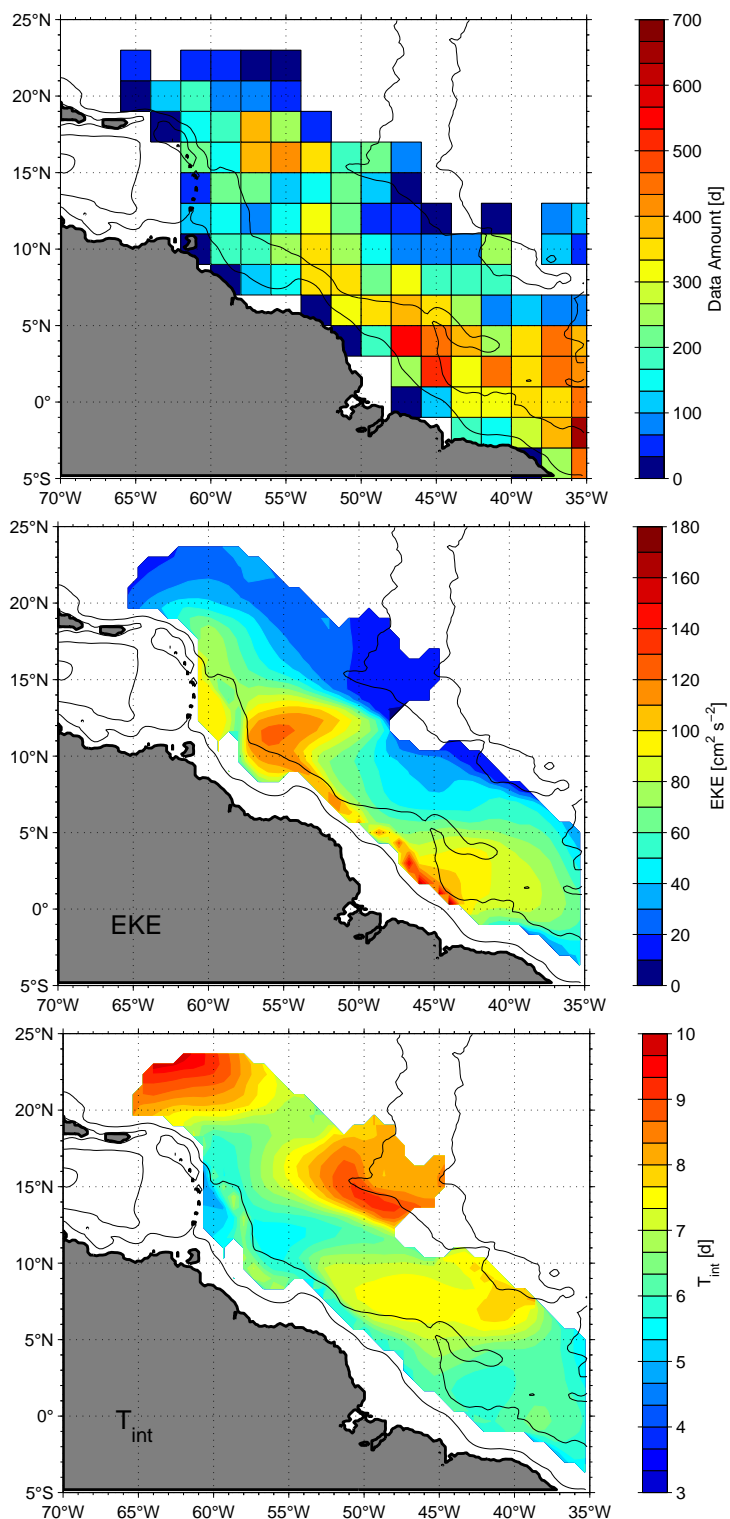


Figure 6.6: Lagrangian eddy scales in the AAIW layer of the northwestern tropical Atlantic derived from acoustically tracked floats. *Top:* Data density in cumulative days of data within boxes of 2°-by-2°. *Middle:* Lagrangian eddy kinetic energy. *Bottom:* Lagrangian integral time scale. Cf. figure 3.11 for comparison with the North Atlantic. Bathymetry is shown at 1000 and 4000 m.

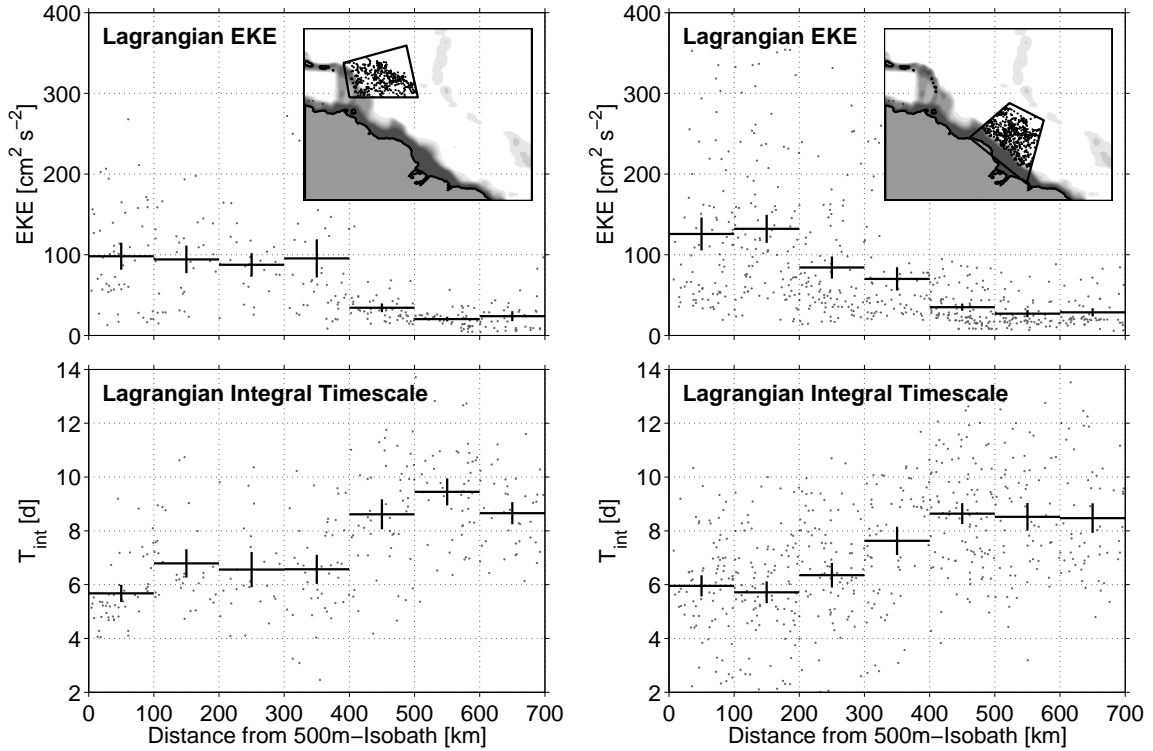


Figure 6.7: Characteristics of the eddy field as a function of distance offshore for the AAIW layer. Grey dots are individual measurements from trajectory segments of 80 d duration. Black crosses indicate averages for bins of 100 km width. The vertical extent of the crosses corresponds to a 95% confidence interval. The data source is identical to that of figure 6.6. *Top panels:* Lagrangian eddy kinetic energy. The map inlets show data origins. *Bottom panels:* Lagrangian integral time scale. *Left:* From a box east of the Lesser Antilles. *Right:* From a box off French Guiana.

and one off French Guiana. In both cases, EKE increases towards the boundary, while the time scale of eddy activity decreases. Maximum EKE averages are near  $100 \text{ cm}^2 \text{ s}^{-2}$  at the boundary, and minimum values near  $25 \text{ cm}^2 \text{ s}^{-2}$  offshore, with slightly higher values in the southern box. Lagrangian integral time scales are between 6 and 9 d in both cases.

Figure 6.8 shows the same for the uNADW layer, for which data coverage is not sufficient to produce maps as in figure 6.6. In both boxes, EKE increases towards the shore, but the northern box has significantly lower values. Off the Lesser Antilles, EKE varies between approximately  $10 \text{ cm}^2 \text{ s}^{-2}$  in the open ocean and  $30 \text{ cm}^2 \text{ s}^{-2}$  near the western boundary, whereas in the southern box, the range is from 10 to  $110 \text{ cm}^2 \text{ s}^{-2}$ . The integral time scales are mostly between 7 and 9 d with a tendency towards shorter times near the shore in the south, but without any clear pattern evolving from the data in the northern box. Corresponding length scales are between 20 and 70 km.

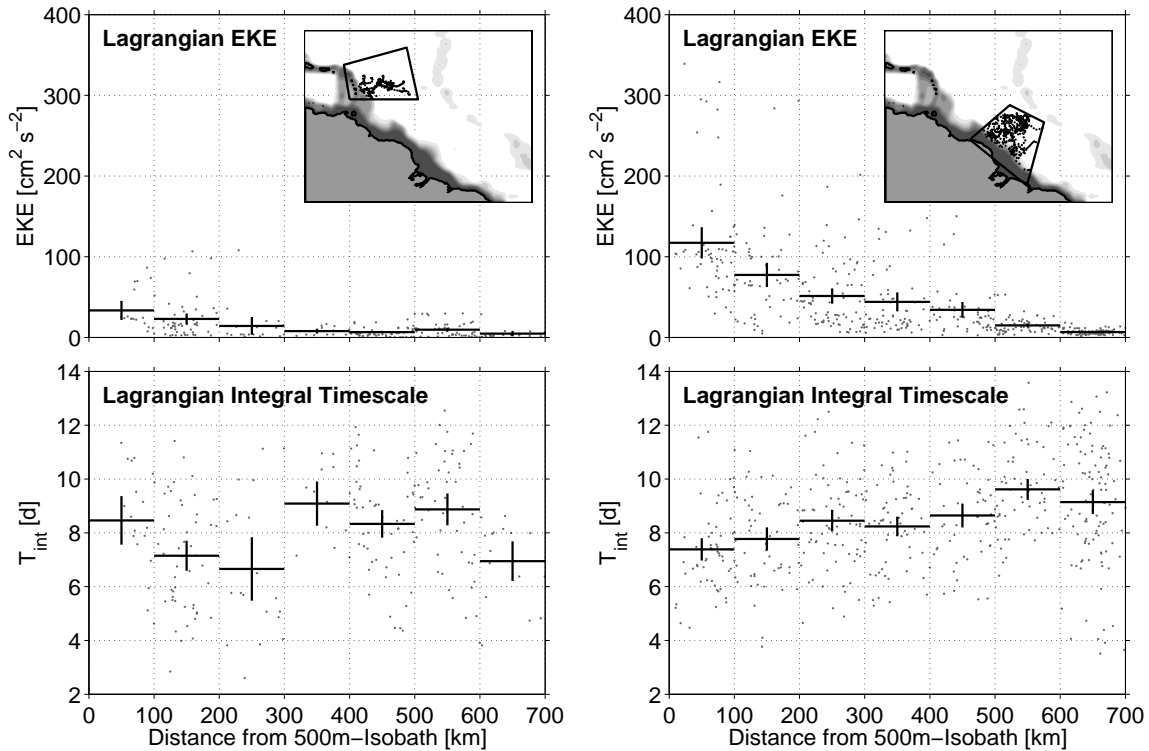


Figure 6.8: Characteristics of the eddy field as a function of distance offshore for the uNADW layer, for which maps as in figure 6.6 cannot be produced because of data sparsity. Otherwise as figure 6.7. *Top panels:* Lagrangian eddy kinetic energy. The map inlets show data origins. *Bottom panels:* Lagrangian integral time scale. *Left:* From a box east of the Lesser Antilles. *Right:* From a box off French Guiana.

### 6.3 Concluding Remarks

Float data from the depth of AAIW in the northwestern tropical Atlantic show only weak mean currents in the basin interior. Areas of strong mean flow are restricted to the equatorial zonal current bands and the boundary current, i. e. the northward-flowing North Brazil Undercurrent. At the uNADW level, a net westward flow around  $16^\circ$  N is observed, in addition to the southward-flowing DWBC. Float observations in the boundary currents of either depth range augment previous mooring data with additional observations of the strengths and widths of the currents. Mesoscale variability at both depths is more energetic towards the boundary, with highest Lagrangian EKE near  $100 \text{ cm}^2 \text{ s}^{-2}$ . Lagrangian integral time scales are between 5 and 10 d, with short time scales near the boundary. EKE generally seems to decrease towards the subtropical basin to the north, with time scales increasing simultaneously.

Put together, these findings suggest a flow regime that is most energetic both in the mean and in the EKE near the coast of South America, while energy levels rapidly decrease towards the interior.



## 6.4 Database for Chapters 5 and 6

The studies of the tropical Atlantic in chapters 5 and 6 were initiated by the analysis of a relatively small (26 instruments, 23 of which delivered data) set of RAFOS floats east of the Caribbean (LANKHORST, 2003, Meridional Overturning and Variability Experiment, MOVE). Soon, the data was combined with similar data from the nearby North Brazil Current (NBC) experiment (FRATANTONI AND RICHARDSON, 2006), and the idea arose to combine all float data in the area at intermediate depths. This ultimately led to the collection of data outlined in table 6.1, which provides the database for the above two chapters.

Floats from two depth ranges were considered in both cases: from one layer representing Antarctic Intermediate Water (AAIW, 600–1050 dbar), and from another layer called upper North Atlantic Deep Water (uNADW, 1200–2050 dbar) here. A different naming convention involving multiple types of Labrador Sea Water is used by RHEIN ET AL. (2004); the uNADW here corresponds reasonably well to their “upper Labrador Sea Water”. Based on the hydrography shown in figure 1.1, the depth ranges chosen are clearly within the water masses mentioned, bearing in mind that the hydrography in the eastern basin is slightly different from that of the western basin.

Floats of the two fundamentally different types—acoustic and profiling—are used in chapters 5 and 6.

To investigate the mesoscale variability (only chapter 6), the acoustic floats are used at their full temporal resolution (two positions per day for NBC floats, one per day for the others). Maps of the energy and time scales are presented, as already shown for the extratropical North Atlantic (section 3.3). The methodology is identical and has already been described in section 3.4. However, a time window for detrending of 80 d is applied here. The SOFAR data have been truncated after a maximum drift time of one year due to concerns about their vertical depth adjustment (RICHARDSON AND FRATANTONI, 1999).

For analyses of mean currents and seasonal variability, data from both acoustic and profiling float types are combined. In case of the profiling floats, each displacement was used as a single measurement of velocity. More than 98% of the displacements were of a duration between 9 and 11 days, with the rest being between 6 and 15 days. Therefore, 10 days is regarded the typical displacement duration. Data from the acoustic floats was brought to an equivalent format by “downgrading” (i. e. subsampling) the trajectories of the acoustic instruments into ten-day intervals that are comparable to the displacements of the profiling floats. Note that Lagrangian integral time scales of less than 10 d are identified (figure 6.6), thus each 10-d displacement may be considered a statistically independent velocity measurement.

In total, 22088 such displacements are obtained from within the AAIW and uNADW layers, accumulating to more than 600 years of float data. Table 6.1 lists data types and sources, and figure 6.9 shows data distribution in time and space, sorted by experiment. Figure 6.10 displays data densities as maps, separating the layers of Antarctic Intermediate Water (AAIW) and upper North Atlantic Deep Water (uNADW). The area under consideration is the entire open Atlantic between 12° S and 25° N (excluding the Caribbean), although the main focus is on the parts west of the Mid-Atlantic Ridge. Clearly, the AAIW layer is better sampled than the uNADW layer. In the AAIW, a basin-wide coverage has been achieved, which makes it possible to derive maps of mean velocities and investigate

Table 6.1: Float data collected in the tropical Atlantic. RAFOS, SOFAR, and MARVOR floats have acoustic underwater positioning. The internet page of the WOCE float data center (WFDAC) is indicated as the source for several datasets. Where individual persons are also listed, the actual data was obtained directly from them rather than through WFDAC.

Project Name	Float Type	PI	Data Source	References
MOVE	RAFOS	U. Send, W. Zenk	IFM-GEOMAR	LANKHORST (2003)
NBC	RAFOS	D. Fratantoni, P. Richardson	wfdac.who.edu, C. Wooding	FRATANTONI AND RICHARDSON (2006)
ABACO	RAFOS	K. Leaman	wfdac.who.edu	LEAMAN AND VERTES (1996)
SAMBA	MARVOR	M. Ollitrault, A. C. de Verdière	M. Ollitrault, IFREMER	OLLITRAULT ET AL. (2006)
IFM WOCE-era	RAFOS	O. Boebel, W. Zenk	IFM-GEOMAR	BOEBEL ET AL. (1999)
Trop. Atl. SOFAR	SOFAR	P. Richardson, W. Schmitz	wfdac.who.edu	RICHARDSON AND FRATANTONI (1999)
Argo	Profiling	Multiple	Argo Data Centers	www.argo.ucsd.edu
ACCE (WHOI)	Profiling	R. Schmitt	wfdac.who.edu, E. Montgomery	MOLINARI ET AL. (1999)
ACCE (RSMAS)	Profiling	K. Leaman	wfdac.who.edu, P. Vertes	

variability throughout the entire area under consideration. For the uNADW, data is sparser and not as evenly distributed in space, so that only averages over limited regions are possible.

Most of the data ( $\approx 50\%$ ) is now from the Argo array of profiling floats, followed by the acoustic floats from the French SAMBA (SubAntartic Motions in the Brazil Basin) project and contributions from profiling floats during the ACCE (Atlantic Circulation and Climate Experiment) campaigns of different US institutions. Ironically, the data amounts contributed by the two initial projects (MOVE and NBC) are very small compared to the rest, but the fact that they deliver eddy-resolving trajectories through their acoustic navigation makes them a crucial data source for the discussion of the mesoscale variability.

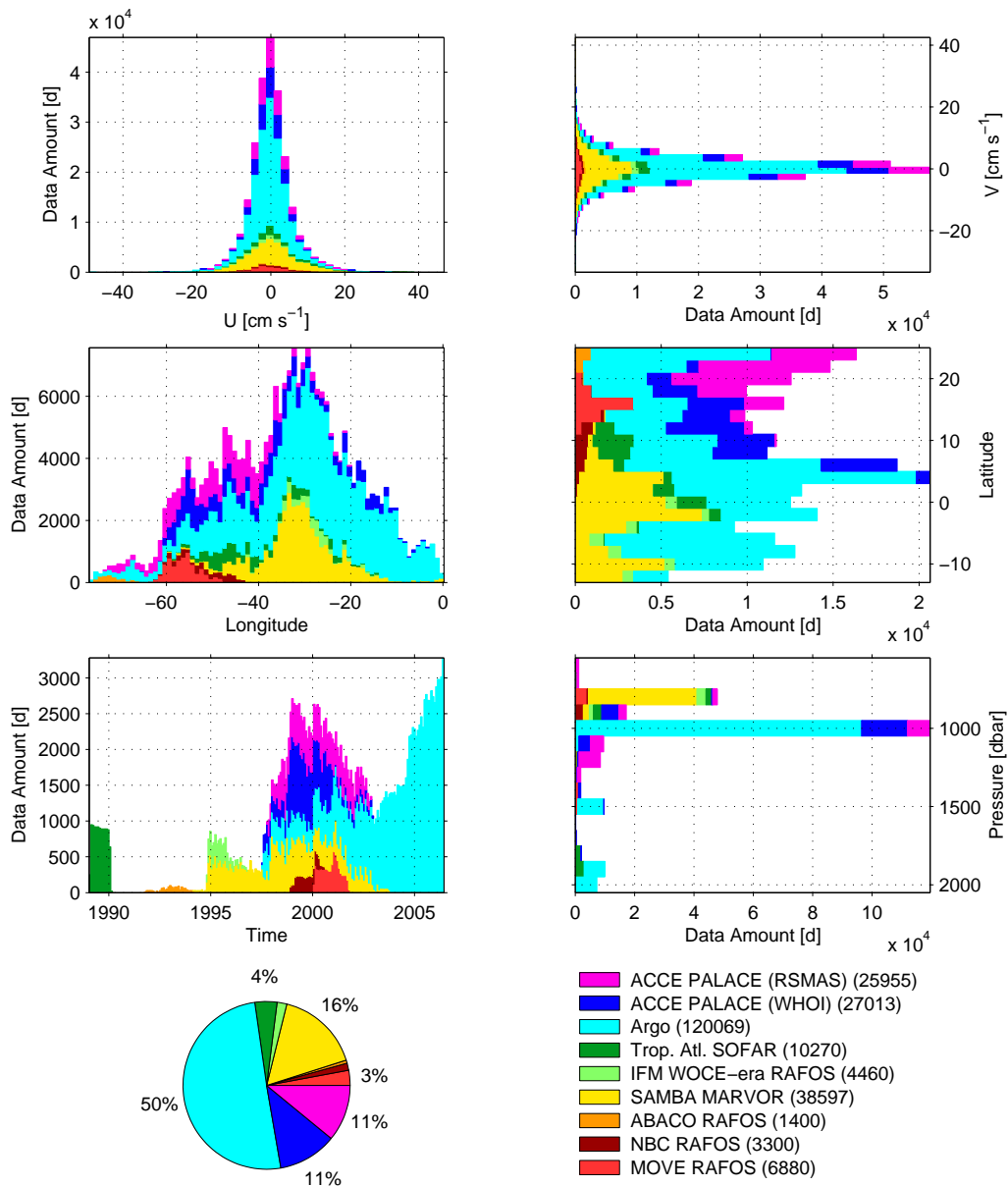


Figure 6.9: Float data distribution in the tropical Atlantic at intermediate depth. From top to bottom: velocities, location, time and depth, and contributions by experiment. Numbers are given in “float days”, i. e. days during which a float was in mission. The Argo array provides by far the largest amount of data, followed by the acoustically tracked floats from the SAMBA project.

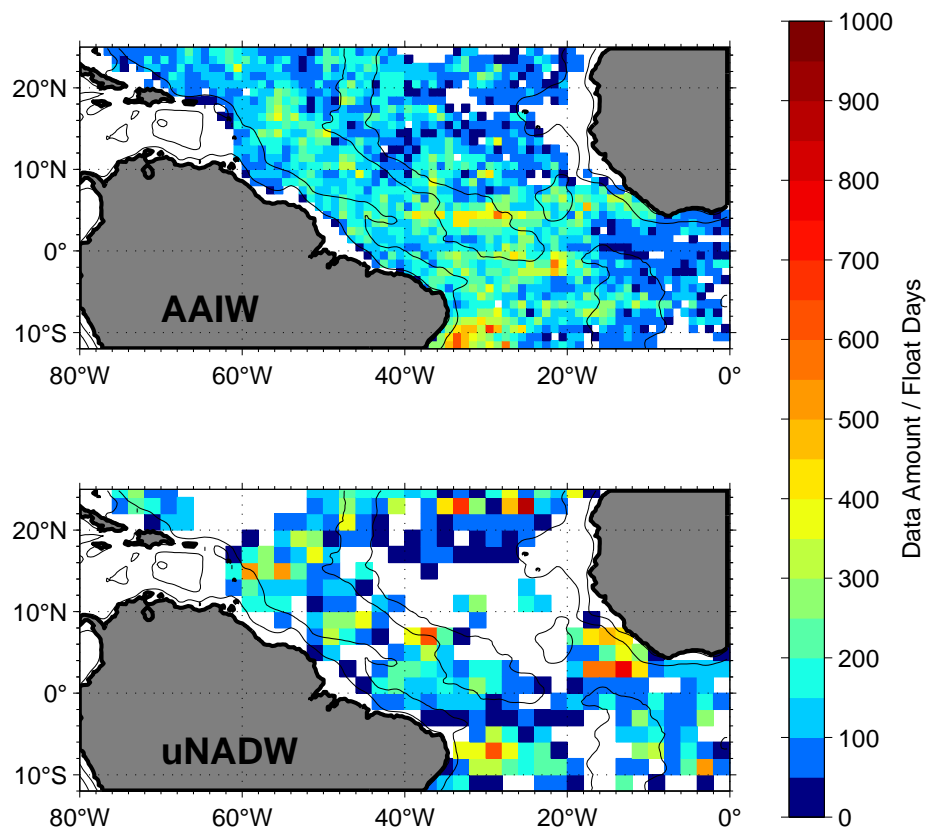


Figure 6.10: Map of float data densities achieved in the tropical Atlantic. *Top:* for the Antarctic Intermediate Water (AAIW) layer in boxes of  $1^\circ$ . *Bottom:* for the upper North Atlantic Deep Water (uNADW) layer in boxes of  $2^\circ$ . Bathymetry outlined at 1000 and 4000 m.

## Chapter 7

# Summary and Conclusion

In this study, the ocean circulation is investigated with floats. Two fundamentally different instrument types, profiling and acoustic, are used in different ways to derive results on mean currents, seasonal variability, and the mesoscale eddy fields in the northeastern Atlantic and the tropical Atlantic. Although far apart from each other, the two regions are linked by the global ocean circulation, in this case the Meridional Overturning Circulation (MOC) of the Atlantic Ocean. The MOC carries warm water northwards near the surface, which is balanced by a southward transport of cold water at greater depths. The observations in the northeastern Atlantic here show results on both the warm and the cold component of this circulation. Analyses of the tropical region focus on an intermediate depth that is generally assigned to the warm branch of the MOC, and on the upper parts of the cold limb.

As for the methodology applied, the following float data have been exploited: hydrographic profiles collected from profiling floats, large-scale velocities derived from float displacements of either float type, and eddy-resolving velocity data from acoustic floats. An endpoint technique to derive geostrophic transports between remote clusters of floats is able to retrieve time series of volume transports in the major currents of the northeastern Atlantic (chapter 2). In this chapter, hydrographic data collected with profiling floats are used, a methodology inherently capable of overcoming data sparseness and of averaging over the unresolved eddy field. In contrast to this endpoint method, mean currents and their seasonal variability at the equator are analyzed in chapter 5 by direct velocity measurements from a large database of different float types. Obviously, the geostrophic endpoint technique is not possible there due to the lack of the Coriolis force. In both cases of deriving the mean currents, the mesoscale eddy field is a source of uncertainty. It can, however, be directly observed with acoustic floats at appropriate temporal resolution, which is presented here in chapters 3, 4, and 6. Typical Lagrangian energy and time scales of the eddy field in the ocean interior are found to be 1–150  $\text{cm}^2 \text{s}^{-2}$  and 2–10 d. These energy levels show that the eddy field is indeed a major feature of the ocean circulation, in particular in the interior basins where mean currents are low.

The current branches in the northeastern Atlantic of the warm limb of the MOC (chapter 2) that are analyzed here are the Irminger Current, North Atlantic Drift Current, and the Azores Current. The geostrophic endpoint technique used to derive their transports depends heavily on the reference level for the integration of the velocity shear. Here, the sea surface height is used as the reference level, and it is found that the recent estimate of the mean surface by MAXIMENKO AND NILER (2005) compares well with independent

velocity observations. Combining the float profiles, mean sea surface height, additional hydrographic profiles from moorings, and satellite altimetry yields transport estimates of 5, 20, and 8 Sv for the three current branches. For the Irminger and North Atlantic Drift Currents, variability of 2–3 Sv is found in an antiphase correlation on time scales of 2–3 years. A manuscript in preparation by BOWER AND VON APPEN (2006) discusses similar time scales in observations of the North Atlantic Current immediately above the Mid-Atlantic Ridge and suggests that the interpretation of the observations here might be more complicated than just a simple translation of the current axis to the north, instead involving multiple current branches of variable intensity.

Chapter 3 presents results from RAFOS floats in the northeastern Atlantic at depths between 1500 and 2600 dbar, located in the Labrador Sea Water (LSW) and Iceland Scotland Overflow Water (ISOW). Both water masses are heavily involved in the cold branch of the MOC. Individual pathways provide direct evidence of the spreading paths, emphasizing the role of fracture zones in the Reykjanes Ridge as areas of exchange between the eastern and the western basins. Additional pathways documented by the floats show ventilation of the West European Basin to the south and a boundary current around the southern Rockall Plateau. Properties of the mesoscale eddy field contrast sharply between the subpolar and the subtropical basins, the subpolar basin having higher energy levels by an order of magnitude and shorter time scales. Areas of highest eddy intensity in the Iceland Basin are interpreted to be locations of water mass transformation involving LSW and ISOW.

Chapter 4 presents an automatic identification algorithm for coherent eddies in float trajectories. Compared to the manuscript by LANKHORST (2003), the methodology has been revised to remove any a-priori assumptions on the flow field, and it is thoroughly validated against a comparison study (SHOOSMITH ET AL., 2005). Applied to the trajectories of the previous chapter, the algorithm reveals a particularly high abundance and intensity of cyclonic vortices in the subpolar northeastern Atlantic, suggesting that these features play an active role in the mixing processes there.

Chapter 5 contains direct velocity measurements from the equatorial Atlantic, which for the first time provide basin-wide coverage at data densities allowing for a representative estimate of the mean flow and its seasonal variability at intermediate depths. Strong zonal bands of alternating zonal flow are identified with mean velocities exceeding  $10 \text{ cm s}^{-1}$  in the open ocean. These measurements put to rest the discussion about the mere existence of these alternating flow bands, but clearly do not settle the question about possible effects on the MOC. Such effects could be through interaction with the boundary current and through modified lateral mixing in the basin interior.

Finally, chapter 6 shows results from the northwestern tropical Atlantic, offshore off South America and the Lesser Antilles. Significant mean flow is only found in the boundary current regime and in the equatorial current bands. The float data complement older mooring data in the boundary current at two depths (centered around 800 and 1600 dbar), resolving its lateral structure and showing the side-by-side patterns of the boundary and the equatorial currents. Acoustic floats are then again utilized to map out the quantities of the mesoscale eddy field at both levels, showing that generally the energy levels are higher by an order of magnitude near the boundary compared to the inner basin, and that they decrease further in the subtropical regime to the north.

The two methodologies of the eddy detection and of the geostrophic endpoint technique using profiling floats are new and, as an outlook, provide opportunities for future applica-

tions to different datasets. As for the endpoint method, application to any region of interest with sufficient data coverage seems possible, with the caveat that some direct velocity measurement should be available to validate the geostrophic reference level. Obvious candidates for the eddy detection algorithm would be the global surface drifter data collected over the past few decades, and existing RAFOS datasets elsewhere.

As for the measurements of the zonal equatorial currents, the present challenge to oceanographic research is to achieve numerical simulations that reproduce these patterns, which seems to be possible now. Clearly, numerical models need such observations to be validated against. Perhaps as a next step in model improvement, the author hopes that the maps of the mesoscale properties presented herein for both the northeastern and the tropical Atlantic prove useful. In any case, the values observed here can possibly aid in parameterizing features not resolved in coarse-resolution models.





# Appendix A

## Glossary

**AAIW** Antarctic Intermediate Water

**AABW** Antarctic Bottom Water

**ACCE** Atlantic Circulation and Climate Experiment

**ADCP** Acoustic Doppler Current Profiler

**AGU** American Geophysical Union

**AMS** American Meteorological Society

**ANIMATE** Atlantic Network of Interdisciplinary Moorings and Time Series for Europe

**AR, AR2** Autoregressive Process (2nd order)

**AVISO** Archiving, Validation and Interpretation of Satellite Oceanographic Data

**AzC** Azores Current

**BAS** British Antarctic Survey

**BFZ** Bight Fracture Zone

**CGFZ** Charlie-Gibbs Fracture Zone

**CIS** Central Irminger Sea

**CNES** Centre National d'Études Spatiales (France)

**DANA** Drifter ANALysis, software by LANKHORST (2003)

**DSOW** Denmark Strait Overflow Water

**DUACS** Data Unification and Altimeter Combination System

**DWBC** Deep Western Boundary Current

**EIC** Equatorial Intermediate Current

**EKE** Eddy Kinetic Energy

- ESTOC** Estación Europea de Series Temporales del Oceano, Islas Canarias
- EUC** Equatorial Undercurrent
- GAGE** Guiana Abyssal Gyre Experiment
- GRACE** Gravity Recovery And Climate Experiment
- IFM-GEOMAR** Leibniz Institute of Marine Sciences (Kiel, Germany)
- IFREMER** French Research Institute for Exploitation of the Sea (Plouzané, France)
- IPRC** International Pacific Research Center (Honolulu, HI, USA)
- IrmC** Irminger Current
- ISOW** Iceland Scotland Overflow Water
- LSW** Labrador Sea Water
- MERSEA** Marine Environment and Security for the European Area
- MKE** Mean Kinetic Energy
- MOC** Meridional Overturning Circulation
- MOVE** Meridional Overturning Variability Experiment
- NAC, NADC** North Atlantic (Drift) Current
- NADW** North Atlantic Deep Water
- NBC, NBUC** North Brazil (Under-) Current
- NEC** North Equatorial Current
- NECC** North Equatorial Countercurrent
- NEIC** Northern Equatorial Intermediate Current
- NEUC** North Equatorial Undercurrent
- NICC** Northern Intermediate Countercurrent
- NOAA** National Oceanographic and Atmospheric Administration (USA)
- NODC** National Oceanographic Data Center (Washington, DC, USA)
- OLFRZ06** Study by OLLITRAULT ET AL. (2006)
- PAP** Porcupine Abyssal Plain
- RAFOS** SOFAR spelled backwards, Ranging and Fixing of Sound
- RSMAS** Rosenstiel School of Marine and Atmospheric Science (Miami, FL, USA)
- SAMBA** SubAntartic Motions in the Brazil Basin

**SEC** South Equatorial Current

**SEIC** Southern Equatorial Intermediate Current

**SEUC** South Equatorial Undercurrent

**SFB** Sonderforschungsbereich

**SICC** Southern Intermediate Countercurrent

**SigProcTbx** MatLab Signal Processing Toolbox

**SIO** Scripps Institution of Oceanography (La Jolla, CA, USA)

**SOFAR** Sound Fixing and Ranging

**SRBR05** Study by SHOOSMITH ET AL. (2005)

**SSALTO** Segment Sol multissions d'ALTimétrie, d'Orbitographie et de localisation précise

**UIB** University of Bergen (Norway)

**uNADW** Upper North Atlantic Deep Water

**WHOI** Woods Hole Oceanographic Institution (Woods Hole, MA, USA)

**WOCE** World Ocean Circulation Experiment



## Appendix B

# Acknowledgements

I gratefully appreciate public availability of the following data: Argo float data and OceanSITES mooring data were collected and made freely available by these international projects and the national programs that contribute to them. Argo is a pilot program of the Global Ocean Observing System. In particular, data from the following EU-funded projects were used: GYROSCOPE, ANIMATE, MERSEA. Several other float datasets have been received from the WOCE float data center (WFDAC). The 1992–2002 mean ocean dynamic topography data has been obtained from Nikolai Maximenko (IPRC) and Peter Niiler (SIO). The altimeter products were produced by SSALTO/DUACS and distributed by AVISO with support from CNES. NODC (Levitus) World Ocean Atlas 1994 data is provided by the NOAA-CIRES Climate Diagnostics Center, Boulder, Colorado, USA, on their web site.

I have received financial support through the following projects: SFB 460 (funded by the *Deutsche Forschungsgemeinschaft*, *DFG*), GYROSCOPE, ANIMATE, MFSTEP, and MERSEA (funded by the EU), MOVE (funded by the *Bundesministerium für Bildung und Forschung*, *BMBF*), and TROPAT (funded by DFG).

Furthermore, I am thankful for support by the following individuals: David Fratantoni and Philip Richardson have shared float data and kindly received me during a visit to WHOI. Christine Wooding, Ellyn Montgomery (both WHOI), and Peter Vertes (RSMAS) deserve thanks for helping with float data acquisition. Michael McCartney (WHOI) has provided mooring data from GAGE. Heather Furey (WHOI) and Deb Shoosmith (now BAS) have shared their float data and expertise with the eddy identification. Michel Ollitrault (IFREMER) has generously shared large data amounts collected in the SAMBA experiment and many helpful comments. Øyvind Knutsen (UIB) has provided vessel-mounted ADCP data from the “Nuka Arctica”. Luca Centurioni and Yoo Yin Kim (both SIO) have pointed me towards the 1992–2002 mean ocean dynamic topography. Arne Biastoch (IFM-GEOMAR) has contributed model output from the ORCA05 model. Andreas Macrander (AWI) has helped by proof-reading this manuscript and providing comments on the layout. Walter Zenk (IFM-GEOMAR) deserves special appreciation for being available and supportive throughout my entire career so far, including fruitful discussions about the work presented here. Last but not least, I am very thankful to my advisor Uwe Send (now SIO) and the entire physical oceanography group at IFM-GEOMAR for providing an excellent environment to perform research in.



## Appendix C

# Bibliography

- BARNIER, B., G. MADEC, T. PENDUFF, J.-M. MOLINES, A.-M. TREGUIER, A. BECKMANN, A. BIASTOCH, C. BÖNING, J. DENG, J. GULEV, S. LE SOMMER, E. REMY, C. TALANDIER, S. THEETTEN and M. MALTRUD, 2006: Impact of partial steps and momentum advection schemes in a global ocean circulation model at eddy permitting resolution. *Ocean Dynamics*.
- BERSCH, M., 1995: On the circulation of the northeastern North Atlantic. *Deep-Sea Res. I*, **42** (9), 1583–1607.
- BOEBEL, O., J. LUTJEHARMS, C. SCHMID, W. ZENK, T. ROSSBY and C. BARRON, 2003: The Cape Cauldron: a regime of turbulent inter-ocean exchange. *Deep-Sea Res. II*, **50** (1), 57–86.
- BOEBEL, O., C. SCHMID and W. ZENK, 1999: Kinematic elements of Antarctic Intermediate Water in the western South Atlantic. *Deep-Sea Res. II*, **46** (1–2), 355–392.
- BOWER, A., 2003: Directly-Measured Mid-Depth Circulation in the Northeastern North Atlantic. In: *Geophys. Res. Abstracts*, Europ. Geophys. Soc., Volume 5.
- BOWER, A. S., B. L. CANN, T. ROSSBY, W. ZENK, J. GOULD, K. SPEER, P. L. RICHARDSON, M. D. PRATER and H.-M. ZHANG, 2002: Directly measured mid-depth circulation in the northeastern North Atlantic Ocean. *Nature*, **419**, 603–607.
- BOWER, A. S. and W.-J. VON APPEN, 2006: Interannual Variability in the Pathways of the North Atlantic Current over the Mid-Atlantic Ridge and the Impact of Topography. *J. Phys. Oceanogr.*, submitted.
- BOX, G. E. P., G. M. JENKINS and G. C. REINSEL, 1994: *Time Series Analysis: Forecasting and Control*. Prentice-Hall, 3rd Edition.
- CURRY, R. G. and M. S. MCCARTNEY, 2001: Ocean Gyre Circulation Changes Associated with the North Atlantic Oscillation. *J. Phys. Oceanogr.*, **31** (12), 3374–3400.
- DAVIS, R. E., 1998: Preliminary results from directly measuring middepth circulation in the tropical and South Pacific. *J. Geophys. Res.*, **103** (C11), 24619–24639.
- DAVIS, R. E., D. C. WEBB, L. A. REGIER and J. DUFOUR, 1992: The Autonomous Lagrangian Circulation Explorer (ALACE). *J. Atmos. Oceanic Technol.*, **9**, 264–285.

- FISCHER, J., V. HORMANN, P. BRANDT, F. A. SCHOTT, B. RABE and A. FUNK, 2007: The South Equatorial Undercurrent in the tropical Atlantic deduced from floats and shipboard current meters. *Geophys. Res. Lett.*, Submitted.
- FRATANTONI, D. M. and P. L. RICHARDSON, 2006: The Evolution and Demise of North Brazil Current Rings. *J. Phys. Oceanogr.*
- FREELAND, H. J., P. B. RHINES and T. ROSSBY, 1975: Statistical observations of the trajectories of neutrally buoyant floats in the North Atlantic. *J. Mar. Res.*, **33** (3), 383–404.
- HANSEN, B. and S. ØSTERHUS, 2000: North Atlantic – Nordic Seas exchanges. *Progr. Oceanogr.*, **45** (2), 109–208.
- HEYWOOD, K. J., E. L. McDONAGH and M. A. WHITE, 1994: Eddy kinetic energy of the North Atlantic subpolar gyre from satellite altimetry. *J. Geophys. Res.*, **99** (C11), 22525–22539.
- JOCHUM, M. and P. MALANOTTE-RIZZOLI, 2003: *Interhemispheric Water Exchange in the Atlantic Ocean* (Eds.: G. J. Goni and P. Malanotte-Rizzoli), Elsevier, Chapter The flow of AAIW along the equator, 193–212.
- JOHNS, W. E., T. N. LEE, R. C. BEARDSLEY, J. CANDELA, R. LIMEBURNER and B. CASTRO, 1998: Annual Cycle and Variability of the North Brazil Current. *J. Phys. Oceanogr.*, **28** (1), 103–128.
- JOHNS, W. E., T. N. LEE, F. A. SCHOTT, R. J. ZANTOPP and R. H. EVANS, 1990: The North Brazil Current Retroflexion: Seasonal Structure and Eddy Variability. *J. Geophys. Res.*, **95** (C12), 22103–22120.
- KANZOW, T., U. SEND, W. ZENK, A. D. CHAVE and M. RHEIN, 2006: Monitoring the integrated deep meridional flow in the tropical North Atlantic: Long-term performance of a geostrophic array. *Deep-Sea Res. I*, **53** (3), 528–546.
- KLEIN, B. and G. SIEDLER, 1989: On the Origin of the Azores Current. *J. Geophys. Res.*, **94** (C5), 6159–6168.
- KNUTSEN, Ø., H. SVENDSEN, S. ØSTERHUS, T. ROSSBY and B. HANSEN, 2005: Direct measurements of the mean flow and eddy kinetic energy structure of the upper ocean circulation in the NE Atlantic. *Geophys. Res. Lett.*, **32**.
- KRAUSS, W., 1986: The North Atlantic Current. *J. Geophys. Res.*, **91**, 5061–5074.
- KRAUSS, W., 1995: Currents and mixing in the Irminger Sea and in the Iceland Basin. *J. Geophys. Res.*, **100** (C6), 10851–10871.
- KRAUSS, W. and C. W. BÖNING, 1987: Lagrangian properties of eddy fields in the northern North Atlantic as deduced from satellite-tracked buoys. *J. Mar. Res.*, **45** (2), 259–291.
- KRAUSS, W. and R. H. KÄSE, 1984: Mean Circulation and Eddy Kinetic Energy in the Eastern North Atlantic. *J. Geophys. Res.*, **89**, 3407–3415.



- LANKHORST, M., 2003: Klassifizierung charakteristischer Eigenschaften von Float-Trajektorien in unterschiedlichen dynamischen Regionen. Diploma Thesis, Mathematisch-Naturwissenschaftliche Fakultät, Christian-Albrechts-Universität Kiel, Germany, 84 pages.
- LANKHORST, M., 2006: A Self-Contained Identification Scheme for Eddies in Drifter and Float Trajectories. *J. Atmos. Oceanic Technol.*, **23** (11), 1583–1592.
- LANKHORST, M., D. FRATANONI, M. OLLITRAULT, P. RICHARDSON, U. SEND and W. ZENK, 2007a: The Circulation of the Western Tropical Atlantic at Mid-Depth as Observed by Floats. *In Preparation*.
- LANKHORST, M., M. NIELSEN and W. ZENK, 2004: Rafos Float Trajectories from the Labrador Sea Water Level in the Iceland Basin 1997–2003. Electronic Publication (Internet), <http://www.ifm-geomar.de/index.php?id=999&L=1>.
- LANKHORST, M., U. SEND and A. BIASTOCH, 2007b: Transport Time Series of Northeastern Atlantic Current Systems Derived from Long-Distance Geostrophy. *Geophys. Res. Lett.*, In Preparation.
- LANKHORST, M. and W. ZENK, 2006: Lagrangian Observations of the Middepth and Deep Velocity Fields of the Northeastern Atlantic Ocean. *J. Phys. Oceanogr.*, **36** (1), 43–63.
- LANKHORST, M. and W. ZENK, 2007: *Lagrangian Analysis and Prediction of Coastal and Ocean Dynamics* (Eds.: A. Griffa, A. D. Kirwan, A. J. Mariano, T. Özgökmen, and T. Rossby), Cambridge University Press, Chapter “On the Intermediate Circulation in the Iceland Basin (Favorite Trajectories)”. In press.
- LARGE, W. G. and S. G. YEAGER, 2004: Diurnal to decadal global forcing for ocean and sea-ice models: the data sets and flux climatologies. Technical Note NCAR/TN-460+STR, NCAR.
- LAVENDER, K. L., W. B. OWENS and R. E. DAVIS, 2005: The mid-depth circulation of the subpolar North Atlantic Ocean as measured by subsurface floats. *Deep-Sea Res. I*, **52** (5), 767–785.
- LEAMAN, K. D. and P. S. VERTES, 1996: Topographic Influences on Recirculation in the Deep Western Boundary Current: Results from RAFOS Float Trajectories between the Blake-Bahama Outer Ridge and the San Salvador “Gate”. *J. Phys. Oceanogr.*, **26** (6), 941–961.
- LUMPKIN, R., A.-M. TREGUIER and K. SPEER, 2002: Lagrangian Eddy Scales in the Northern Atlantic Ocean. *J. Phys. Oceanogr.*, **32** (9), 2425–2440.
- MARTIN, A. P., I. P. WADE, K. J. RICHARDS and K. J. HEYWOOD, 1998: The PRIME Eddy. *J. Mar. Res.*, **56**, 439–462.
- MatLab, 1984–2006: MatLab (TM). The MathWorks, Inc, [www.mathworks.com](http://www.mathworks.com).
- MAXIMENKO, N. A. and P. P. NIILER, 2005: *Recent Advances in Marine Science and Technology* (Ed.: N. Saxena), PACON International, Chapter Hybrid decade-mean global sea level with mesoscale resolution.

- MENZEL, M., 1995: Entwicklung eines Programmpaketes zur Datenaufbereitung, Berechnung und Visualisierung von Floattrajektorien. Diploma Thesis, Fachhochschule Kiel.
- MOLINARI, R. L., S. L. GARZOLI and R. W. SCHMITT, 1999: Equatorial currents at 1000 m in the Atlantic Ocean. *Geophys. Res. Lett.*, **26** (3), 361–363.
- NIILER, P. P., N. A. MAXIMENKO and J. C. MCWILLIAMS, 2003: Dynamically balanced absolute sea level of the global ocean derived from near-surface velocity observations. *Geophys. Res. Lett.*, **30** (22).
- OLLITRAULT, M., M. LANKHORST, D. FRATANTONI, P. RICHARDSON and W. ZENK, 2006: Zonal intermediate currents in the equatorial Atlantic Ocean. *Geophys. Res. Lett.*, **33**, L05605.
- OWENS, W. B., 1991: A statistical description of the mean circulation and eddy variability in the northwestern Atlantic using SOFAR floats. *Progr. Oceanogr.*, **28** (3), 257–303.
- PAILLET, J., 1999: Central Water Vortices of the Eastern North Atlantic. *J. Phys. Oceanogr.*, **29** (10), 2487–2503.
- PÉREZ-BRUNIUS, P., T. ROSSBY and D. R. WATTS, 2004: Absolute Transports of Mass and Temperature for the North Atlantic Current–Subpolar Front System. *J. Phys. Oceanogr.*, **34** (8), 1870–1883.
- PICKARD, G. L. and W. J. EMERY, 1990: *Descriptive Physical Oceanography*. Butterworth-Heinemann, 5th Edition.
- PINGREE, R. D. and B. LE CANN, 1991: Drifting Buoy in the Field of Flow of Two Eddies on East Thulean Rise (Northeast Atlantic). *J. Geophys. Res.*, **96** (C9), 16759–16777.
- POND, S. and G. L. PICKARD, 1983: *Introductory Physical Oceanography*. Butterworth-Heinemann, 2nd Edition.
- PRESS, W. H., B. P. FLANNERY, S. A. TEUKOLSKY and W. T. VETTERLING, 1993: *Numerical Recipes in FORTRAN 77: The Art of Scientific Computing*. Cambridge University Press, 2nd Edition.
- RHEIN, M., M. WALTER, C. MERTENS, R. STEINFELDT and D. KIEKE, 2004: The circulation of North Atlantic Deep Water at 16° N, 2000–2003. *Geophys. Res. Lett.*, **31** (L14305).
- RHINES, P. B., 1975: Waves and turbulence on a beta-plane. *J. Fluid Mech.*, **69** (3), 417–443.
- RICHARDS, K. J., N. A. MAXIMENKO, F. O. BRYAN and H. SASAKI, 2006: Zonal jets in the Pacific Ocean. *Geophys. Res. Lett.*, **33** (L03605).
- RICHARDSON, P. L. and D. M. FRATANTONI, 1999: Float trajectories in the deep western boundary current and deep equatorial jets of the tropical Atlantic. *Deep-Sea Res. II*, **46** (1–2), 305–333.
- RICHARDSON, P. L., G. E. HUFFORD and R. LIMEBURNER, 1994: North Brazil Current retroreflection eddies. *J. Geophys. Res.*, **99** (C3), 5081–5093.

- ROSSBY, T., 1996: The North Atlantic Current and surrounding waters: At the crossroads. *Rev. Geophys.*, **34** (4), 463–481.
- ROSSBY, T., 1999: On gyre interactions. *Deep-Sea Res. II*, **46** (1–2), 139–164.
- ROSSBY, T., 2007: *Lagrangian Analysis and Prediction of Coastal and Ocean Dynamics* (Eds.: A. Griffa, A. D. Kirwan, A. J. Mariano, T. Özgökmen, and T. Rossby), Cambridge University Press, Chapter “Evolution of Lagrangian Methods in Oceanography”. In press.
- ROSSBY, T., A. S. BOWER and P.-T. SHAW, 1985: Particle Pathways in the Gulf Stream. *Bull. Am. Met. Soc.*
- ROSSBY, T., D. DORSON and J. FONTAINE, 1986a: The RAFOS System. *J. Atmos. Oceanic Technol.*, **3** (4), 672–679.
- ROSSBY, T., J. PRICE and D. WEBB, 1986b: The Spatial and Temporal Evolution of a Cluster of SOFAR Floats in the POLYMODE Local Dynamics Experiment (LDE). *J. Phys. Oceanogr.*, **16** (3), 428–442.
- SCHMID, C., Z. GARAFFO, E. JOHNS and S. L. GARZOLI, 2003: *Interhemispheric Water Exchange in the Atlantic Ocean* (Eds.: G. J. Goni and P. Malanotte-Rizzoli), Elsevier, Chapter Pathways and variability at intermediate depths in the tropical Atlantic, 233–268.
- SCHMITZ, W. J., JR. and M. S. MCCARTNEY, 1993: On the North Atlantic Circulation. *Rev. Geophys.*, **31** (1), 29–49.
- SCHOTT, F., J. FISCHER, J. REPPIN and U. SEND, 1993: On Mean and Seasonal Currents and Transports at the Western Boundary of the Equatorial Atlantic. *J. Geophys. Res.*, **98** (C8), 14353–14368.
- SCHOTT, F., L. STRAMMA and J. FISCHER, 1999: Interaction of the North Atlantic Current with the deep Charlie Gibbs Fracture Zone throughflow. *Geophys. Res. Lett.*, **26** (3), 369–372.
- SCHOTT, F. A., M. DENGLER, P. BRANDT, K. AFFLER, J. FISCHER, B. BOURLÈS, Y. GOURIOU, R. L. MOLINARI and M. RHEIN, 2003: The zonal currents and transports at 35°W in the tropical Atlantic. *Geophys. Res. Lett.*, **30** (7).
- SCHOTT, F. A., J. FISCHER and L. STRAMMA, 1998: Transports and Pathways of the Upper-Layer Circulation in the Western Tropical Atlantic. *J. Phys. Oceanogr.*, **28** (10), 1904–1928.
- SHOOSMITH, D. R., P. L. RICHARDSON, A. S. BOWER and H. T. ROSSBY, 2005: Discrete eddies in the northern North Atlantic as observed by looping RAFOS floats. *Deep-Sea Res. II*, **52** (3–4), 627–650.
- SWIFT, D. D. and S. C. RISER, 1994: RAFOS Floats: Defining and Targeting Surfaces of Neutral Buoyancy. *J. Atmos. Oceanic Technol.*, **11** (4), 1079–1092.
- TAYLOR, G. I., 1921: Diffusion by continuous movements. In: *Proceedings of the London Mathematical Society*, Volume 20 of 2, 196–212.
- VAN AKEN, H. M. and C. J. DE BOER, 1995: On the synoptic hydrography of intermediate and deep water masses in the Iceland Basin. *Deep-Sea Res. I*, **42** (2), 165–189.

ZENK, W., A. PINCK, S. BECKER and P. TILLIER, 2000: The Float Park: A New Tool for a Cost-Effective Collection of Lagrangian Time Series with Dual Release RAFOS Floats. *J. Atmos. Oceanic Technol.*, **17** (10), 1439–1443.

## Erklärungen

Zu dieser Dissertation erkläre ich:

- Die Abhandlung ist von Form und Inhalt her meine Arbeit, abgesehen von der Beratung durch meinen Betreuer. Andere als die angegebenen Hilfen habe ich nicht verwendet.
- Die Arbeit hat weder ganz noch teilweise in einem Prüfungsverfahren vorgelegen.
- Teile der Arbeit sind in wissenschaftlichen Fachzeitschriften veröffentlicht worden bzw. zur Veröffentlichung eingereicht. Diese Teile sind in der Arbeit entsprechend vermerkt.
- Die Arbeit ist nach den Regeln guter wissenschaftlicher Praxis entstanden.

Kiel, 7. Februar 2007

M. Lankhorst



## Lebenslauf

**Name:** Matthias Jan Lankhorst

**Geburtsdatum und -ort:** 18.02.1977, Bottrop

**Nationalität:** Deutsch

**Wohnort:** Kiel

**Schulabschluß:** Abitur

**Studium:** Physikalische Ozeanographie (Diplom 2003)